

Small Area Estimation of Case Growths for Timely COVID-19 Outbreak Detection

Zhaowei She*

Singapore Management University, zwshe@smu.edu.sg,

Zilong Wang*

Georgia Institute of Technology, zwang937@gatech.edu,

Jagpreet Chhatwal

Massachusetts General Hospital, Harvard Medical School, jagchhatwal@mgh.harvard.edu,

Turgay Ayer†

Georgia Institute of Technology, ayer@isye.gatech.edu,

The COVID-19 pandemic has exerted a profound impact on the global economy and continues to exact a significant toll on human lives. The COVID-19 case growth rate stands as a key epidemiological parameter to estimate and monitor for effective detection and containment of the resurgence of outbreaks. A fundamental challenge in growth rate estimation and hence outbreak detection is balancing the accuracy-speed tradeoff, where accuracy typically degrades with shorter fitting windows. In this paper, we develop a machine learning (ML) algorithm, which we call *Transfer Learning Generalized Random Forest (TLGRF)*, that balances this accuracy-speed tradeoff. Specifically, we estimate the instantaneous COVID-19 exponential growth rate for each U.S. county by using TLGRF that chooses an adaptive fitting window size based on relevant day-level and county-level features affecting the disease spread. Through transfer learning, TLGRF can accurately estimate case growth rates for counties with small sample sizes. Out-of-sample prediction analysis shows that TLGRF outperforms established growth rate estimation methods. Furthermore, we conducted a case study based on outbreak case data from the state of Colorado and showed that the timely detection of outbreaks could have been improved by up to 224% using TLGRF when compared to the decisions made by Colorado’s Department of Health and Environment (CDPHE). To facilitate implementation, we have developed a publicly available outbreak detection tool for timely detection of COVID-19 outbreaks in each U.S. county, which received substantial attention from policymakers.

Key words: COVID-19, Epidemiology, Machine Learning, Outbreak Detection, Transfer Learning

1. Introduction

The COVID-19 pandemic has wreaked havoc on economies and human lives globally. Although vaccination efforts have effectively curtailed the spread of the virus, the specter

* Equal contribution co-first authors, listed alphabetically

† Corresponding author

of recurrent COVID-19 surges continues to loom, driven by factors such as waning immunity, vaccine hesitancy, the emergence of new variants, and the evolution of global policies. In China, for instance, the abrupt shift from a “zero-COVID” policy led to a swift and widespread Omicron outbreak, infecting an estimated 90% of the population by the end of December 2022 (Goldberg et al. 2023). In light of these dynamic conditions, accurate and timely estimation of new case growth rates remains paramount to prepare for potential outbreaks.

Since the beginning of the pandemic, the COVID-19 exponential growth rate has been a key epidemiological parameter closely monitored by public health officials (Anderson et al. 2020, Sommer 2020). This rate can be defined as the expected natural logarithmic ratio of two consecutive days’ infected case numbers (for an elaborate definition, please see §3.1 of this paper). As an illustration, if the infected case numbers on days t and $t - 1$ are generated from the same exponential growth model and are expressed as e^{rt} and $e^{r(t-1)}$, respectively, the natural logarithmic ratio would represent the exponential growth rate, i.e., $r = \ln\left(\frac{e^{rt}}{e^{r(t-1)}}\right)$. The exponential growth rate provides a direct measure of changes in infection numbers, with a larger exponential growth rate indicating faster growth. Additionally, as further discussed in §2.3, other important epidemiological parameters such as the basic reproduction number (R_0) are derived from the exponential growth rate and play key roles in various prescriptive models of COVID-19 outbreak management (Lipsitch et al. 2003, Ma 2020, Bertozzi et al. 2020). Lastly, and perhaps most importantly for our study purposes, accurately estimating and understanding spatial and temporal heterogeneity in exponential growth rates might help identify potential outbreaks. As such, the exponential growth rate is considered one of the most important “model-free” parameters in formulating a well-informed epidemic outbreak response (Chowell et al. 2003).

Nevertheless, it remains a challenge to obtain accurate small area exponential growth rate estimates of epidemic outbreaks (c.f. Ma et al. 2014), especially for diseases like COVID-19 where frequent policy-level (e.g., social distancing guidelines or school closures) and behavioral response changes (e.g., reduced mask use) quickly alter the disease propagation dynamics. In such a rapidly changing environment, it becomes a challenge to choose a fitting window size that balances the speed and accuracy tradeoff: while a longer fitting window is preferable as it reduces variance in estimation due to a larger sample size, a

shorter window is appealing for early and timely detection of outbreaks while they are still in controllable stages.

Historically, this fitting window size is treated as a hyperparameter that is either directly specified by the user (c.f. [Ben Phillips 2020](#)) or determined by cross-validation (c.f. [Chowell et al. 2007](#)) in the epidemiology literature. However, the constantly changing state and county level policy interventions and the public’s behavioral responses have presented new challenges with regard to fitting window size selection. More precisely, treating fitting window size as a single hyperparameter, as in the established literature and current practice, fails to consider the heterogeneity of COVID-19 growth rates across time and space. These limitations call for a more adaptive approach to accurately estimate the exponential growth rates across various jurisdictions and over time at a fast pace.

To address these challenges, we develop an adaptive machine learning algorithm, which we refer to as Transfer Learning Generalized Random Forest (TLGRF), that dynamically balances the speed-accuracy tradeoff by adjusting the window sizes over time and across space in case growth rate estimation. Specifically, to capture the heterogeneity of COVID-19 growth rates over time and across space, TLGRF chooses an adaptive fitting window size for each U.S. county on each day based on features that affect the disease spread, such as social distancing policies and the United States’ Centers for Disease Control and Prevention’s (CDC) Social Vulnerability Index. Moreover, for counties with insufficient data, TLGRF pools together all relevant COVID-19 case data from counties with similar features across the US via transfer learning.

Our study makes several key contributions to the relevant existing literature. First, from a methodological standpoint, we develop and present an adaptive Machine Learning (ML) based approach to select fitting windows that balances the challenging accuracy-speed tradeoff and demonstrate superior performance compared to established exponential growth rate estimates. Second, as further discussed in §2.2, our proposed TLGRF algorithm sheds new light on the “small sample problem” in COVID-19 outbreak detection (c.f. [Farrington and Andrews 2004](#)) and reduces model uncertainty in COVID-19 outbreak management (c.f. [Holmdahl and Buckee 2020](#), [Bertozi et al. 2020](#)). Third, through carefully designed experiments using county-level COVID-19 data throughout the pandemic, we show that TLGRF substantially improves case growth rate projections and can reduce the median Mean Absolute Error (MAE), defined as the average of the absolute difference

between the predictions and the ground truth samples, and Root Mean Squared Error (RMSE), defined as the square root of the average squared differences between the predictions and the ground truth samples, by at least 27.4% and 37.7% respectively (see §5.2 for details). In addition, applying TLGRF to Colorado state data reveals that CDPHE could have targeted counties with the most severe outbreaks in 58.79% of their investigations, a significant improvement over their historical decisions (18.13%). This marks a substantial 224% increase in the Positive Predictive Value (PPV) of CDPHE’s decisions (see §8 for details). To make our findings accessible to the policy-makers and the general public, we have further developed an online interactive local-level outbreak detection tool (www.covid19sim.org). Since official launch in September 2020, the outbreak detection tool has been used by more than 20,000 authentic users from all 50 states by April 2022. We have also been consulted by public health officials from several states to help them in their policy-making decisions through the support of the TLGRF algorithm.

The rest of this paper is organized as follows. §2 reviews the related literature in epidemiology, machine learning, and health operations management on COVID-19 outbreak detection and management, with an emphasis on current challenges and our contribution to this literature. §3 develops a statistical model that identifies the instantaneous county-level COVID-19 exponential growth rate, while §4 presents the proposed machine learning algorithm to estimate this model. §5 evaluates the performance of this machine learning algorithm against other fitting window size selection methods via out-of-sample prediction accuracy in 7-day ahead COVID-19 incident case number forecasts. §6 highlights the advantage of the proposed TLGRF algorithm over other types of GRF algorithms in instantaneous growth rate estimations and compares their empirical performance. §7 explores the potential applications and constraints of TLGRF beyond the task of county-level exponential growth rate estimations. §8 conducts a case study to demonstrate how TLGRF can assist health authorities prioritize limited resources in outbreak investigations. §9 discusses the decision support tool implementation of TLGRF. §10 concludes this paper with suggestions for future work.

2. Literature Review

In the global effort to combat COVID-19, various epidemiological models were developed by researchers from a wide range of academic disciplines. These models can be categorized

into three main classes, i.e., descriptive, predictive and prescriptive models (Liu and Xia 2020). §2.1 reviews relevant literature in epidemiology, machine learning and health operations management based on this model classification. §2.2 and §2.3 discuss some current challenges in these modeling approaches, and explain how our study contributes to the fast-growing literature on COVID-19 outbreak detection and management.

2.1. COVID-19 Outbreak Detection and Management Studies

A straightforward way to analyze COVID-19 outbreaks is through descriptive models such as clustering and hot spot analysis. The goal of these models is to identify spatial distribution patterns of COVID-19 infection clusters, which have been widely used for data visualization purposes by popular media outlets (The Mayo Clinic 2021, The New York Times 2021). More advanced clustering techniques such as generalized K-Means and point process analysis were also employed to detect COVID-19 outbreak clusters (Zhang and Lin 2021, Ruiz-Correa et al. 2021, Hohl et al. 2020).

Taking data visualization one step further, several studies, particularly in the machine learning community, have developed predictive models to predict when a COVID-19 outbreak was likely to happen and how severe the impact would be. For example, boosting algorithms like XGBoost were used to forecast whether a U.S. county would be affected by COVID-19, i.e., has at least one infected case (c.f. Mehta et al. 2020). Besides, CUSUM-based change detection and deep learning based anomaly detection techniques were also applied to detect aberrations in COVID-19 case growth patterns (c.f. Braca et al. 2021, Soldi et al. 2021, Karadayi et al. 2020). In addition, many short-term forecasting models are developed to predict the potential impacts (e.g., cases, hospitalizations and deaths) of COVID-19 outbreaks, with methods including deep learning (c.f. Rodriguez et al. 2020, Wieczorek et al. 2020), time-series analysis (c.f. Awan and Aslam 2020, Tandon et al. 2020) and support vector machine (c.f. Singh et al. 2020), among others. Starting from April 2020, the U.S. Centers for Disease Control and Prevention (CDC) formally established a COVID-19 Forecast Hub to generate ensemble forecasts by combining predictions from multiple epidemiological methods (Ray et al. 2020).

In addition to descriptive and predictive models, prescriptive models are often used to guide operational decisions such as how to allocate medical resources (e.g., ventilators and vaccines) and when to implement non-pharmaceutical interventions (NPIs) (e.g., social distancing and mask mandate). Many of these prescriptive models in COVID-19 outbreak

management are developed by healthcare operations management researchers. For example, [Mehrotra et al. \(2020\)](#) developed a stochastic optimization model to allocate ventilators in the national stockpile across states to address COVID-19 outbreaks. The compartmental modeling approach, often utilizing either the susceptible-infected-recovered (SIR) model or the susceptible-exposed-infectious-recovered (SEIR) model, has been employed to investigate various decision-making challenges, such as the formulation of targeted lockdown policies to curb COVID-19 outbreaks (e.g., [Birge et al. 2022](#), [Palmer et al. 2020](#), [Camelo et al. 2021](#), [Li et al. 2023](#)). By explicitly modeling population transitions between different disease states (e.g., susceptible (S), exposed (E), infected (I), and recovered (R)), these compartmental models have played pivotal roles in elucidating the dynamics of COVID-19, especially with respect to the implementation of targeted policies and the behavioral responses they elicit (e.g., [Chen et al. 2020](#), [Bai et al. 2021](#), [Chen and Kong 2023](#)). Last but not least, the global pandemic also catalyzes collaborations between researchers and practitioners. In the past two years, various practice-based COVID-19 outbreak management models have been developed to inform policy and clinical level decisions such as targeted border screening, patient triage, ICU capacity and nurse staffing planning (c.f. [Bastani et al. 2021](#), [Betcheva et al. 2021](#), [Bertsimas et al. 2021](#), [Kaplan 2020](#), [Shi et al. 2021](#)).

2.2. The Small Sample Problem

A distinctive challenge in epidemic outbreak detection is the small sample problem. Specifically, to effectively contain potential outbreaks in their early stages, an outbreak detection algorithm must provide early warning signals of these outbreaks before they fully develop, when their case numbers are still small ([Farrington and Andrews 2004](#)). However, when case numbers are small, accurately training statistical or machine learning models becomes a challenge due to the small sample size problem. Unless managed carefully, models tend to overfit in such cases resulting in poor out-of-sample prediction and the level of overfitting increases with the model complexity ([Nakip et al. 2020](#)).

In ML, a common approach to address this small sample problem is through transfer learning (c.f. [Pan and Yang 2009](#), [Zhuang et al. 2020](#)). Specifically, transfer learning refers to a class of ML algorithms that pool relevant proxy data to improve their ML models' performance on target data. For example, [Bastani \(2021\)](#) propose a LASSO-based estimator to incorporate a large sample of proxy data in ML models to improve their prediction performance on target data. Following a similar spirit, [Farias and Li \(2019\)](#) develop a

tensor completion model to improve recommender systems’ performance on target customers through pooling response data from other proxy customers. Based on the successful application of transfer learning in various settings, it is natural to expect that a similar technique can be employed to address the small sample problem in epidemic outbreak detection.

However, existing transfer learning techniques are not directly applicable to COVID-19 outbreak detection to address the small sample problem. Specifically, transfer learning algorithms rely on well-defined target tasks, which require the existence of a target predictive/decision function that maps the target domain to the target label space (c.f. Definition 1 by [Pan and Yang \(2009\)](#) and Definition 3 by [Zhuang et al. \(2020\)](#)). However, as explicitly modeled in §3.1, the dynamic nature of the COVID-19 pandemic may induce a domain shift from day to day and county to county. This results in a target learning domain comprising *a single data point*: the incident case number for a specific county on a particular day. This data point cannot be properly mapped to our target label space, which is defined as the realm of potential slopes corresponding to the possible instantaneous county-level COVID-19 exponential growth rates for the county on that day. Essentially, our target domain lacks an instance that can be appropriately labeled, considering that at least two data points are required to establish a slope. Consequently, in the absence of additional identification assumptions, the application of transfer learning methodologies to enhance growth rate estimations is infeasible.

To facilitate the application of transfer learning in COVID-19 outbreak detection, we propose a Transfer Learning Generalized Random Forest (TLGRF) algorithm in this paper, which allows proper identification of the county-level instantaneous COVID-19 exponential growth rates. The necessity for a new algorithm stems from the limitations of the classical generalized random forests (GRF) algorithm, which cannot effectively utilize time (or treatment) dependent features, such as the duration of face mask mandates in a given county. As demonstrated in §6.1, the population overlap assumption, a fundamental assumption of the GRF algorithm, is violated when features are time-dependent. Consequently, the county-level instantaneous COVID-19 exponential growth rate cannot be identified as a conditional average partial effect, and thus cannot be estimated by the classical GRF algorithm. To address these time-dependent heterogeneities and to enable transfer learning, our proposed TLGRF algorithm extends the classical GRF algorithm to models with variable treatment intensity (c.f. [Angrist and Imbens 1995](#), [Athey et al. 2019](#)).

2.3. Model Uncertainty in COVID-19 Outbreak Management

Another challenge in COVID-19 outbreak management comes from model uncertainty (Holmdahl and Buckee 2020). Specifically, prescriptive models to guide COVID-19 outbreak management, as reviewed in §2.1, require accurate estimates of key epidemiological parameters such as the basic reproduction number and the exponential growth rate. However, the fact that these parameter estimates tend to vary from one outbreak to another leads to high model uncertainty in COVID-19 outbreak management (Bertozi et al. 2020).

Among these epidemiological parameters, the epidemic exponential growth rate is viewed as one of the most important “model-free” parameters in/for epidemic outbreak detection and management (Chowell et al. 2003, Anderson et al. 2020). Specifically, the epidemic exponential growth rate can be estimated through pure phenomenological models that are independent of disease transmission assumptions (Ma et al. 2014). Furthermore, for epidemiological parameters whose estimation depends on certain modeling assumptions, a more accurate estimate of the epidemic exponential growth rate would lead to more accurate estimates of these “model-based” parameters as well. For example, when a mechanistic transmission model (e.g., an SIR or SEIR model) is assumed, the basic reproduction number (R_0) is a function of the exponential growth rate. More precisely, in an SIR model where the infectious period is exponentially distributed with a mean $\frac{1}{\gamma}$, its basic reproduction number (R_0) is determined by the epidemic exponential growth rate (r) as $R_0 = \frac{r}{\gamma} + 1$. In an SEIR model where the infectious and latent periods are exponentially distributed with means $\frac{1}{\gamma}$ and $\frac{1}{\sigma}$ respectively, its basic reproduction number (R_0) is determined by the epidemic exponential growth rate (r) as $R_0 = \frac{(r+\gamma)(r+\sigma)}{\gamma\sigma}$ (Ma 2020). Therefore, reducing uncertainty in epidemic exponential growth rate estimation would help in COVID-19 outbreak management regardless of their disease transmission assumptions.

To this aim, this paper proposes a new algorithm to improve the estimation accuracy of exponential growth rates in COVID-19 outbreaks. Specifically, this algorithm addresses a long-standing open problem in epidemiology regarding the speed and accuracy tradeoff in epidemic exponential growth rate estimation, and demonstrates consistently higher out-of-sample prediction accuracy compared to existing estimation methods.

3. Instantaneous Exponential Growth Model and Identification

This section first constructs an instantaneous COVID-19 exponential growth model (§3.1). Subsequently, we present and discuss the identification assumptions of the instantaneous county-level exponential growth rate $r_{t,c}$ from this model (§3.2).

3.1. Instantaneous Exponential Growth Model

To capture the heterogeneity of COVID-19 case growth patterns, we employ a flexible actual growth model for each county's daily log incident case number, as follows:

$$\ln(\mathbf{I}_{s,c}) = \alpha(\mathbf{X}_{s,c}) + r(\mathbf{X}_{s,c})\mathbf{s} + \varepsilon_{s,c}. \quad (1)$$

Here, $\mathbf{I}_{s,c}$ is the observed incident case number of county c on day \mathbf{s} . The detailed epidemiological definition of incident case number is presented in Appendix B. The independent variable is day \mathbf{s} . In addition, the intercept term $\alpha(\mathbf{X}_{s,c})$ and the slope term $r(\mathbf{X}_{s,c})$ are constructed as random coefficients of relevant features $\mathbf{X}_{s,c}$ of county c on day \mathbf{s} , thereby capturing time and county-level variations affecting COVID-19 spread. For a list of relevant features employed in this study, please refer to Appendix C.

To underscore the flexibility of the actual growth model (1), we also consider the potential growth model of each county's daily log incident case number, i.e., $\forall t \in \mathbb{Z}^+$,

$$\ln(\mathbf{I}_{s,c}^t) = \alpha(\mathbf{X}_{t,c}) + r(\mathbf{X}_{t,c})\mathbf{s} + \varepsilon_{t,c}. \quad (2)$$

Here $\ln(\mathbf{I}_{s,c}^t)$ represents the potential log incident case number of county c on day \mathbf{s} if COVID-19 growth in county c were to follow the day t spreading patterns consistently; \mathbb{Z}^+ denotes the set of positive integers, i.e., $\{1, 2, 3, \dots\}$ (Weisstein 2023). This potential outcome framework can be illustrated through the following matrix:

$$\begin{bmatrix} \ln(\mathbf{I}_{1,c}^1) & \ln(\mathbf{I}_{2,c}^1) & \ln(\mathbf{I}_{3,c}^1) & \cdots \\ \ln(\mathbf{I}_{1,c}^2) & \ln(\mathbf{I}_{2,c}^2) & \ln(\mathbf{I}_{3,c}^2) & \cdots \\ \ln(\mathbf{I}_{1,c}^3) & \ln(\mathbf{I}_{2,c}^3) & \ln(\mathbf{I}_{3,c}^3) & \cdots \\ \vdots & \vdots & \vdots & \ddots \end{bmatrix}. \quad (3)$$

Here, only the diagonal entries represent the actual log incident case numbers of county c on day \mathbf{s} , observable from the actual growth model (1). That is,

$$\ln(\mathbf{I}_{s,c}^s) = \ln(\mathbf{I}_{s,c}).$$

In contrast, the off-diagonal entries, i.e., $\ln(\mathbf{I}_{s,c}^t)$ where $s \neq t$, denote the potential log incident case number of county c on day s as if it were generated by day t 's growth model, which is a counterfactual outcome and is not observable from the actual growth model (1). Therefore, the specification of the actual growth model (1) essentially permits a unique data generating process for each data point. This reflects the reality that COVID-19 spreading patterns can vary day by day and county by county.

We are now ready to define the instantaneous county-level exponential growth rate $r_{t,c}$. As explained in the Introduction, $r_{t,c}$ can be defined as the expected natural logarithmic ratio of two consecutive days' incidence case numbers, conditional on the relevant features of county c on day t , i.e.,

$$r_{t,c} := \mathbb{E}\left[\ln\left(\frac{\mathbf{I}_{s,c}^t}{\mathbf{I}_{s-1,c}^t}\right) \mid \mathbf{X}_{t,c}\right]. \quad (4)$$

Notably, this definition is solely based on the potential growth model (2) rather than the actual growth model (1). In other words, the instantaneous county-level exponential growth rate $r_{t,c}$ only applies to county c on day t , without assuming that the same exponential growth rate applies to other counties or other days. Therefore, this definition allows each observed incidence case number $\ln(\mathbf{I}_{s,c})$ from the actual growth model (1) to have its own instantaneous county-level exponential growth rate $r_{s,c}$.

Finally, we characterize conditions under which potential growth models (2) follow exponential growths:

Assumption 1 (*Instantaneous Exponential Growth*)

$$\mathbb{E}[\ln(\mathbf{I}_{s,c}^t) \mid \mathbf{s}, \mathbf{X}_{t,c}] = \alpha(\mathbf{X}_{t,c}) + r(\mathbf{X}_{t,c})\mathbf{s} + \mathbb{E}[\varepsilon_{t,c} \mid \mathbf{X}_{t,c}].$$

Assumption 1 is not restrictive as it only specifies the potential growth model (2), granting full flexibility in the actual growth model (1). It ensures that (2) models an exponential growth, where the expected daily log of incident case numbers is a linear function of the day. That is,

LEMMA 1. *The instantaneous county-level exponential growth rate defined in (4) is encapsulated by the slope term in the potential growth model (2), i.e.,*

$$r_{t,c} = r(\mathbf{X}_{t,c}).$$

For the sake of brevity, all the proofs are included in Appendix E. Notably, the functional form of (2) does not guarantee this requirement. In fact, any growth model $\mathbb{E}[\ln(\mathbf{I}_{s,c}^t)|\mathbf{s}, \mathbf{X}_{t,c}] = \mathbf{f}(\mathbf{s})$ can be derived from (2) by setting $\mathbb{E}[r(\mathbf{X}_{t,c})\mathbf{s}|\mathbf{s}, \mathbf{X}_{t,c}] = r(\mathbf{X}_{t,c})\mathbf{s}$, $\mathbb{E}[\alpha(\mathbf{X}_{t,c})|\mathbf{s}, \mathbf{X}_{t,c}] = \alpha(\mathbf{X}_{t,c})$, and $\mathbb{E}[\boldsymbol{\varepsilon}_{t,c}|\mathbf{s}, \mathbf{X}_{t,c}] = \mathbf{f}(\mathbf{s}) - r(\mathbf{X}_{t,c})\mathbf{s} - \alpha(\mathbf{X}_{t,c})$.

Having presented a model of the instantaneous county-level exponential growth rate $\mathbf{r}_{t,c}$ in this section, §3.2 proceeds to characterize conditions that enable the identification of this model. To establish the context, let's consider a scenario with no heterogeneity in county-level instantaneous growth rates, i.e., $\forall t', t'' \in \{1, \dots, t\}$ and $c', c'' \in C$, $\alpha(\mathbf{X}_{t',c'}) = \alpha(\mathbf{X}_{t'',c''})$ and $r(\mathbf{X}_{t',c'}) = r(\mathbf{X}_{t'',c''})$. In this case, the actual growth model (1) simplifies to a homogeneous growth model, which is identifiable under Ordinary Least Squares (OLS) assumptions (c.f. Appendix §E.2). Nevertheless, with full heterogeneity in county-level instantaneous growth rates, i.e., $\forall t', t'' \in \{1, \dots, t\}$ and $c', c'' \in C$, $t' \neq t''$ or $c' \neq c'' \Rightarrow \alpha(\mathbf{X}_{t',c'}) \neq \alpha(\mathbf{X}_{t'',c''})$ and $r(\mathbf{X}_{t',c'}) \neq r(\mathbf{X}_{t'',c''})$, the actual growth model (1) is not identifiable under OLS assumptions as the data generating process contains twice as many parameters as the observable data points. Thus, specific assumptions are required to incorporate heterogeneity into the model while maintaining identifiability. We outline these assumptions in §3.2.

3.2. Model Identification

This section first presents the identification assumptions of the instantaneous county-level exponential growth rate in Theorem 1. Subsequently, we proceed to examine these assumptions, demonstrating that they are less restrictive and allow for more adaptive estimators compared to OLS assumptions.

Our identification requires a certain “overlap” assumption between the potential growth models (2):

Assumption 2 (*Overlap*)

$$\mathbb{E}[\ln(\mathbf{I}_{s,c}^t)|\mathbf{s} = t - 1, \mathbf{X}_{t,c}] = \mathbb{E}[\ln(\mathbf{I}_{s,c}^{t-1})|\mathbf{s} = t - 1, \mathbf{X}_{t-1,c}].$$

Assumption 2 requires that the potential growth models of $\ln(\mathbf{I}_{s,c}^t)$ and $\ln(\mathbf{I}_{s,c}^{t-1})$ overlap on the day $t - 1$ in expectation. In the absence of this assumption, only a *single data point* of the potential growth model $\ln(\mathbf{I}_{s,c}^t)$ can be observed from the data generated by the actual growth model (1). With a single observation, it is not possible to identify any

parameters, including $\mathbf{r}_{t,c}$, from the potential growth model $\ln(\mathbf{I}_{s,c}^t)$. Figure 1 illustrates a possible trajectory of $\mathbb{E}[\ln(\mathbf{I}_{s,c}^s)|\mathbf{s}, \mathbf{X}_{s,c}]$ in accordance with Assumptions 1 and 2, serving as an explanatory example. Theorem 1 demonstrates that $\mathbf{r}_{t,c}$ is identified under these two assumptions.

THEOREM 1. *The county-level instantaneous exponential growth rate $\mathbf{r}_{t,c}$ is identified as*

$$\mathbf{r}_{t,c} = \mathbb{E}[\ln(\mathbf{I}_{s,c}^t)|\mathbf{s} = t, \mathbf{X}_{t,c}] - \mathbb{E}[\ln(\mathbf{I}_{s,c}^{t-1})|\mathbf{s} = t-1, \mathbf{X}_{t-1,c}]. \quad (5)$$

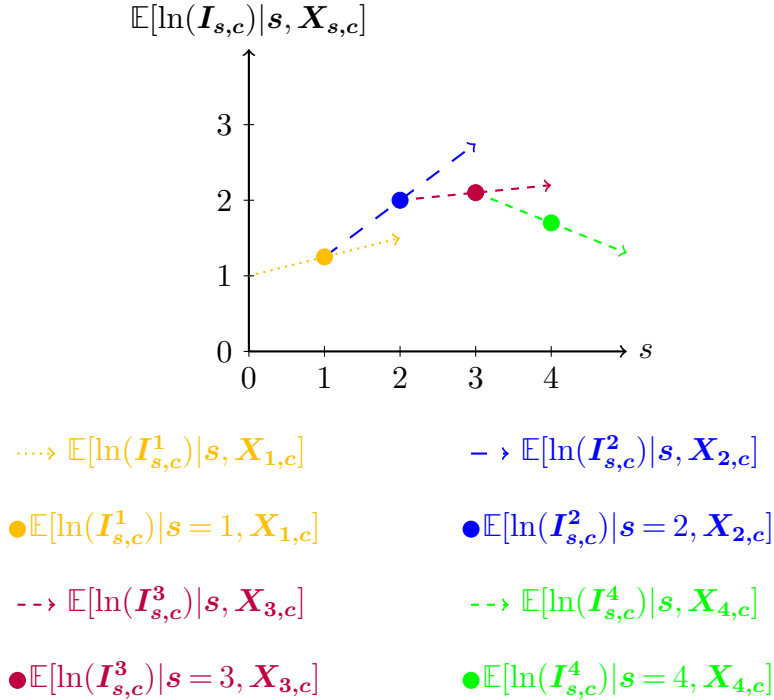


Figure 1 Each potential growth model, i.e., $\ln(\mathbf{I}_{s,c}^1)$, $\ln(\mathbf{I}_{s,c}^2)$, $\ln(\mathbf{I}_{s,c}^3)$, and $\ln(\mathbf{I}_{s,c}^4)$, can exhibit distinct patterns under Assumptions 1 and 2. The unobservable components of these potential growth models are indicated by dashed lines. The observable components of these potential growth models, which coincide with the actual growth model $\ln(\mathbf{I}_{s,c})$, are depicted as solid dots.

To illustrate the parsimonious nature of our identification assumptions, we provide a formal comparison between Assumptions 1 and 2 with the OLS identification assumptions in Appendix E.2. Specifically, we show that our identification assumptions are less restrictive than the OLS identification assumptions (c.f. Theorem 5 in Appendix E.2) and allow for more adaptive estimators compared to those derived from the OLS assumptions. (c.f.

Theorem 6 in Appendix E.2). Particularly, Theorem 6 demonstrates that any OLS estimators of $\mathbf{r}_{t,c}$ with a δ -day fitting window can be expressed as a convex combination of $\delta - 1$ two-point estimators in the form of (5), i.e.,

$$\hat{\mathbf{r}}_{t,c}^{ols(\delta)} = \sum_{t'=t-\delta+2}^t \hat{\mu}_{t',c} (\ln(\mathbf{I}_{t',c}) - \ln(\mathbf{I}_{t'-1,c})), \quad (6)$$

where $\{\hat{\mu}_{t',c}\}_{t' \in \{t-\delta+2, \dots, t\}}$ are non-negative weights that sum to 1, i.e.,

$$\hat{\mu}_{t',c} = \frac{\sum_{i=t'}^t (i - \frac{2t-\delta+1}{2})}{\sum_{i=t-\delta+1}^t (i - (t - \delta + 1))(i - \frac{2t-\delta+1}{2})}. \quad (7)$$

In summary, despite necessitating more stringent identification assumptions, the OLS estimator of the county-level instantaneous exponential growth rate (6) merely constitutes an ad hoc weighted average of the two-point estimators (5). Consequently, our identification assumptions are less constraining and more likely to reflect the COVID-19 transmission pattern.

4. Model Estimation

This section discusses how we estimate the instantaneous county-level exponential growth rate $\mathbf{r}_{t,c}$, defined in (4). To this end, §4.1 first derives the local moment condition and an initial estimate of $\mathbf{r}_{t,c}$. Subsequently, §4.2 improves this initial estimate by incorporating relevant proxy data through GRF and transfer learning. Pseudocode and implementation details of our proposed estimation algorithm, i.e., TLGRF, are presented in Appendix A.1. A detailed discussion of this algorithm’s stability with regard to its key hyperparameters is provided in Appendix G.1.

4.1. Local Moment Equation and Initial Estimator

To obtain an initial estimator for $\mathbf{r}_{t,c}$ identified under Assumptions 1 and 2, this section derives the local moment equation of the estimation problem and subsequently shows that this local moment equation can be estimated using a two-day “data block” $\{\ln(\mathbf{I}_{t,c}), \ln(\mathbf{I}_{t-1,c}), \mathbf{X}_{t,c}\}$.

To derive the relevant local moment equation, we first note that (5) can be rewritten as

$$r(\mathbf{X}_{t,c}) = \mathbb{E}[\ln(\mathbf{I}_{s,c}^t) | \mathbf{s} = t, \mathbf{X}_{t,c}] - \mathbb{E}[\ln(\mathbf{I}_{s,c}^t) | \mathbf{s} = t - 1, \mathbf{X}_{t,c}],$$

where the conditional moments $\mathbb{E}[\ln(\mathbf{I}_{s,c}^t)|\mathbf{s} = t, \mathbf{X}_{t,c}]$ and $\mathbb{E}[\ln(\mathbf{I}_{s,c}^t)|\mathbf{s} = t - 1, \mathbf{X}_{t,c}]$ are observable by their definitions and Assumption 2. For ease of expression, we proceed to transform and denote the dependent and independent variables as

$$\mathbf{Y}_{t,c}(\mathbf{s}) = \mathbb{1}_t(\mathbf{s}) \left(\mathbb{E}[\ln(\mathbf{I}_{s,c}^t)|\mathbf{s}, \mathbf{X}_{t,c}] - \mathbb{E}[\ln(\mathbf{I}_{s,c}^t)|\mathbf{s} = t - 1, \mathbf{X}_{t,c}] \right), \quad W_{t,c}(\mathbf{s}) = \mathbb{1}_t(\mathbf{s}). \quad (8)$$

As such, we have a local moment equation that identifies $\mathbf{r}_{t,c}$:

$$\mathbf{Y}_{t,c}(\mathbf{s}) = r(\mathbf{X}_{t,c})W_{t,c}(\mathbf{s}), \quad (9)$$

where $r(\mathbf{X}_{t,c}) = \mathbf{r}_{t,c}$ by Lemma 1.

Second, we derive an initial estimator of the instantaneous county-level exponential growth rate from the local moment equation (9). The derivation makes use of the following assumption, i.e.,

Assumption 3

$$\mathbb{E}[\mathbf{Y}_{t,c}(\mathbf{s})|\mathbf{X}_{t,c}] = r(\mathbf{X}_{t,c})\mathbb{E}[W_{t,c}(\mathbf{s})].$$

That is, the relevant features $\mathbf{X}_{t,c}$ only affect the change in incident COVID case numbers through the growth rate $r(\mathbf{X}_{t,c})$. As such, we have

THEOREM 2. *For any county $c \in C$ on any day $t \in \mathbb{Z}^+ \setminus \{1\}$ with realized features $x_{t,c}$, its instantaneous county-level exponential growth rate $\mathbf{r}_{t,c}$ can be estimated from data $\{\ln(\mathbf{I}_{t,c}), \ln(\mathbf{I}_{t-1,c}), x_{t,c}\}$ via the local moment condition*

$$\mathbb{E}[(\mathbf{Y}_{t,c}(\mathbf{s}) - r(\mathbf{X})W_{t,c}(\mathbf{s}))W_{t,c}(\mathbf{s})|\mathbf{X} = x_{t,c}] = 0, \quad (10)$$

which yields the following initial estimator:

$$\hat{\mathbf{r}}_{t,c} = \ln(\mathbf{I}_{t,c}) - \ln(\mathbf{I}_{t-1,c}). \quad (11)$$

We observe that (11) is the same as the two-point estimator (5), which is equivalent to an OLS estimator with a 2-day fitting widow as in (6). This estimator best captures the case growth rate of this county on this day but is noisy. To improve this initial estimator further, we propose a GRF-based estimator in §4.2, which adaptively chooses fitting windows by pooling data across space and time through transfer learning.

4.2. Transfer Learning through GRF

In §4.1, we showed that the target data $\{\ln(\mathbf{I}_{t,c}), \ln(\mathbf{I}_{t-1,c}), \mathbf{X}_{t,c}\}$ provides an initial estimator for the instantaneous county-level exponential growth rate $\mathbf{r}_{t,c}$. To further improve this initial estimator, we incorporate relevant proxy data $\{\ln(\mathbf{I}_{t',c'}), \ln(\mathbf{I}_{t'-1,c'}), \mathbf{X}_{t',c'}\}$ from other counties $c' \neq c$ and days $t' \neq t$ into the estimation through transfer learning.

Specifically, for any county $c \in C$ on any day $t \in \mathbb{Z}^+$ with relevant features $\mathbf{X}_{t,c}$, the GRF algorithm provides a similarity measure $\gamma_{t',c'}(\mathbf{X}_{t,c})$ between the target data $\{\ln(\mathbf{I}_{t,c}), \ln(\mathbf{I}_{t-1,c}), \mathbf{X}_{t,c}\}$ and the proxy data $\{\ln(\mathbf{I}_{t',c'}), \ln(\mathbf{I}_{t'-1,c'}), \mathbf{X}_{t',c'}\}$ from other counties $c' \neq c$ and days $t' \neq t$. For estimation, the GRF algorithm grows a forest $B := \{1, \dots, |B|\}$, where for each tree indexed by $b \in B$, the algorithm recursively partitions the training sample through an axis-aligned cut of relevant features based on the similarity of their underlying instantaneous county-level exponential growth rates. As such, training samples whose features fall into the same leaf as that of the target data, denoted as $L_b(\mathbf{X}_{t,c})$, are effectively used to estimate $\mathbf{r}_{t,c}$. The similarity measure, which we denote $\gamma_{t',c'}(\mathbf{X}_{t,c})$, is thus constructed as follows

$$\gamma_{t',c'}(\mathbf{X}_{t,c}) := \frac{1}{|B|} \sum_{b=1}^{|B|} \frac{\mathbb{1}(\{\mathbf{X}_{t',c'} \in L_b(\mathbf{X}_{t,c})\})}{|L_b(\mathbf{X}_{t,c})|}, \quad (12)$$

which measures how frequently each training sample $\{\ln(\mathbf{I}_{t',c'}), \ln(\mathbf{I}_{t'-1,c'}), \mathbf{X}_{t',c'}\}$ is in the same leaf as the target data $\{\ln(\mathbf{I}_{t,c}), \ln(\mathbf{I}_{t-1,c}), \mathbf{X}_{t,c}\}$, i.e., $\mathbf{X}_{t',c'} \in L_b(\mathbf{X}_{t,c})$. We note that this similarity measure essentially weights the proxy data based on its similarity to the target data, which resembles classical variance reduction techniques such as importance sampling (Sugiyama et al. 2008).

Given these similarity measures, we now present TLGRF estimator for the instantaneous county-level exponential growth rate $\mathbf{r}_{t,c}$. We start with an assumption commonly made for GRF estimation as follows:

Assumption 4 For any county $c \in C$ on any day $t \in \mathbb{Z}^+$ with realized features $x_{t,c}$, $\mathbb{E}[\mathbf{Y}_{t,c}(\mathbf{s}) | \mathbf{X} = x_{t,c}]$ is Lipschitz continuous in $x_{t,c}$.

That is, daily county-level COVID-19 incident case numbers are changing continuously with relevant features, which implies that proxy data whose features are close enough to that of the target data have similar underlying instantaneous county-level exponential

growth rates. As such, Assumption 4 allows us to estimate $\mathbf{r}_{t,c}$ using the entirety of data up to day t , i.e.,

$$\{\ln(\mathbf{I}_{t',c'}), \ln(\mathbf{I}_{t'-1,c'}), \mathbf{X}_{t',c'}\}_{t' \in [t], c' \in C} \text{ where } [t] := \{t' \in \{1, \dots, t\} | t \equiv t' \pmod{2}\},$$

where mod 2 is the standard modulo 2 operation such that

$$[t] := \begin{cases} \{1, 3, 5, \dots, t\} & , \text{ if } t \text{ is odd} \\ \{2, 4, 6, \dots, t\} & , \text{ if } t \text{ is even.} \end{cases}$$

Under these assumptions, the TLGRF estimator, as described in Theorem 3, is obtained.

THEOREM 3. *For any county $c, c' \in C$ on any day $t, t' \in \mathbb{Z}^+$ with realized features $x_{t,c}$ and $x_{t',c'}$ such that $x_{t',c'} \in \bigcup_{b \in B} L_b(x_{t,c})$, its instantaneous county-level exponential growth rate $\mathbf{r}_{t,c}$ can be estimated from data $\{\ln(\mathbf{I}_{t',c'}), \ln(\mathbf{I}_{t'-1,c'}), x_{t',c'}\}_{t' \in [t], c' \in C}$ via the weighted moment condition*

$$\sum_{t' \in [t]} \sum_{c' \in C} \gamma_{t',c'}(x_{t,c}) \mathbb{E}[(\mathbf{Y}_{t',c'}(\mathbf{s}) - r(x_{t,c})W_{t',c'}(\mathbf{s}))W_{t',c'}(\mathbf{s}) | \mathbf{X} = x_{t',c'}] = 0, \quad (13)$$

resulting in the following TLGRF estimator:

$$\hat{\mathbf{r}}_{t,c}^{TLGRF} = \sum_{t' \in [t]} \sum_{c' \in C} \gamma_{t',c'}(\mathbf{X}_{t,c}) (\ln(\mathbf{I}_{t',c'}) - \ln(\mathbf{I}_{t'-1,c'})). \quad (14)$$

We note that the initial estimator presented in Theorem 2 is a special case of the TLGRF estimator derived in Theorem 3. Specifically, if no proxy data is in the same leaf as the target data for all trees in the forest, i.e., $\bigcup_{b \in B} L_b(\mathbf{X}_{t,c}) = \{\mathbf{X}_{t,c}\}$, we would have a similarity measure concentrated at the target data, i.e., $\gamma_{t,c}(\mathbf{X}_{t,c}) = 1$ and $\gamma_{t',c'}(\mathbf{X}_{t,c}) = 0$ for all $t' \neq t$ or $c' \neq c$. In that case, the weighted moment condition (13) and the TLGRF estimator (14) reduce to the local moment condition (10) and the initial estimator (11), respectively.

To better understand the flexibility of the TLGRF estimator (14), we compare it with OLS estimators (6) with δ -day fitting windows. It is noteworthy that both estimators can be expressed as a convex combination of two-point estimators (5), i.e.,

$$\hat{\mathbf{r}}_{t,c}^{TLGRF} = \sum_{t' \in [t]} \sum_{c' \in C} \gamma_{t',c'}(\mathbf{X}_{t,c}) (\ln(\mathbf{I}_{t',c'}) - \ln(\mathbf{I}_{t'-1,c'})) \quad (15)$$

and

$$\hat{\mathbf{r}}_{t,c}^{ols(\delta)} = \sum_{t'=t-\delta+2}^t \hat{\mu}_{t',c} (\ln(\mathbf{I}_{t',c}) - \ln(\mathbf{I}_{t'-1,c})) \quad (16)$$

The main difference between these two classes of estimators is that the weights of the TLGRF estimator (15) are adaptive to the relevant features, while the weights of the OLS estimators (16), as specified in (7), are non-adaptive. In other words, by allowing for more flexible weighting, the TLGRF estimator (14) generalizes the OLS estimators with non-adaptive fitting windows. A formal analysis of how these two fitting window selection approaches affect the bias-variance tradeoff of their corresponding estimators are presented in Appendix E.4.

To summarize, in order to improve the estimation, our proposed algorithm adaptively chooses fitting windows by pooling proxy data across time and counties via the GRF similarity measures. In §5 and §6, we evaluate the numerical performance of our estimator by benchmarking it against traditional estimators with both non-adaptive fitting windows and fitting windows chosen via time series cross-validation, as well as the classical GRF algorithm by Athey et al. (2019).

5. Performance Evaluation Against Other Fitting Window Size Selection Methods

This section empirically assesses the performance of TLGRF algorithm. Specifically, we compare the prediction of TLGRF algorithm against true case numbers 7 days ahead and report two well-established prediction accuracy measures in the epidemiology and operations management literature, i.e., the mean absolute error (MAE) and root-mean-squared error (RMSE) (Bertsimas et al. 2021). That is, to predict the COVID-19 incident case number $\hat{\mathbf{I}}_{t+7,c}$ at county c on day $t+7$, we first estimate the instantaneous county-level growth rate at county c on day t , and generate the prediction as follows

$$\hat{\mathbf{I}}_{t+7,c} = e^{\ln(\mathbf{I}_{t,c}) + 7\hat{\mathbf{r}}_{t,c}}. \quad (17)$$

Therefore, the prediction accuracy depends solely on the instantaneous county-level growth rate estimate $\hat{\mathbf{r}}_{t,c}$.

In line with the paper’s central premise, our comparison primarily concentrates on varying techniques for estimating exponential growth rates, particularly emphasizing the differences in fitting window selection. Specifically, selecting fitting windows essentially involves determining the weights $\{w_{t',c'}\}_{t' \in \{2, \dots, t\}, c' \in C}$ for estimating $\mathbf{r}_{t,c}$:

$$\sum_{c' \in C} \sum_{t'=2}^t w_{t',c'} (\ln(\mathbf{I}_{t',c'}) - \ln(\mathbf{I}_{t'-1,c'})).$$

For example, Theorem 6 demonstrates that any OLS estimators of $\mathbf{r}_{t,c}$ with a δ -day fitting window can be expressed as

$$\hat{\mathbf{r}}_{t,c}^{ols(\delta)} = \sum_{c' \in C} \sum_{t'=2}^t w_{t',c'} (\ln(\mathbf{I}_{t',c'}) - \ln(\mathbf{I}_{t'-1,c'})).$$

Here the weights $w_{t',c} = \hat{\mu}_{t',c} \quad \forall t' \in \{t - \delta + 2, \dots, t\}$ are defined in accordance with (7), while $w_{t',c'} = 0 \quad \forall t' \in \{2, \dots, t - \delta + 1\}$ or $\forall c' \in C \setminus \{c\}$. In this section, we compare the weight assignment scheme of TLGRF, as specified in Theorem 3, against three classes of weight assignment methods. First, we demonstrate that TLGRF consistently outperforms all fixed window size choices in §5.1. Then, in §5.2, we show that TLGRF also outperforms dynamic window size algorithms that pool data and conduct cross validation across time. Finally, in §5.3, we conduct a comparison between the empirical performance of TLGRF and K-Means Dynamic Window size algorithms. Similar to TLGRF, this algorithm is capable of pooling data and performing cross validation across both time and space. Through this analysis, we provide evidence that the superiority of TLGRF stems not only from its capacity to pool data across time and space, but also from its adaptive weighting schemes as outlined in Theorem 3. In contrast, we note that alternative fitting window choice algorithms rely, at least partially, on non-adaptive OLS weight assignments (7). Properties of the benchmarks against which we compare TLGRF are summarized in Table 1.

Lastly, we remark that while there are many COVID-19 prediction algorithms and time series clustering methods (c.f. Wynants et al. 2020, Ma et al. 2019), few of them aim to improve the estimation of exponential growth rate, which is the main focus of this paper. In this section, we only include those benchmarking algorithms that are capable of estimating exponential growth rates for comparison.

(Estimator)	Cross Validation Across Space	Cross Validation Across Time	Weighting Schemes
Fixed Windows			OLS
Dynamic Windows		✓	OLS
K-Means Dynamic Windows	✓	✓	OLS
TLGRF	✓	✓	GRF

Table 1 Comparison of exponential growth rate estimators: Fixed Window Size Method, Dynamic Window Size Method, i.e., Time-based Cross Validation (tcv) and County and Time-based Cross Validation (ctcv), K-means Dynamic Window Size Method, and TLGRF

5.1. Performance Comparison Against Fixed Window Size Methods

In this section, we compare the empirical performance of TLGRF against fixed window size methods. As established in Theorem 6 of Appendix E.2, any OLS estimators of $r_{t,c}$ with a δ -day fitting window can be expressed as

$$\hat{r}_{t,c}^{ols(\delta)} = \sum_{t'=t-\delta+2}^t \hat{\mu}_{t',c} (\ln(\mathbf{I}_{t',c}) - \ln(\mathbf{I}_{t'-1,c})), \quad (18)$$

where $\{\hat{\mu}_{t',c}\}_{t' \in \{t-\delta+2, \dots, t\}}$ are the OLS weights (7).

Figure 2 characterizes the performance of TLGRF against algorithms with fixed 2-, 7-, and 14-fitting window sizes, starting from the first day of recorded COVID-19 cases in NYTimes COVID-19 dataset (The New York Times 2020). The results summarized in this figure show that TLGRF consistently outperforms all the fixed window-size algorithms after April 2020, when there were enough proxy data to conduct transfer learning. In addition, Table 2 demonstrates that TLGRF achieves MAE 0.127 and RMSE 0.195, which are respectively 27.4% and 42.5% lower than their closest competitors. Therefore, TLGRF reliably estimates the instantaneous county-level growth rates, including those counties with small sample sizes, and outperforms all fixed window-size algorithms with the help of transfer learning. Additional results on the comparison between TLGRF and fixed window size algorithms are available in Appendix §F.1.

In addition, this experiment also shows that there is no clear winner among the fixed window size algorithms considered, indicating that optimal window sizes for different counties are different and change over time. To see this, please observe that even though Table 2 shows Fixed Window 2 has the lowest median MAE and RMSE compared to the other

fixed window-size algorithms, Figure 2 reveals that Fixed Window 2 has been outperformed by others fitting window size choices on many different days. This is because, at different time points of the pandemic, the rate of spread varies, and no fixed time window algorithm has the flexibility to capture this changing nature of disease epidemiology.

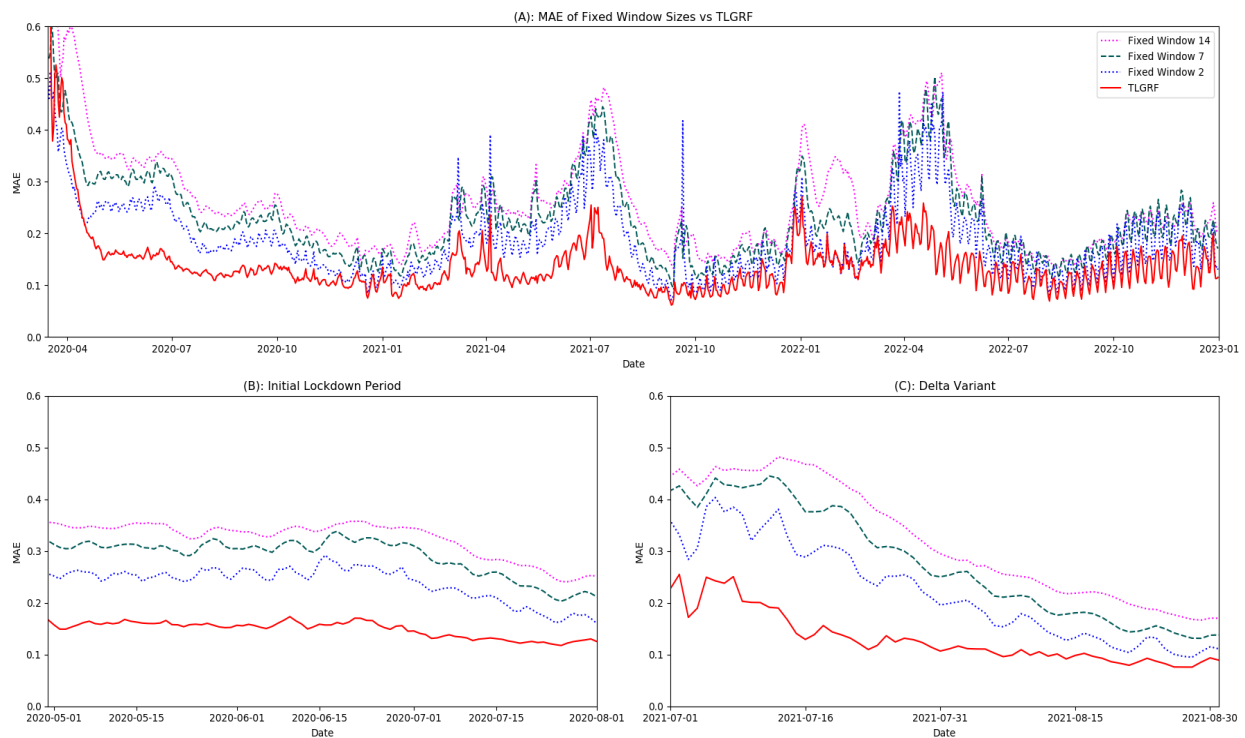


Figure 2 MAE plot of prediction accuracy (TLGRF vs. Fixed 2-, 7-, and 14-Day Fitting Window): Plot A (Top) shows the MAE comparison across the study period. Plot B (bottom left) zooms in on the initial lockdown period. Plot C (bottom right) zooms in on the period during the outbreak of the Delta variant.

Method	MAE	RMSE
Fixed Window 14	0.240	0.373
Fixed Window 7	0.213	0.365
Fixed Window 2	0.175	0.339
TLGRF	0.127	0.195

Table 2 Median MAE and RMSE of TLGRF vs. Fixed Window 2-, 7-, and 14-Day Fitting Window

5.2. Performance Comparison Against Dynamic Window Methods

While most existing literature is predominantly occupied by fixed window-size methods, relatively recent epidemiology literature has started to treat the window size as a hyperparameter that could dynamically change over time (Ben Phillips 2020, Chowell et al. 2007). Motivated by these studies, we adopt a similar approach in this section and treat the window size as a hyperparameter that can change over time. More precisely, our approach involves dynamically selecting the appropriate window size δ_t using cross validation and applying it uniformly across all U.S. counties. We refer to this approach as the Time-based Cross Validation (**tcv**) algorithm, which yields the following estimator:

$$\hat{\mathbf{r}}_{t,c}^{ols(\delta_t)} = \sum_{t'=t-\delta_t+2}^t \hat{\mu}_{t',c} (\ln(\mathbf{I}_{t',c}) - \ln(\mathbf{I}_{t'-1,c})), \quad (19)$$

where $\{\hat{\mu}_{t',c}\}_{t' \in \{t-\delta_t+2, \dots, t\}}$ are the OLS weights (7). Notably, the primary distinction between the **tcv** estimator (19) and the fixed window size estimator (18) is that the **tcv** algorithm dynamically selects the window size δ_t through cross-validation, whereas the fixed window size estimator (18) employs a predetermined fixed window size δ . Further details and implementation specifics of the Dynamic Window estimation algorithms are provided in Appendix A.2.

In addition, we consider another benchmarking algorithm that adjusts fitting window sizes dynamically at the county level, which we refer to as County Time-based Cross Validation (**ctcv**). That is, this algorithm dynamically selects the appropriate fitting window size $\delta_{t,c}$ for each county using cross validation, and yields the following estimator:

$$\hat{\mathbf{r}}_{t,c}^{ols(\delta_{t,c})} = \sum_{t'=t-\delta_{t,c}+2}^t \hat{\mu}_{t',c} (\ln(\mathbf{I}_{t',c}) - \ln(\mathbf{I}_{t'-1,c})). \quad (20)$$

Again, $\{\hat{\mu}_{t',c}\}_{t' \in \{t-\delta_{t,c}+2, \dots, t\}}$ represent the OLS weights (7). Unlike the **tcv** estimator (19), where a uniform fitting window size δ_t is selected for all U.S. counties each day, the **ctcv** estimator (20) chooses a distinct fitting window size $\delta_{t,c}$ for each county on a daily basis by cross validating at the county-level. For more comprehensive information and implementation details of the **ctcv** estimation algorithm, please refer to Appendix A.2.2.

The performance comparison results between **tcv/ctcv** and **TLGRF** are summarized in Table 3 and Figure 3. As seen in Table 3, **TLGRF** outperforms **tcv** and **ctcv** with respect to both median MAE and RMSE, with **TLGRF** outperforming them by over 27.4% in terms

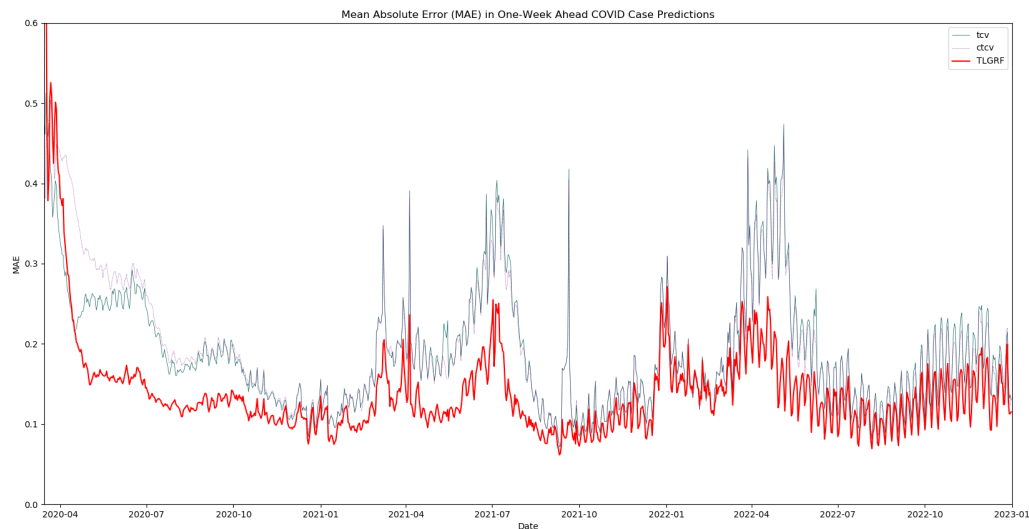


Figure 3 MAE plot of prediction accuracy (TLGRF vs. Time-based Cross Validation (tcv) and County Time-based Cross Validation (ctcv))

Method	MAE	RMSE
tcv	0.175	0.337
ctcv	0.175	0.314
TLGRF	0.127	0.195

Table 3 Median MAE and RMSE of TLGRF vs tcv and ctcv

of median MAE and 37.7% in terms of RMSE. Furthermore, a review of Figure 3 reveals that the outperformance of TLGRF over tcv and ctcv is consistent across days throughout the study period considered. These findings overall indicate that the ability to transfer learn across counties enables TLGRF to improve its performance against other dynamic window-size tuning algorithms. Please refer to Appendix §F.2 for additional results on the comparison of performance between TLGRF and tcv/ctcv.

5.3. Performance Comparison Against K-Means Dynamic Window Methods

This section investigates a method that selects the best fitting windows between two extremes: the tcv and ctcv algorithms. Specifically, the tcv algorithm performs cross validation at the national level, thereby determining a single dynamic fitting window, δ_t , applicable to all counties on each day t . In contrast, the ctcv algorithm implements

cross validation exclusively at the county level, thus establishing a unique dynamic fitting window, $\delta_{t,c}$, for each individual county c on each day t . Between these two extremes, a spectrum of fitting window size selection methods exists.

Investigation of this spectrum can be achieved through the utilization of k-means clustering methods. This involves partitioning all the U.S. counties into K clusters, with counties within each cluster sharing similar time-invariant characteristics, such as the geographical coordinates of county centroids. For each resulting cluster $C_k \in \{C_1, \dots, C_K\}$, cross validation can be performed internally to dynamically determine a fitting window size $\delta_{t,k}$, which will be applicable to all counties in the specific cluster on each day t . This procedure is denoted as the K-Means Dynamic Window algorithm. The resultant estimator is defined as follows: $\forall c \in C_k$,

$$\hat{\mathbf{r}}_{t,c}^{ols(\delta_{t,k})} = \sum_{t'=t-\delta_{t,k}+2}^t \hat{\mu}_{t',c} (\ln(\mathbf{I}_{t',c}) - \ln(\mathbf{I}_{t'-1,c})). \quad (21)$$

Again, $\{\hat{\mu}_{t',c}\}_{t' \in \{t-\delta_{t,k}+2, \dots, t\}}$ represent the OLS weights (7). Notably, when there is only 1 cluster, the K-Means Dynamic Window estimator (21) reduces to the `tcv` estimator (19). In contrast, when each county forms its own cluster, the K-Means Dynamic Window estimator (21) becomes the `ctcv` estimator (20). Additional procedural details for the K-Means Dynamic Window algorithm can be found in Appendix A.2.3.

This section benchmarks the empirical performance of TLGRF against the optimal K-Means Dynamic Window estimators. Here, optimality is defined by the selection of the number of clusters K . Specifically, TLGRF is gauged against the K-Means Dynamic Window estimators with $K = 800$ and $K = 3100$ as these particular values of K yield the lowest median MAE and RMSE, respectively. The respective performances of all K-Means Dynamic Window estimators' MAE and RMSE, based on the number of clusters K , are illustrated in Figures 12 and 13 of Appendix §F.3.

The performance comparison results between the K-Means Dynamic Window method and TLGRF are presented in Table 4. As highlighted in Table 4, TLGRF surpasses the K-Means Dynamic Window estimators in both median MAE and RMSE metrics, exceeding their performance by over 26.6% in median MAE and 37.7% in RMSE. Furthermore, Figure 4 indicates that the TLGRF's superior performance over the K-Means Dynamic Window method is sustained throughout the study period. For more details of the performance of the K-Means Dynamic Window methods, please refer to Appendix §F.3.

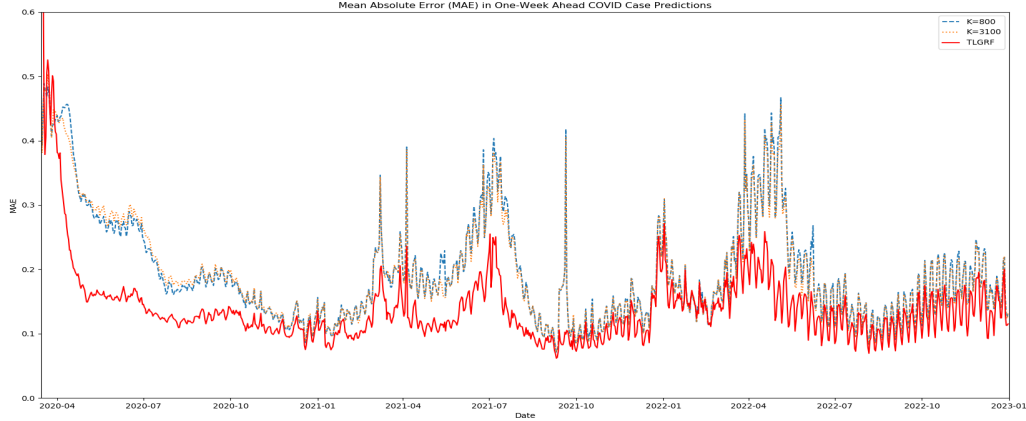


Figure 4 MAE plot of prediction accuracy (TLGRF vs. K-Means Dynamic Window Estimators with choices $K = 800$ and $K = 3100$)

Method	MAE	RMSE
K=800	0.173	0.333
K=3100	0.175	0.313
TLGRF	0.127	0.195

Table 4 Median MAE and RMSE of TLGRF vs. K-Means Dynamic Window: The K-Means Dynamic Window estimators achieve the lowest median MAE and RMSE when $K = 800$ and $K = 3100$, respectively.

These findings indicate that the enhanced effectiveness of TLGRF is attributed not only to its ability to aggregate data and perform cross-validation across both time and space but also to its adaptive weighting schemes. It is noteworthy that all benchmarking methods examined in this section rely on non-adaptive OLS weights (7). For example, K-Means Dynamic Window method alternate between different OLS weight assignments $\{\hat{\mu}_{t',c}\}_{t' \in \{t-\delta_{t,k}+2, \dots, t\}}$ through varying the fitting window size hyperparameter $\delta_{t,k}$. In contrast, the weights of TLGRF estimator, i.e., $\{\gamma_{t',c'}(\mathbf{X}_{t,c})\}_{t' \in [t], c \in C}$, are fully adaptive and are not constrained by the OLS weighting schemes. We delve deeper into this aspect in §6.

6. Performance Evaluation Against Other GRF Algorithms

This section elaborates on the distinct strengths of TLGRF by providing a detailed comparison with other types of GRF estimators. The properties of these estimators are compared to those of TLGRF in Table 5. Specifically, §6.1 expands on how the classical GRF algorithm

(Estimator)	Time-invariant Features	Time-varying Features	Weighting Schemes
Classical GRF	✓		OLS+GRF
TLGRF- δ ($\delta > 2$)	✓	✓	OLS+GRF
TLGRF	✓	✓	GRF

Table 5 Comparison of exponential growth rate estimators: Classical GRF, TLGRF- δ , and TLGRF

(c.f. [Athey et al. 2019](#)) can be deployed to estimate county-level instantaneous exponential growth rates and assess its empirical performance. Particularly, we highlight the limitation of the classical GRF algorithm in incorporating time-varying features in the estimations. §6.2 investigates a modified version of TLGRF, denoted as TLGRF δ , which incorporates OLS weights into its weighting schemes. An empirical comparison is conducted to evaluate the respective performances of TLGRF and TLGRF δ . §6.3 summarizes this section, emphasizing that the main strengths of the proposed TLGRF algorithm reside in its fully adaptive weighting schemes.

6.1. Performance Comparison Against Classical GRF

This section compares TLGRF against the classical GRF method (c.f. [Athey et al. 2019](#)). Both algorithms exploit the power of splitting upon feature data to improve the growth rate parameter estimates. However, TLGRF is better equipped to handle time-varying features as compared to GRF. To illustrate this point, we first present empirical evidence showing that GRF cannot effectively incorporate time-varying features. This is followed by a theoretical exposition elucidating the limitations of GRF and illustrating how TLGRF addresses these shortcomings.

6.1.1. Empirical Evidence

First, we provide empirical evidence that GRF does not effectively utilize time-varying features in its estimation. As illustrated in [Figure 5](#) and [Table 6](#), incorporating time-varying features into the classical GRF model yields only a marginal enhancement in performance. For more results on the performance comparison between TLGRF and classical GRF, please refer to [Appendix F.4](#).

Moreover, it remains ambiguous whether this improvement is attributable to the effective utilization of temporal information. This ambiguity arises because all features employed

in this study, whether time-invariant or time-varying, inherently contain spatial information. For example, the county-level vaccination coverage rate is a time-varying feature, yet its dynamics are significantly shaped by state-specific policies, which reveal geographic information. Consequently, the performance improvement observed when time-varying features such as vaccination coverage rate are included could also be ascribed to the spatial information embedded within these features.

In summary, the classical GRF model that incorporates all features demonstrates only a marginal performance improvement over its counterpart that utilizes solely time-invariant features, and it is markedly outperformed by the TLGRF.

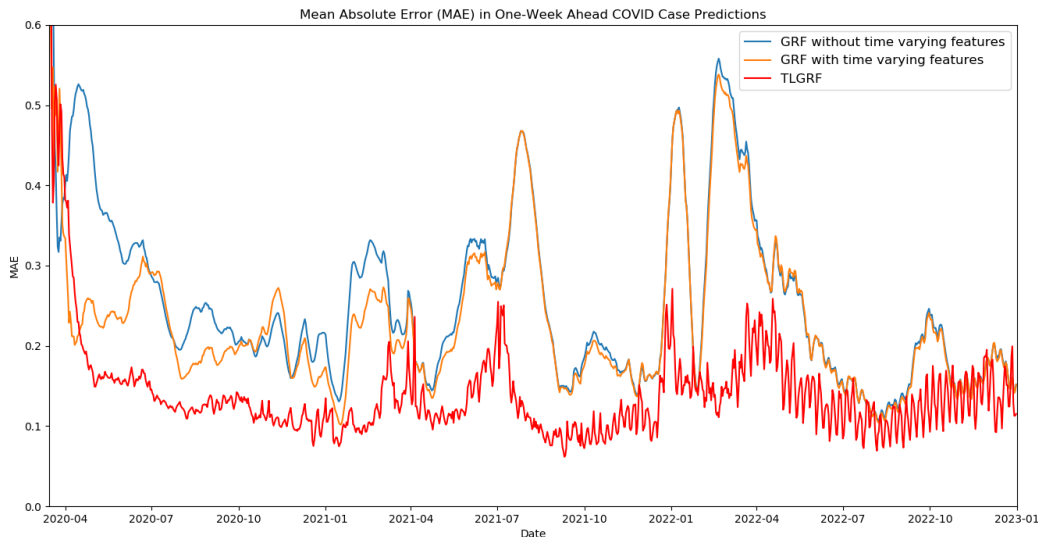


Figure 5 MAE plot of prediction accuracy (TLGRF vs. Classical GRF with/without Time-varying Features)

Method	MAE	RMSE
Classical GRF without time varying features	0.218	0.291
Classical GRF with time varying features	0.204	0.275
TLGRF	0.127	0.195

Table 6 Median MAE and RMSE of TLGRF vs. Classical GRF without time varying features and Classical GRF with time varying features

Dependent Variable ($\ln(\mathbf{I}_{s,c})$)	Independent Variable (\mathbf{s})	Feature (\mathbf{X})
$\ln(I_{1,1})$	1	$x_{1,1}$
$\ln(I_{2,1})$	2	$x_{2,1}$
\vdots	\vdots	\vdots
$\ln(I_{t,1})$	t	$x_{t,1}$
$\ln(I_{1,2})$	1	$x_{1,2}$
$\ln(I_{2,2})$	2	$x_{2,2}$
\vdots	\vdots	\vdots

Table 7 Data Structure Overview

6.1.2. Theoretical Justifications

This section clarifies the limitations of classical GRF in estimating the county-level instantaneous exponential growth rates. Specifically, when the independent variable (\mathbf{s}) takes non-binary values as indicated in Table 7, the classical GRF algorithm estimates a conditional average partial effect (CAPE), i.e.,

$$\frac{\text{Cov}[\ln(\mathbf{I}_{s,c}), \mathbf{s} | \mathbf{X} = x]}{\text{Var}[\mathbf{s} | \mathbf{X} = x]} \quad (22)$$

for each feature realization $x \in \{x_{1,1}, \dots, x_{t,|C|}\}$ (Tibshirani et al. 2023). As shown in Theorem 4 of Appendix E.2, the parameter of interest ($\mathbf{r}_{t,c}$) is captured by the CAPE with $X = x_{t,c}$. However, when the feature realization is time-varying, i.e., $\exists t' \in \{1, \dots, t\}$, $x_{t',c} \neq x_{t,c}$, a key identification assumption of the classical GRF method is violated. More precisely, according to Theorem 6, the CAPE (22) with $X = x_{t,c}$ can be expressed as

$$\frac{\text{Cov}[\ln(\mathbf{I}_{s,c}), \mathbf{s} | \mathbf{X} = x_{t,c}]}{\text{Var}[\mathbf{s} | \mathbf{X} = x_{t,c}]} = \sum_{t^-=2}^t \boldsymbol{\mu}_{t^-,c} (\mathbb{E}[\ln(\mathbf{I}_{s,c}) | \mathbf{s} = t^-, \mathbf{X} = x_{t,c}] - \mathbb{E}[\ln(\mathbf{I}_{s,c}) | \mathbf{s} = t^- - 1, \mathbf{X} = x_{t,c}]), \quad (23)$$

where $\{\boldsymbol{\mu}_{t^-,c}\}_{t^-\in\{1,\dots,t\}}$ are non-negative weights that add up to 1, as specified in (48). When the feature realization is time-varying, i.e., $x_{t',c} \neq x_{t,c}$, the conditional expectation $\mathbb{E}[\ln(\mathbf{I}_{s,c}) | \mathbf{s} = t', \mathbf{X} = x_{t,c}]$ in (23) is not identifiable as the relevant data, i.e., $(\ln(I_{t',c}), t', x_{t,c})$, is not observable in Table 7. Consequently, incorporating time-varying features essentially compromises the assumption of population overlap, i.e., $\forall t' \in \{1, \dots, t\}$,

$$0 < \mathbb{P}[\mathbf{s} = t', \mathbf{X} = x_{t,c}] < 1, \quad (24)$$

which is a key identification assumption of causal inference methods like GRF (D’Amour et al. 2021).

Therefore, certain constraints on the incorporated features are essential to enable the application of classical GRF for county-level instantaneous exponential growth rate estimations. A practical constraint is the inclusion of only time-invariant features such that $\forall c \in C, \forall t' \in \{1, \dots, t\}, x_{t',c} = x_c$. The population overlap assumption (24) is naturally satisfied under this constraint since $\forall t' \in \{1, \dots, t\}$,

$$\mathbb{P}[\mathbf{s} = t', \mathbf{X} = x_c] = \frac{1}{t}.$$

Therefore, under this constraint, the CAPE (22) with time-invariant features $X = x_c$ becomes identifiable.

Constraining features to time-invariant only $\{X_{c'}\}_{c' \in C}$ allows us to construct the similarity measure $\{\alpha'_{c'}(x)\}_{c' \in C}$ as defined by Athey et al. (2019), i.e.,

$$\alpha_{c'}(x) := \frac{1}{|B|} \sum_{b=1}^{|B|} \frac{\mathbb{1}(\{\mathbf{X}_{c'} \in L_b(x)\})}{|L_b(x)|}.$$

As such, the classical GRF estimator is obtained by weighing the sample counterpart of CAPE (23) with the GRF similarity measure $\{\alpha'_{c'}(x)\}_{c' \in C}$, i.e.,

$$\hat{\mathbf{r}}_{t,c}^{GRF} = \sum_{c' \in C} \alpha_{c'}(x) \sum_{t'=2}^t \hat{\mu}_{t',c} (\ln(\mathbf{I}_{t',c'}) - \ln(\mathbf{I}_{t'-1,c'})).$$

Notably, the classical GRF method cannot achieve fully adaptive weight allocations due to the OLS weights (7) inherited from the CAPE estimate, namely $\{\hat{\mu}_{t',c}\}_{t' \in \{2, \dots, t\}}$.

In conclusion, the disparity in performance between TLGRF and the classical GRF stems from two sources. First, to satisfy the population overlap assumption in the CAPE estimation, the classical GRF is constrained to use time-invariant features. Our analysis of feature importance in Appendix D.3 demonstrates that time-varying features, like the number of days since school closures were implemented, are the main contributors to the transfer learning ability of TLGRF. In contrast, time-invariant features like geographical location are way less important. Second, when estimating the CAPE, the classical GRF method would incorporate the OLS weights, leading to a failure in adaptive weights assignments. Therefore, TLGRF’s capabilities in leveraging time-varying features and adaptive weight assignments are the two key sources of its greatly improved performance.

6.2. Performance Comparison Against TLGRF δ

This section provides an extension to Theorem 2 and Theorem 3 by allowing initial estimators to have fitting window sizes exceeding $\delta = 2$. This extension essentially merges OLS weights with TLGRF weighting schemes. Specifically, under the additional assumptions specified in Theorem 7, the initial estimator of TLGRF δ becomes an OLS estimator with a δ -day fitting window, i.e.,

$$\hat{\mathbf{r}}_{t,c}^{ols(\delta)} = \sum_{t^- = t - \delta + 2}^t \hat{\mu}_{t^-,c} (\ln(\mathbf{I}_{t^-,c}) - \ln(\mathbf{I}_{t^- - 1,c})), \quad (25)$$

which coincides with the TLGRF initial estimator (11) only when $\delta = 2$. Additionally, Theorem 8 demonstrates that these initial estimators yield the subsequent TLGRF δ estimator, i.e., $\forall \delta \in \{2, \dots, t\}$,

$$\hat{\mathbf{r}}_{t,c}^{TLGRF(\delta)} = \sum_{t^- = t - \delta + 2}^t \hat{\mu}_{t^-,c} \sum_{c' \in C} \sum_{t' \in [t^-]} \gamma_{t',c'}(\mathbf{X}_{t^-,c}) (\ln(\mathbf{I}_{t',c'}) - \ln(\mathbf{I}_{t' - 1,c'})). \quad (26)$$

where the non-adaptive weights $\{\hat{\mu}_{t^-,c}\}_{t^- \in \{t - \delta + 2, \dots, t\}}$ are specified in (7). Notably, the TLGRF δ estimator (26) reduces to the TLGRF estimator (14) only when $\delta = 2$. Detail derivations of (26) are presented in Appendix E.3.

As depicted in Table 8, the median RMSE and MAE values of the TLGRF algorithm are presented for various selections of δ . Additionally, Figure 6 illustrates the daily mean MAE values corresponding to different choices of $\delta = 2$ vs $\delta = 4$ for clarity (see comparisons with other choices of δ in Appendix F.6). The numerical findings provide evidence of TLGRF's capacity to generalize effectively across diverse weighting schemes, with the results indicating that the most adaptable scheme, namely $\delta = 2$, exhibits the most favorable empirical performance.

6.3. TLGRF's Key Advantage over GRF: Fully Adaptive Weighting

A salient characteristic of TLGRF is its ability to implement fully adaptive weight allocations. This uniqueness is evident when compared with other methods, as consolidated in Tables 1 and 5, where TLGRF emerges as the sole estimator free from the dependency on non-adaptive OLS weights. The superior empirical performance of the TLGRF estimators, as evidenced in the evaluations detailed in §5 and §6, is a result of this adaptable weighting scheme.

Method	MAE	RMSE
TLGRF 14	0.173	0.237
TLGRF 7	0.153	0.226
TLGRF 4	0.138	0.217
TLGRF 3	0.132	0.203
TLGRF ($\delta=2$)	0.127	0.195

Table 8 Median MAE and RMSE of TLGRF vs. TLGRF δ : TLGRF corresponds to TLGRF δ with $\delta = 2$.

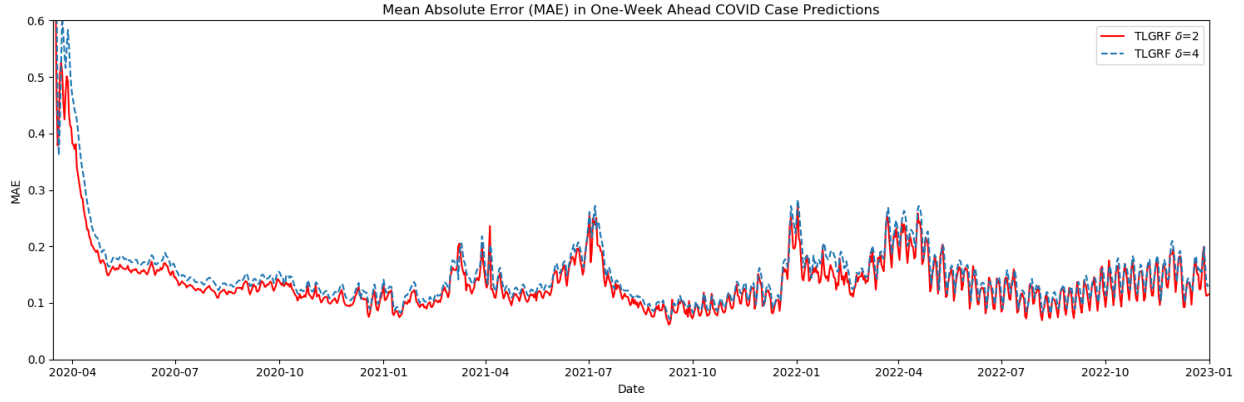


Figure 6 MAE plot of prediction accuracy (TLGRF with choices $\delta = 2$ vs $\delta = 4$)

As demonstrated in §6.2, this adaptive advantage is particularly pronounced in the performance comparison among TLGRF δ estimators with varying δ values. With an increasing δ , the OLS weighting scheme progressively redistributes weights from the estimator formed by target data, symbolized by $\ln(\mathbf{I}_{t,c}) - \ln(\mathbf{I}_{t-1,c})$, to the estimators created from proxy data, represented by $\ln(\mathbf{I}_{t',c'}) - \ln(\mathbf{I}_{t'-1,c'})$ where $t' \neq t$ and $c' \neq c$. This shift results in a declining empirical performance for larger δ values, which is expected given the fixed and non-adaptive nature of its weight reallocation. In fact, the target data OLS weight $\hat{\mu}_{t,c}$ in the TLGRF δ estimator (26) can be explicitly determined as a function of its initial estimator (25)'s fitting window size δ , as follows:

$$\hat{\mu}_{t,c} = \frac{\sum_{i=t}^t (i - \frac{2t-\delta+1}{2})}{\sum_{i=t-\delta+1}^t (i - (t - \delta + 1))(i - \frac{2t-\delta+1}{2})} = \frac{\frac{\delta-1}{2}}{\sum_{i=0}^{\delta-1} i(i - \frac{\delta-1}{2})}.$$

Therefore, the OLS weight is concentrated on the target data, i.e., $\hat{\mu}_{t,c} = 1$, if and only if $\delta = 2$. Moreover, as demonstrated in Lemma 4, the distribution of OLS weights is generally

not concentrated toward the target data. Specifically, when $\delta = 3$, we have $\hat{\mu}_{t,c} = \hat{\mu}_{t-1,c}$, whereas for $\delta > 3$, the following ordering prevails:

$$\hat{\mu}_{t,c} < \cdots < \hat{\mu}_{\lfloor \frac{2t-\delta+2}{2} \rfloor, c} = \hat{\mu}_{\lceil \frac{2t-\delta+2}{2} \rceil, c} > \cdots > \hat{\mu}_{t-\delta+2, c}.$$

Consequently, any estimators depending on OLS weighting schemes $\{\hat{\mu}_{t^-,c}\}_{t^- \in \{t-\delta+2, \dots, t\}}$ with $\delta > 2$ are not fully adaptive, leading to arbitrary weight shifts from target data to proxy data.

More generally, the key advantage of TLGRF over other GRF-style algorithms lies in its full flexibility of weight assignments when estimating CAPEs in the form of (23). As demonstrated in §6.1, the feasibility of this estimation task hinges upon the satisfaction of the population overlap assumption (24). A practical approach to fulfill this assumption is to assume that features within a specific δ fitting windows are sufficiently similar so that $r(\mathbf{X}_{t,c}) = r(\mathbf{X}_{t^-,c})$ for all $t^- \in \{t - \delta + 1, \dots, t\}$, as exemplified by **OLS Assumption 2** (Homogeneity) in Appendix E.2. Nevertheless, this approach is susceptible to introducing non-adaptive OLS weighting schemes when $\delta > 2$, resulting in ad hoc weight shifts from target data to proxy data. In contrast, TLGRF is anchored on a more robust identification assumption, namely, **Assumption 2** (*Overlap*). This assumption enables the identification of CAPE with treatment-correlated features without necessitating the inclusion of non-adaptive OLS weighting schemes. This crucial advantage underlines the potential of TLGRF to extend beyond the confines of county-level instantaneous growth rate estimation, the primary focus of this paper. We discuss these extensions of TLGRF in §7.

7. Potential Applications and Limitations of TLGRF

This section explores the potential for expanding TLGRF to encompass learning tasks other than small area estimations in instantaneous exponential growth rates and some possible limitations.

A natural way to expand the use of TLGRF is by adapting it to estimate dose-response models with subpopulation heterogeneity, i.e.,

$$\ln(\mathbf{I}_{s,c}) = \alpha(\mathbf{X}_{s,c}) + r(\mathbf{X}_{s,c})\mathbf{s} + \varepsilon_{s,c}.$$

Here, the independent variable \mathbf{s} represents the exposure intensity (or dosage) of a toxic substance, such as aflatoxin; the dependent variable $\ln(\mathbf{I}_{s,c})$ measures the negative health

effects (or response) of population c after being exposed to the substance, such as the log number of observed cancer cases in that population (World Health Organization 2020). In literature, it is widely accepted that the relationship between \mathbf{s} and $\ln(\mathbf{I}_{\mathbf{s},c})$ can be described by locally exponential models, which means that for any $t \in \mathbb{Z}^+$, the equation

$$\frac{\partial \mathbb{E}[\ln(\mathbf{I}_{\mathbf{s},c}) | \mathbf{s} = t, \mathbf{X}_{\mathbf{s},c}]}{\partial t} = r(\mathbf{X}_{\mathbf{s},c}) \quad (27)$$

holds (Slob and Setzer 2014). Nevertheless, the task of selecting the appropriate dose-response functional forms remains a challenge and often requires strong assumptions. A prevalent strategy, as recommended by Slob (2002), involves utilizing likelihood ratio tests to choose from a range of locally exponential models. This approach faces two main challenges. Firstly, there is a risk of model misspecification as the class of locally exponential models satisfying (27) may never be fully exhausted. Secondly, when a subpopulation c has limited observations or variations in exposure intensity, it may not be possible to estimate the subpopulation model accurately. In contrast, TLGRF avoids these problems by directly estimating the instantaneous exponential growth rates $r(\mathbf{X}_{\mathbf{s},c})$, without requiring global functional form assumptions. Additionally, by utilizing transfer learning across subpopulation data, TLGRF can obtain more precise estimates of subpopulation models, even with limited subpopulation data. Thus, TLGRF represents a promising avenue for overcoming the challenges associated with estimating dose-response models.

Nevertheless, TLGRF’s transfer learning capabilities depend on having access to panel data whose features vary in both temporal and spatial dimensions. On one hand, when restricted to data with features only varying across space, TLGRF essentially reduces to classical GRF. In this case, as explained in §6.1, the TLGRF method would inadvertently adopt the OLS weights, resulting in failure in transfer learning across time. On the other hand, when restricted to single-county data with features only varying across time, TLGRF also exhibits limited capabilities in transfer learning. To illustrate this, we experimented with TLGRF by only pooling data across time and referred to this estimator as “TLGRF Time Only”. As shown in Appendix F.5, the TLGRF Time Only method has significantly poorer performance in terms of RMSEs and MAEs compared to TLGRF. The drop in performance can be attributed to the inadequate amount of proxy data that is relevant to the target data. Proxy data that goes too far back in time is unlikely to help estimate the recent

growth rates. Without relevant proxy data, TLGRF `Time Only` cannot perform proper splitting to conduct transfer learning. For a more thorough comparison and analysis of the splitting decisions made by TLGRF and TLGRF `Time Only`, please refer to Appendix G.2. In summary, the effectiveness of TLGRF is intricately tied to the presence of data variation in both spatial and temporal dimensions, a constraint that may limit its applicability in certain contexts such as cross-sectional or time series analysis.

8. Case Study: Allocating Resources for COVID-19 Outbreak Investigations in Colorado

This section presents a case study demonstrating how TLGRF can assist policymakers in their outbreak responses. Specifically, we chose Colorado for this case study because Colorado has an excellent track record of outbreak investigation reporting (c.f. [Colorado Department of Health & Environment 2022b](#)), allowing for an extensive evaluation of our methodology. In this case study, we compare the outbreak investigation decisions made by the Colorado Department of Public Health and Environment (CDPHE) with those recommended by TLGRF. As a natural extension of this case study, we consider an alternative use case of TLGRF in Appendix G.3.3. Through these analyses, we intend to demonstrate how TLGRF can help quantify and operationalize some of CDPHE’s investigation priorities.

8.1. Analyzing CDPHE’s Investigation Decisions

We begin by illustrating the outbreak investigation process of CDPHE. By law, “all suspected outbreaks must be reported to Public Health (CDPHE) as soon as possible” in Colorado ([El Paso County Public Health 2020](#)). Once CDPHE receives the reports, they must determine which outbreaks to investigate. In general, CDPHE would prioritize their investigations for outbreaks with “concerning characteristics” such as “a high attack rate, the introduction of a new variant of concern, higher than expected severity among cases” ([Colorado Department of Health & Environment 2023](#)). Additionally, CDPHE tends to prioritize outbreak investigations for at-risk populations, such as those in healthcare and correctional settings ([Colorado Department of Health & Environment 2021](#)).

To analyze CDPHE’s investigation decisions, we first summarize its investigation record (c.f. [Colorado Department of Health & Environment 2022b](#)) in Figure 7, which indicates the start and end dates of each outbreak investigation conducted. For our study purposes, we are interested in the days when an investigation starts in a county, marked by a transition

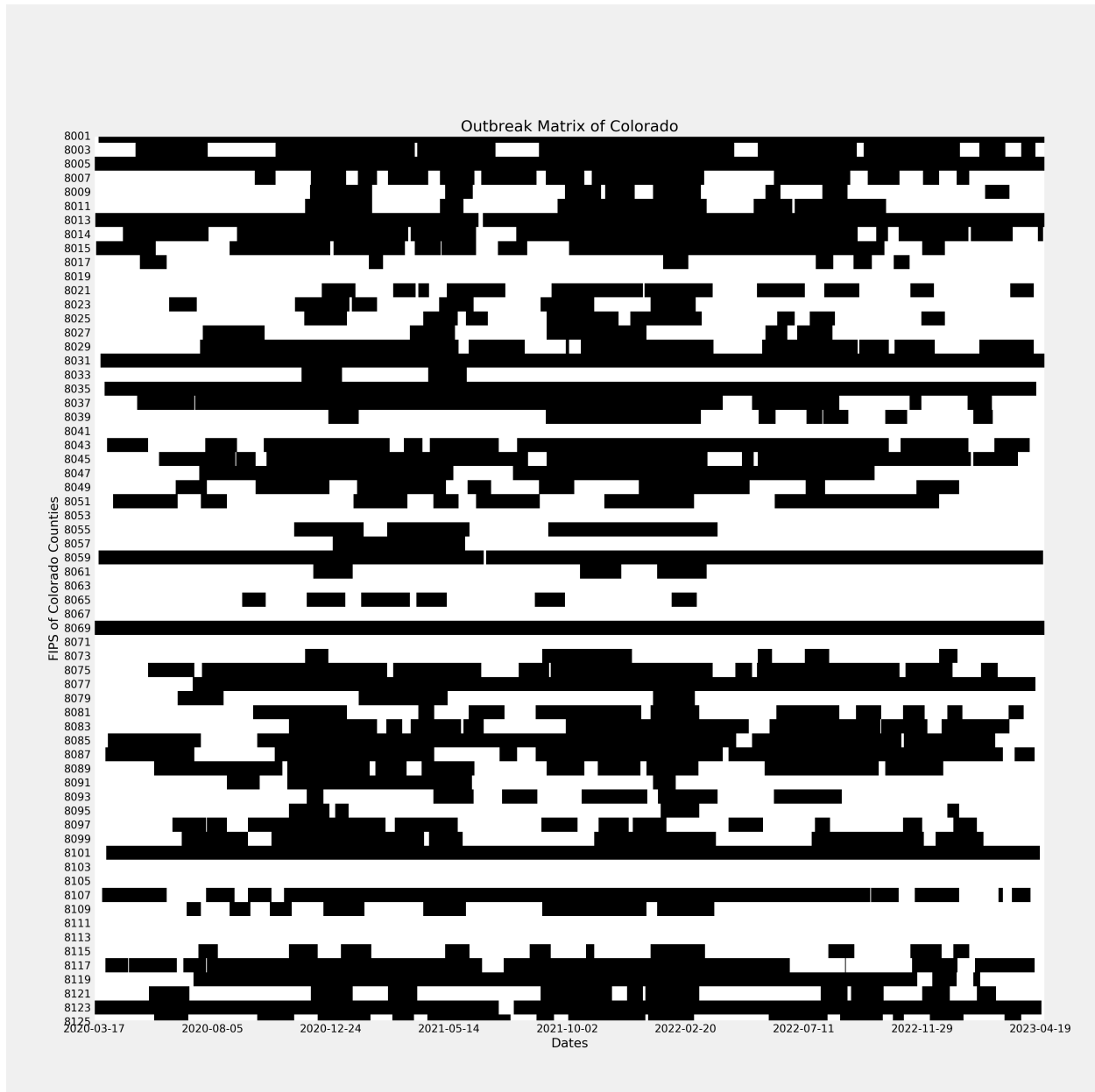


Figure 7 Outbreak Matrix of Colorado Counties, where the rows are each county (indicated by its FIPS code) and each column is a point in time. Black indicates that the county is under investigation of a suspected outbreak and white otherwise.

from white to black in Figure 7. We refer to these days as *decision points*. As demonstrated in Appendix G.3.1, out of the 1,020 days in our updated study period (from 2020-03-17 to 2022-12-31), only 159 days are decision points when CDPHE initiated new investigations. Additionally, out of these 159 decision points, CDPHE initiated only one investigation 86% (137/159) of the time.

The observed sparse pattern in CDPHE’s investigation frequency suggests a potential investigation resource constraint. In fact, as part of the procedure for investigating new outbreaks, a rapid response team often needs to be dispatched by CDPHE to conduct on-site testing (Metz et al. 2022). However, the number of rapid response teams contracted by CDPHE is limited and thus cannot be dispatched on a daily basis (Colorado Department of Health & Environment 2022a). In other words, an investigation decision can be made only on specific days when relevant resources are available.

It is thus reasonable to model CDPHE’s outbreak investigation decisions under a resource allocation framework. Specifically, given its investigation priority and resource constraints, one can evaluate whether CDPHE’s investigation decisions were justifiable in a data-driven way. If they are not, it may be possible to improve these decisions by prioritizing another county with the help of TLGRF. In the following section, we explore these pertinent questions and demonstrate how TLGRF can add value in this context.

8.2. Operationalizing CDPHE’s Investigation Priorities

This section demonstrates how TLGRF can help CDPHE to operationalize one of its main investigation priorities, i.e., outbreaks with “a high attack rate”. Specifically, we will examine whether the counties that CDPHE chose to investigate actually had a higher increase in incident cases compared to other counties in the following week. Should this not be the case, we will proceed to evaluate the effectiveness of TLGRF in accurately predicting the counties with higher attack rates for the upcoming week. Such prediction could provide valuable insight to CDPHE in terms of allocating their resources more efficiently for investigation purposes. Lastly, we also discuss the potential impact of TLGRF’s investigation recommendations on CDPHE’s other investigation priorities.

Formally, we formulate CDPHE’s investigation resource allocation as a binary classification problem. Specifically, a True Positive (TP) result means that the investigated county did indeed have the most serious outbreak. In contrast, a False Positive (FP) result means that the investigated county was not the one with the most serious outbreak. That is, there was at least another county with a similar profile of at-risk populations but a greater increase in incident cases in the following week but was not chosen by the CDPHE for investigation. For the negative predictions, a False Negative (FN) result means that the county which was not investigated turned out to be the one with the most serious outbreak, and a True Negative (TN) result means that the non-investigated counties were not among

those with the greatest increase in incident cases in the following week. On times when more than one county was investigated, the corresponding overlap between the ground truth and decisions are categorized into the various TP, FP, TN, FN as above.

		Most Serious Outbreak?		Most Serious Outbreak?	
		Yes	No	Yes	No
Investigated?	Yes	TP 33	FP 149	TP 107	FP 75
	No	FN 149	TN 1956	FN 75	TN 2030

Table 9 Comparison of CDPHE’s decisions (left) vs TLGRF’s recommendations (right) as confusion matrices.

The evaluation results of CDPHE’s decisions are summarized by the left confusion matrix of Table 9. Specifically, out of 182 counties CDPHE chose to investigate, only 33 of them turned out to experience the most serious outbreaks in the following week, corresponding to a positive predictive value (PPV) of 18.1%. In other words, at approximately four out of five investigation attempts, CDPHE did not allocate its scarce resources optimally to investigate the most serious outbreaks.

Next, we demonstrate how TLGRF can improve CDPHE’s investigation decisions. Specifically, at each decision point, we first use TLGRF to estimate the rate of change in incident cases, i.e.,

$$\frac{dI_{t,c}}{dt} = \hat{r}_{t,c}^{TLGRF} I_{t,c}, \quad (28)$$

for all counties currently not under investigation. This rate (28) is determined by multiplying TLGRF’s estimated instantaneous exponential growth rate ($\hat{r}_{t,c}^{TLGRF}$) by the current reported incident case numbers ($I_{t,c}$). Subsequently, we choose the county to investigate based on CDPHE’s investigation capacity at this decision point. For example, if CDPHE has initiated one investigation at this decision point, we recommend investigating the county with the highest estimated rate (28). Similarly, on decision points when CDPHE investigates two or three counties, TLGRF’s recommendation would be to investigate the

counties with the top two or three highest estimated rates (28). As such, TLGRF recommends the same number of investigations that CDPHE actually conducts at each decision point. Therefore, TLGRF’s recommendations are comparable to CDPHE’s decisions.

As shown in the right confusion matrix of Table 9, CDPHE’s decisions can be substantially improved upon with the help of TLGRF. Specifically, if CDPHE chose to investigate the county recommended by TLGRF, its detection rate could be improved by 224% (from 33 to 107 out of 182). We remark that while our estimation of FP (also TP) rate for the CDPHE is exact, the estimation for the CDPHE’s FN rate is a lower bound. This is because at each decision point, if CDPHE chooses to investigate a county that does not have the highest growth rate in the following week (i.e., a FP case), it implies that CDPHE fails to investigate at least one more county with a higher growth rate in the following week (i.e., at least one or more FN cases). In other words, we assume that for each FP case, there is exactly one FN case while in reality we only know that there is *at least* one FN case. Hence, our estimation for CDPHE’s FN rate is likely an underestimation and TN rate is an overestimation. Yet, even with this conservative approach, we observe that in addition to improving the number of true positives by 224%, the TLGRF improves the true negative rate by 3.51% (from 1956 to 2030 out of 2105).

We further observe that, in addition to improving the overall prediction accuracy, TLGRF also improves the prediction time of the most serious outbreaks. For example, on July 5th 2020, CDPHE recommended an investigation of Jefferson County, which uncovered an outbreak at a Chick-fil-A (an American fast food chain) with 2 confirmed cases and no deaths. In contrast TLGRF recommended an investigation of Mesa County, whereas CDPHE did choose to investigate Mesa one week later. This county-level outbreak was later linked to a local-level outbreak in the St Mary’s Medical Center and the Grandview Care Lodge Assisted Living facility (Zorn 2020) with 13 confirmed cases and 2 deaths. One week later on July 13th 2020, CDPHE did decide to investigate Mesa County, while TLGRF continued to recommend Mesa County’s investigation.

Lastly, we discuss the impact of TLGRF’s recommendations on CDPHE’s other investigation priorities. Table 10 shows that counties recommended by TLGRF are similar to those investigated by CDPHE in terms of demographic characteristics such as nursing homes, correctional facilities, and total populations. Therefore, TLGRF’s recommendations are consistent with CDPHE’s investigation prioritization, which focuses resources on outbreaks

Column	Total Population	Nursing Home Beds	Inmates
CDPHE mean	36322.53	103.29	379.17
TLGRF mean	45167.48	72.37	182.37
t-statistic	-1.02	1.01	1.60
Standard Error	8684.54	30.50	122.73
95% CI	(-25866.66, 8176.76)	(-28.86, 90.69)	(-43.74, 437.34)
p-value	0.31	0.31	0.11

Table 10 To compare the at-risk population profile of counties selected for investigation by CDPHE and TLGRF, this table presents the means of nursing homes, prisons and county population of their investigation choices, respectively. Results for two sample *t*-tests between these means are also presented, where a large *p*-value (typically greater than 0.05) means that CDPHE and TLGRF’s investigation choices are not statistically different in terms of the at-risk population profile. $n = 182$ for both CDPHE and TLGRF

among at-risk populations (c.f. [Colorado Department of Health & Environment 2022b](#)). A more detailed comparison of the decisions made by CDPHE and TLGRF can be found in Appendix [G.3.2](#).

9. A Decision Support Tool for Implementation: COVID-19 Outbreak Detection Tool

We expanded on our research by developing a public decision support tool based on the TLGRF algorithm presented in this study. The “COVID-19 Outbreak Detection Tool” offers an interactive choropleth displaying county-specific doubling times, showcasing the duration required for daily incident COVID-19 case numbers in a county to double. Additionally, a user-friendly data explorer is available for users to access, examine, and download the data, estimates, and predictions utilized in our study. Released on September 15, 2020, the web platform (www.covid19sim.org) experienced consistent traffic from all 50 states in the US. Notably, public health officials from various U.S. states also utilized this platform.

A detailed description of the tool’s functionalities and its impact, along with specific usage details, is provided in Appendix [H](#). This tool served as an essential resource, attracting significant user engagement, and was instrumental in assisting public health authorities in their decision-making processes during the ongoing pandemic.

10. Conclusion

In this work, we developed a transfer learning algorithm, i.e., **TLGRF**, which obtains reliable small area estimates for COVID-19 growth rates. By pooling proxy data across time and space, **TLGRF** addresses a key challenge in small area case growth estimates, i.e., choosing the fitting window to adequately balance the speed-accuracy tradeoff in estimation. This algorithm can be readily extended to other estimation problems in epidemiology where fitting window size choices play an important role, e.g., estimating the county-level instantaneous reproduction number (c.f. [Fraser 2007](#), [Cori et al. 2013](#)), as well as the estimation problem of dose-response models with subpopulation heterogeneity discussed in §7.

We also showcased an application of **TLGRF** in our Colorado case study and demonstrated that with more reliable estimates of small area case growth rates, public health officials could better allocate their limited resources in outbreak investigations. Particularly, we demonstrate that **TLGRF** can serve to substantially improve detection rates of the most serious outbreaks within a much earlier time frame.

In our ongoing commitment to keep the public informed and assist timely decision making by health and governing authorities, we have developed an online, interactive decision support tool to disseminate our findings. This tool has provided the doubling time of COVID-19 incident case numbers in each county since September 2020 and has attracted significant public attention. Our outbreak detection tools and resulting findings have been used by multiple states to track the spread of COVID-19 in different jurisdictions by policy-makers.

References

- Anderson R, Donnelly C, Hollingsworth D, Keeling M, Vegvari C, Baggaley R, Maddren R (2020) Reproduction number (R) and growth rate (r) of the COVID-19 epidemic in the UK: methods of estimation, data sources, causes of heterogeneity, and use as a guide in policy formulation. *The Royal Society* 2020.
- Angrist JD, Imbens GW (1995) Two-stage least squares estimation of average causal effects in models with variable treatment intensity. *Journal of the American Statistical Association* 90(430):431–442.
- Arthur D, Vassilvitskii S (2007) k-means++: the advantages of careful seeding. *SODA '07: Proceedings of the Eighteenth Annual ACM-SIAM Symposium on Discrete Algorithms*, 1027–1035 (Philadelphia, PA, USA: Society for Industrial and Applied Mathematics), ISBN 978-0-898716-24-5.
- Athey S, Imbens G (2016) Recursive partitioning for heterogeneous causal effects. *Proceedings of the National Academy of Sciences* 113(27):7353–7360.

- Athey S, Tibshirani J, Wager S, et al. (2019) Generalized random forests. *The Annals of Statistics* 47(2):1148–1178.
- Awan TM, Aslam F (2020) Prediction of Daily COVID-19 Cases in European Countries Using Automatic ARIMA Model. *Journal of Public Health Research* 9(3).
- Bai M, Cui Y, Kong G, Zhang AZ (2021) No panic in pandemic: The impact of individual choice on public health policy and vaccine priority. *University of Connecticut School of Business Research Paper* (21-02).
- Bastani H (2021) Predicting with proxies: Transfer learning in high dimension. *Management Science* 67(5):2964–2984.
- Bastani H, Drakopoulos K, Gupta V, Vlachogiannis I, Hadjicristodoulou C, Lagiou P, Magiorkinis G, Paraskevis D, Tsiodras S (2021) Efficient and targeted COVID-19 border testing via reinforcement learning. *Nature* 599(7883):108–113.
- Ben Phillips (2020) Coronavirus 10-day forecast. Available at <https://covid19forecast.science.unimelb.edu.au/> (Accessed September, 18, 2020).
- Bergman A, Sella Y, Agre P, Casadevall A (2020) Oscillations in US COVID-19 incidence and mortality data reflect diagnostic and reporting factors. *Msystems* 5(4):e00544–20.
- Bertozzi AL, Franco E, Mohler G, Short MB, Sledge D (2020) The challenges of modeling and forecasting the spread of COVID-19. *Proceedings of the National Academy of Sciences* 117(29):16732–16738.
- Bertsimas D, Boussioux L, Cory-Wright R, Delarue A, Digalakis V, Jacquillat A, Kitane DL, Lukin G, Li M, Mingardi L, et al. (2021) From predictions to prescriptions: A data-driven response to COVID-19. *Health Care Management Science* 1–20.
- Betcheva L, Erhun F, Feylessoufi A, Gonçalves P, Jiang H, Kattuman PA, Pape T, Pari A, Scholtes S, Tyrrell C (2021) Rapid COVID-19 Modeling Support for Regional Health Systems in England. *SSRN Working Paper* .
- Birge JR, Candogan O, Feng Y (2022) Controlling epidemic spread: Reducing economic losses with targeted closures. *Management Science* .
- Braca P, Gaglione D, Marano S, Millefiori LM, Willett P, Pattipati KR (2021) Quickest detection of COVID-19 pandemic onset. *IEEE Signal Processing Letters* 28:683–687.
- Camelo S, Ciocan DF, Iancu DA, Warnes XS, Zoumpoulis SI (2021) Quantifying the benefits of targeting for pandemic response. *medRxiv* 2021–03.
- Centers for Disease Control and Prevention (2018) Centers for Disease Control and Prevention Social Vulnerability Index 2018 Database. Available at https://www.atsdr.cdc.gov/placeandhealth/svi/data_documentation_download.html.
- Centers for Disease Control and Prevention (2021a) CDC - variant classifications. <https://www.cdc.gov/coronavirus/2019-ncov/variants/variant-classifications.html>, accessed 2023-01-01.

-
- Centers for Disease Control and Prevention (2021b) Cdc covid data tracker. Available at <https://data.cdc.gov/Laboratory-Surveillance/SARS-CoV-2-Variant-Proportions/jr58-6ysp/> (Accessed February 27, 2023).
- Chen X, Li M, Simchi-Levi D, Zhao T (2020) Allocation of COVID-19 vaccines under limited supply. *Available at SSRN 3678986* .
- Chen Z, Kong G (2023) Hospital admission, facility-based isolation, and social distancing: An SEIR model with constrained medical resources. *Production and Operations Management* 32(5):1397–1414.
- Chowell G, Fenimore PW, Castillo-Garsow MA, Castillo-Chavez C (2003) SARS outbreaks in Ontario, Hong Kong and Singapore: the role of diagnosis and isolation as a control mechanism. *Journal of Theoretical Biology* 224(1):1–8.
- Chowell G, Nishiura H, Bettencourt LM (2007) Comparative estimation of the reproduction number for pandemic influenza from daily case notification data. *Journal of the Royal Society Interface* 4(12):155–166.
- Colorado Department of Health & Environment (2021) COVID-19 Outbreak Data. <https://web.archive.org/web/20210527003313/https://covid19.colorado.gov/covid19-outbreak-data>, accessed: October 27, 2023.
- Colorado Department of Health & Environment (2022a) COVID Rapid Response Testing in Schools. <https://www.bidnet.com/closed-government-contracts/covid-rapid-response-testing-in-schools?itemId=808895051>.
- Colorado Department of Health & Environment (2022b) Outbreak data. Available at <https://covid19.colorado.gov/covid19-outbreak-data> (Accessed February 28, 2022).
- Colorado Department of Health & Environment (2023) Outbreak report form. <https://docs.google.com/document/d/1e-IWLtzJNCgI2gzPONGvEASGgse85WuBmcToc9ev-74/edit>.
- Cori A, Ferguson NM, Fraser C, Cauchemez S (2013) A new framework and software to estimate time-varying reproduction numbers during epidemics. *American Journal of Epidemiology* 178(9):1505–1512.
- D’Amour A, Ding P, Feller A, Lei L, Sekhon J (2021) Overlap in observational studies with high-dimensional covariates. *Journal of Econometrics* 221(2):644–654.
- El Paso County Public Health (2020) Covid-19 workplace outbreak guidance. Available at <https://www.elpasocountyhealth.org/sites/default/files/2020-06/COVID-19%20Workplace%20Outbreak%20Guidance%20from%20EPC%20Public%20Health.pdf> (Accessed November, 17, 2023).
- Farias VF, Li AA (2019) Learning preferences with side information. *Management Science* 65(7):3131–3149.
- Farrington P, Andrews N (2004) Outbreak detection: Application to infectious disease surveillance. Brookmeyer R, et al., eds., *Monitoring the Health of Populations: Statistical Principles and Methods for Public Health Surveillance*, chapter 8, 203–231 (Oxford: Oxford University Press).

- Fraser C (2007) Estimating individual and household reproduction numbers in an emerging epidemic. *PLoS one* 2(8):e758.
- Goldberg EE, Lin Q, Romero-Severson EO, Ke R (2023) Swift and extensive Omicron outbreak in China after sudden exit from Zero-COVID policy. *Nature Communications* 14:3888, URL <http://dx.doi.org/https://doi.org/10.1038/s41467-023-39638-4>.
- Hamilton JD (2020) *Time Series Analysis* (Princeton university press).
- Hohl A, Delmelle EM, Desjardins MR, Lan Y (2020) Daily surveillance of COVID-19 using the prospective space-time scan statistic in the United States. *Spatial and Spatio-temporal Epidemiology* 34:100354.
- Holmdahl I, Buckee C (2020) Wrong but useful—what COVID-19 epidemiologic models can and cannot tell us. *New England Journal of Medicine* 383(4):303–305.
- Julia R (2020) COVID-19 U.S. State Policy (CUSP) Database. URL <https://www.evidenceforaction.org/{COVID-19}-us-state-policy-cusp-database>.
- Kaplan EH (2020) Om forum—COVID-19 scratch models to support local decisions. *Manufacturing & Service Operations Management* 22(4):645–655.
- Karadayi Y, Aydin MN, Ögrenci AS (2020) Unsupervised anomaly detection in multivariate spatio-temporal data using deep learning: Early detection of COVID-19 outbreak in Italy. *IEEE Access* 8:164155–164177.
- Kittitas County (2020) COVID-19 Incident Rate Explained. Available at <https://nkctribune.com/{COVID-19}-incident-rate-explained-2/> (Accessed: 2021-08-02).
- Li ML, Bouardi HT, Lami OS, Trikalinos TA, Trichakis N, Bertsimas D (2023) Forecasting COVID-19 and analyzing the effect of government interventions. *Operations Research* 71(1):184–201.
- Lipsitch M, Cohen T, Cooper B, Robins JM, Ma S, James L, Gopalakrishna G, Chew SK, Tan CC, Samore MH, et al. (2003) Transmission dynamics and control of severe acute respiratory syndrome. *Science* 300(5627):1966–1970.
- Liu J, Xia S (2020) Paradigms in epidemiology. *Computational Epidemiology*, 1–13 (Springer).
- Ma J (2020) Estimating epidemic exponential growth rate and basic reproduction number. *Infectious Disease Modelling* 5:129–141.
- Ma J, Dushoff J, Bolker BM, Earn DJ (2014) Estimating initial epidemic growth rates. *Bulletin of Mathematical Biology* 76(1):245–260.
- Ma Q, Zheng J, Li S, Cottrell GW (2019) Learning representations for time series clustering. *Advances In Neural Information Processing Systems* 32.
- McNutt LA, Krug A (2016) Incidence. Available at <https://www.britannica.com/science/incidence-epidemiology> (Accessed: 2021-08-02).

-
- Mehrotra S, Rahimian H, Barah M, Luo F, Schantz K (2020) A model of supply-chain decisions for resource sharing with an application to ventilator allocation to combat COVID-19. *Naval Research Logistics (NRL)* 67(5):303–320.
- Mehta M, Julaiti J, Griffin P, Kumara S, et al. (2020) Early stage machine learning–based prediction of US county vulnerability to the COVID-19 pandemic: machine learning approach. *JMIR Public Health and Surveillance* 6(3):e19446.
- Metz AR, Bauer M, Epperly C, Stringer G, Marshall KE, Webb LM, Hetherington-Rauth M, Matzinger SR, Totten SE, Travanty EA, et al. (2022) Investigation of COVID-19 Outbreak among Wildland Firefighters during Wildfire Response, Colorado, USA, 2020. *Emerging Infectious Diseases* 28(8):1551.
- Nakıp M, Çopur O, Güzeliş C (2020) Curse of small sample size in forecasting of the active cases in COVID-19 outbreak. *arXiv preprint arXiv:2011.03628* .
- Palmer AZ, Zabinsky ZB, Liu S (2020) Optimal control of COVID-19 infection rate considering social costs. *arXiv preprint arXiv:2007.13811* .
- Pan SJ, Yang Q (2009) A survey on transfer learning. *IEEE Transactions on Knowledge and Data Engineering* 22(10):1345–1359.
- Pedregosa F, Varoquaux G, Gramfort A, Michel V, Thirion B, Grisel O, Blondel M, Prettenhofer P, Weiss R, Dubourg V, Vanderplas J, Passos A, Cournapeau D, Brucher M, Perrot M, Duchesnay E (2011) Scikit-learn: Machine learning in Python. *Journal of Machine Learning Research* 12:2825–2830.
- Ray EL, Wattanachit N, Niemi J, Kanji AH, House K, Cramer EY, Bracher J, Zheng A, Yamana TK, Xiong X, et al. (2020) Ensemble forecasts of coronavirus disease 2019 (COVID-19) in the US. *medRxiv* .
- Rodriguez A, Tabassum A, Cui J, Xie J, Ho J, Agarwal P, Adhikari B, Prakash BA (2020) Deepcovid: An operational deep learning-driven framework for explainable real-time COVID-19 forecasting. *medRxiv* .
- Ruiz-Correa S, López-Revilla R, Díaz-Barriga F, Marmolejo-Cossío F, del Carmen Robledo-Valero V, Hernández-Huérffano EE, Álvarez-Rivera L, Rangel-Martínez ML, Lutzow-Steiner MÁ, Ortiz-Vázquez LA, et al. (2021) Health Sentinel: a mobile crowdsourcing platform for self-reported surveys provides early detection of COVID-19 clusters in San Luis Potosí, Mexico. *International Journal of Medical Informatics* 104508.
- Shi P, Helm J, Chen C, Lim J, Parker RP, Tinsley T, Cecil J (2021) Operations (management) warp speed: Parsimonious design for rapid deployment of hospital prediction and decision support framework during a pandemic. *Available at SSRN 3815418* .
- Singh V, Poonia RC, Kumar S, Dass P, Agarwal P, Bhatnagar V, Raja L (2020) Prediction of COVID-19 corona virus pandemic based on time series data using support vector machine. *Journal of Discrete Mathematical Sciences and Cryptography* 23(8):1583–1597.
- Slob W (2002) Dose-response modeling of continuous endpoints. *Toxicological Sciences* 66(2):298–312.

- Slob W, Setzer RW (2014) Shape and steepness of toxicological dose–response relationships of continuous endpoints. *Critical Reviews in Toxicology* 44(3):270–297.
- Soldi G, Forti N, Gaglione D, Braca P, Millefiori LM, Marano S, Willett P, Pattipati K (2021) Quickest detection and forecast of pandemic outbreaks: Analysis of COVID-19 waves. *arXiv preprint arXiv:2101.04620* .
- Sommer L (2020) Are We Flattening The Curve? States Keep Watch On Coronavirus ‘Doubling Times’. Available at <https://www.npr.org/sections/health-shots/2020/04/10/829167659/are-we-flattening-the-curve-states-keep-watch-on-coronavirus-doubling-times> (Accessed: 2021-07-11).
- Sugiyama M, Suzuki T, Nakajima S, Kashima H, Von Bünau P, Kawanabe M (2008) Direct importance estimation for covariate shift adaptation. *Annals of the Institute of Statistical Mathematics* 60:699–746.
- Tandon H, Ranjan P, Chakraborty T, Suhag V (2020) Coronavirus (COVID-19): ARIMA based time-series analysis to forecast near future. *arXiv preprint arXiv:2004.07859* .
- The Atlantic (2018) The COVID Tracking Project. Available at <https://covidtracking.com/>.
- The Mayo Clinic (2021) Hot spots in the United States. Available at <https://www.nytimes.com/interactive/2021/us/covid-cases.html> (Accessed 2021-07-18).
- The New York Times (2020) Coronavirus (Covid-19) Data in the United States. Available at <https://github.com/nytimes/{COVID-19}-data> (Accessed 2020-09-07).
- The New York Times (2021) Coronavirus in the U.S.: Latest Map and Case Count. Available at <https://www.nytimes.com/interactive/2021/us/covid-cases.html> (Accessed 2021-07-18).
- Tibshirani J, Athey S, Sverdrup E, Wager S (2023) Causal forest — generalized random forests. https://grf-labs.github.io/grf/reference/causal_forest.html (Accessed 2023-06-30).
- United States Census Bureau (2019) 2019 US Census Gazetteer Files. Available at <https://www.census.gov/geographies/reference-files/time-series/geo/gazetteer-files.html>.
- Weisstein EW (2023) Positive integer. <https://mathworld.wolfram.com/PositiveInteger.html>, from MathWorld—A Wolfram Web Resource.
- Wieczorek M, Siłka J, Woźniak M (2020) Neural network powered COVID-19 spread forecasting model. *Chaos, Solitons & Fractals* 140:110203.
- World Health Organization (2020) *Dose–response assessment and derivation of health-based guidance values*, chapter 5 (World Health Organization), URL <https://cdn.who.int/media/docs/default-source/food-safety/publications/chapter5-dose-response.pdf?sf>.
- Wynants L, Van Calster B, Collins GS, Riley RD, Heinze G, Schuit E, Bonten MM, Dahly DL, Damen JA, Debray TP, et al. (2020) Prediction models for diagnosis and prognosis of COVID-19: systematic review and critical appraisal. *The BMJ* 369.

- Zhang LM (2021) Singapore extends stay-home notice to 21 days for travellers from higher-risk countries or regions. *The Straits Times* Available at: <https://www.straitstimes.com/singapore/singapore-extends-stay-home-notice-to-21-days-for-travellers-from-higher-risk-places> (Accessed November 29, 2023).
- Zhang T, Lin G (2021) Generalized k-means in GLMs with applications to the outbreak of COVID-19 in the United States. *Computational Statistics & Data Analysis* 159:107217.
- Zhuang F, Qi Z, Duan K, Xi D, Zhu Y, Zhu H, Xiong H, He Q (2020) A comprehensive survey on transfer learning. *Proceedings of the IEEE* 109(1):43–76.
- Zorn A (2020) Several St. Mary’s staff members reportedly test positive for COVID-19. *The Daily Sentinel* URL https://www.gjsentinel.com/news/western_colorado/several-st-marys-staff-members-reportedly-test-positive-for-{COVID-19}/article_653be820-d2ab-11ea-982b-9b4ac9686d01.html.

Appendix

Appendix A: Implementation Details and Pseudocode for Estimation Algorithms

A.1. TLGRF Implementation Details and Pseudocode

In this subsection, we provide the implementation details of TLGRF, and highlight its difference from the classical GRF method by [Athey et al. \(2019\)](#). To this end, we first summarize the classical GRF method. Second, we present our TLGRF method as a variant of the classical GRF method. Third, we provide a concrete example to illustrate the difference between TLGRF and classical GRF.

Dependent Variable	Independent Variable	Feature
$\ln(I_{1,1})$	1	$x_{1,1}$
$\ln(I_{2,1})$	2	$x_{2,1}$
$\ln(I_{3,1})$	3	$x_{3,1}$
$\ln(I_{4,1})$	4	$x_{4,1}$
\vdots	\vdots	\vdots

Table 11 GRF Data Structure

First, the classical GRF method is designed to estimate the conditional average partial effect (CAPE) (c.f. [Tibshirani et al. 2023](#)):

$$\frac{\text{Cov}[\ln(\mathbf{I}_{s,c}), \mathbf{s} | \mathbf{X}]}{\text{Var}[\mathbf{s} | \mathbf{X}]}, \quad (29)$$

where

- \mathbf{X} is a random vector of features taking values in \mathbb{R}^n ;
- \mathbf{s} is a random independent variable taking values in \mathbb{R} ;
- $\mathbf{I}_{s,c}$ is a random dependent variable taking values in \mathbb{R} .

Table 11 represents a typical input to the classical GRF algorithm. When the CAPE is properly identified, the classical GRF algorithm constructs a measure $\{\alpha_{c'}(X)\}_{c' \in C}$. This measure shows how similar the proxy feature \mathbf{X}' is to the target features \mathbf{X} : $\forall c' \in C$,

$$\alpha_{c'}(X) = \mathbb{P}[X' \in \bigcup_{b \in B} L_b(X)]. \quad (30)$$

Here, b and B represent the decision tree and random forests of GRF, respectively; $L_b(X)$ is the leaf where X lands at the end of the splitting process of the tree b . The similarity measure (30) is thus the probability that \mathbf{X}' ends up at the same leaf as \mathbf{X} during in random forests B . As such, the classical GRF estimator is obtained by weighing CAPEs with the GRF similarity measure:

$$r^{GRF}(\mathbf{X}) = \sum_{c' \in C} \alpha_{c'}(\mathbf{X}) \frac{\text{Cov}[\ln(\mathbf{I}_{s,c'}), \mathbf{s} | \mathbf{X}']}{\text{Var}[\mathbf{s} | \mathbf{X}']}.$$

Dependent Variable	Independent Variable	Feature
0	0	$x_{2,1}$
$\ln(I_{2,1}) - \ln(I_{1,1})$	1	$x_{2,1}$
0	0	$x_{4,1}$
$\ln(I_{4,1}) - \ln(I_{3,1})$	1	$x_{4,1}$
\vdots	\vdots	\vdots

Table 12 TLGRF Data Structure

Second, we build our TLGRF method upon the classical GRF method. Specifically, instead of feeding data in its original format (e.g., Table 11) to the GRF algorithm, TLGRF conducts two steps of data pre-processing before feeding them to the GRF algorithm. As detailed in §4, these two steps involve

1. Partitioning the dataset into two-day “data blocks”:

$$\{\ln(\mathbf{I}_{t',c'}), \ln(\mathbf{I}_{t'-1,c'}), \mathbf{X}_{t',c'}\}_{t' \in [t], c' \in C} \text{ where } [t] := \{t' \in \{1, \dots, t\} | t' \equiv t' \pmod{2}\},$$

and

2. Normalizing these two-day “data blocks”: $\forall t' \in [t], \forall t^- \in \{t' - 1, t'\}$ and $\forall c' \in C$,
 - Dependent Variable: $\ln(\mathbf{I}_{t^-,c'}) - \ln(\mathbf{I}_{t'-1,c'})$,
 - Independent Variable: $t^- - (t' - 1)$,
 - Feature: $\mathbf{X}_{t',c'}$.

The pseudocode for this pre-processing procedure is displayed in Algorithm 1. Lastly, the pre-processed data, in the format of Table 12, is fed into the GRF algorithm to generate the GRF weights: $\forall t' \in [t]$ and $\forall c' \in C$,

$$\gamma_{t',c'}(\mathbf{X}_{t,c}) := \frac{1}{|B|} \sum_{b=1}^{|B|} \frac{\mathbb{1}(\{\mathbf{X}_{t',c'} \in L_b(\mathbf{X}_{t,c})\})}{|L_b(\mathbf{X}_{t,c})|},$$

and thus the TLGRF estimator:

$$r^{TLGRF}(\mathbf{X}_{t,c}) = \sum_{t' \in [t]} \sum_{c' \in C} \gamma_{t',c'}(\mathbf{X}_{t,c}) (\ln(\mathbf{I}_{t',c'}) - \ln(\mathbf{I}_{t'-1,c'})).$$

The pseudocode for this transfer learning procedure is displayed in Algorithm 2.

Algorithm 1: Normalization and Initial Estimates

Input: $\{(I_{t',c'}, \mathbf{X}_{t',c'})\}_{t' \in \{1, \dots, t\}, c' \in C}$
Output: $\{Feature[t', c']\}_{t' \in \{1, \dots, t\}, c' \in C}$, $\{Y[t', c', 1], Y[t', c', 0]\}_{t' \in \{1, \dots, t\}, c' \in C}$

```

1 for  $c' \leftarrow 1$  to  $|C|$  do
2   for  $t' \leftarrow 1$  to  $t$  do
3     /* Normalize the incident case numbers for each block */
4      $Y[t', c', 1] \leftarrow \ln(I_{t',c'}) - \ln(I_{t'-1,c'})$ ;
5      $Y[t', c', 0] \leftarrow 0$ ;
6      $W[t', c', 1] \leftarrow 1$ ;
7      $W[t', c', 0] \leftarrow 0$ ;
8     /* Generate the initial OLS estimates for each block */
9      $Dep \leftarrow \{Y[t', c', 1], Y[t', c', 0]\}$ ;
10     $Ind \leftarrow \{W[t', c', 1], W[t', c', 0]\}$ ;
11     $\{r_{t',c'}^{ols}, \alpha_{t',c'}^{ols}\} \leftarrow OLS(Dep \sim Ind)$ ;
12    /* Append the feature data for each block */
13     $Feature[t', c'] \leftarrow \{\mathbf{X}_{t',c'}, r_{t',c'}^{ols}, \alpha_{t',c'}^{ols}, t\}$ ;
14  end
15 end
```

Algorithm 2: Transfer Learning through GRF

Input: $\{Feature[t', c']\}_{t' \in \{1, \dots, t\}, c' \in C}$, $\{Y[t', c', 1], Y[t', c', 0]\}_{t' \in \{1, \dots, t\}, c' \in C}$
Output: $\{r_{t,c'}^{GRF}\}_{c' \in C}$

```

/* Compute the congruence classes */
1  $[t] \leftarrow \{t' \in \{1, \dots, t\} | t \equiv t' \pmod{2}\}$ ;
/* Assign the feature variable */
2  $X \leftarrow \{Feature[t', c'], Feature[t', c']\}_{t' \in [t], c' \in C}$ ;
/* Assign the outcome variable */
3  $Y \leftarrow \{Y[t', c', 1], Y[t', c', 0]\}_{t' \in [t], c' \in C}$ ;
/* Assign the treatment variable */
4  $W \leftarrow \{W[t', c', 1], W[t', c', 0]\}_{t' \in [t], c' \in C}$ ;
/* Feed (X,Y,W) into the GRF algorithm and obtain final estimates */
5  $\{r_{t,c'}^{GRF}\}_{c' \in C} \leftarrow GRF(X, Y, W)$ ;
```

Algorithm 1 represents the key difference between TLGRF and the classical GRF method. Specifically, we have theoretically demonstrated in §6.1 that GRF alone cannot effectively leverage time-varying features and eliminate the OLS weights in its estimates. To emphasize the importance of Algorithm 1, we present an example that highlights how GRF and TLGRF can produce different estimates even if the same proxy data are allocated to the leaf containing the target data by both algorithms.

Let's consider a scenario with a single tree where the target data is $\{\ln(\mathbf{I}_{t,c}), t, \mathbf{X}_{t,c}\}$. Suppose that under both GRF and TLGRF, the leaf containing the target data also includes data of the same county from the past three days. In this case, the GRF estimator is

$$\begin{aligned}
r^{GRF}(\mathbf{X}_c) &= \sum_{c' \in C} \alpha_{c'}(\mathbf{X}_c) \frac{\text{Cov}[\ln(\mathbf{I}_{s,c'}), \mathbf{s} | \mathbf{X}_c]}{\text{Var}[\mathbf{s} | \mathbf{X}_c]} \\
&= \frac{\text{Cov}[\ln(\mathbf{I}_{s,c'}), \mathbf{s} | \mathbf{X}_c]}{\text{Var}[\mathbf{s} | \mathbf{X}_c]}
\end{aligned}$$

$$\begin{aligned}
&= \frac{\sum_{t^- = t-3}^t (t^- - \frac{t^- - t^- - 3}{4}) (\ln(I_{t^-,c}) - \frac{\sum_{t^- = t-3}^t \ln(I_{t^-,c})}{4})}{\sum_{t^- = t-3}^t (t^- - \frac{t^- - t^- - 3}{4})^2} \\
&= 0.3 \times [\ln(I_{t,c}) - \ln(I_{t-1,c})] + 0.4 \times [\ln(I_{t-1,c}) - \ln(I_{t-2,c})] + 0.3 \times [\ln(I_{t-2,c}) - \ln(I_{t-3,c})],
\end{aligned}$$

where the weights (0.3,0.4,0.3) corresponds to the OLS weights (7) with fitting window size $\delta = 4$. In contrast, the TLGRF estimator is

$$\begin{aligned}
r^{TLGRF}(\mathbf{X}_{t,c}) &= \sum_{t' \in [t]} \sum_{c' \in C} \gamma_{t',c'}(\mathbf{X}_{t,c}) (\ln(\mathbf{I}_{t',c'}) - \ln(\mathbf{I}_{t'-1,c'})) \\
&= \gamma_{t,c}(\mathbf{X}_{t,c}) (\ln(I_{t,c}) - \ln(I_{t-1,c})) + \gamma_{t-2,c}(\mathbf{X}_{t,c}) (\ln(I_{t-2,c}) - \ln(I_{t-3,c})) \\
&= \frac{\mathbb{1}(\{\mathbf{X}_{t,c} \in L_b(\mathbf{X}_{t,c})\})}{|L_b(\mathbf{X}_{t,c})|} (\ln(I_{t,c}) - \ln(I_{t-1,c})) + \frac{\mathbb{1}(\{\mathbf{X}_{t-2,c} \in L_b(\mathbf{X}_{t,c})\})}{|L_b(\mathbf{X}_{t,c})|} (\ln(I_{t-2,c}) - \ln(I_{t-3,c})) \\
&= 0.5 \times [\ln(I_{t+3,c}) - \ln(I_{t+2,c})] + 0.5 \times [\ln(I_{t+1,c}) - \ln(I_{t,c})],
\end{aligned}$$

where the last equality utilizes the normalized leaf node: $L_b(\mathbf{X}_{t,c}) = \{\mathbf{X}_{t,c}, \mathbf{X}_{t-2,c}\}$. To summarize, Algorithm 1 is the primary distinguishing factor between TLGRF and GRF. This algorithm enables TLGRF to achieve fully adaptive weighting and eliminate the OLS weights in the classical GRF method.

A.2. Dynamic Window Implementation Details

In this subsection, we provide the implementation details of the Dynamic Window procedures, `tcv` and `ctcv` as referenced in §5.2, and the K-Means Dynamic Window procedure as described in §5.3.

A.2.1. `tcv` Implementation Details The `tcv` estimator (19) can be directly computed from the case incidence data $\{(s, \ln(\mathbf{I}_{s,c})) : \forall s \in \{t - \delta_t + 1, \dots, t\}, c \in C\}$ for any fitting window size hyperparameter as:

$$\hat{r}_{t,c}^{ols(\delta_t)} = \frac{\sum_{s=t-\delta_t+1}^t (s - \frac{\sum_{s=t-\delta_t+1}^t s}{\delta_t}) (\ln(\mathbf{I}_{s,c}) - \frac{\sum_{s=t-\delta_t+1}^t \ln(\mathbf{I}_{s,c})}{\delta_t})}{\sum_{s=t-\delta_t+1}^t (s - \frac{\sum_{s=t-\delta_t+1}^t s}{\delta_t})^2}. \quad (31)$$

This encompasses the incidence case data of every county c from the beginning of the chosen fitting window $(t - \delta_t + 1)$ to the current time of query (t) . As described in §5.2, the key characteristic of the `tcv` estimator is that at each time point t , all the counties are constrained to use the same fitting window size hyperparameter δ_t , i.e., the entire nation shares the same fitting window hyperparameter at every time step. We will now describe the cross-validation procedure to obtain the best δ_t , and how the final test-time estimator is computed and evaluated.

Our goal at test time is to forecast the log-incident case numbers of each county $(\ln(I_{t+7,c}))$ seven days ahead from our current time of query t . Our search range for our hyperparameter ranges from $\{2, \dots, 14\}$. To prevent data leakage from the future, we follow the standard implementation of the rolling window time series cross validation procedure (c.f. Pedregosa et al. 2011). Specifically, the training-validation splits on each day are generated successively to ensure that the training set is always of an earlier date than that of the validation set. This procedure is designed to be consistent with the accumulative nature of time series data to avoid leaking information from the future.

More precisely, in our validation procedure, we generate $t - 20$ folds of training and validation pairs $\{(training_n, validation_n) : \forall n \in \{1, 2, \dots, t - 20\}\}$, where the n -th fold consists of training data from day n to $n + 13$: $training_n := \{(s, \ln(\mathbf{I}_{s,c})) : s \in \{n, n + 1, \dots, n + 13\}, c \in C\}$ and validation ground truth of all counties on the $n + 20$ -th day: $validation_n := \{(s, \ln(\mathbf{I}_{s,c})) : s \in \{n + 20\}, c \in C\}$. A detailed illustration of the training and validation data used in each fold when choosing the best δ_t is presented in Table 13.

Fold Index	Training Data	Validation Data
1	$\{(1, \ln(\mathbf{I}_{1,c})), \dots, (14, \ln(\mathbf{I}_{14,c})) \forall c \in C\}$	$\{(21, \ln(\mathbf{I}_{21,c})) \forall c \in C\}$
2	$\{(2, \ln(\mathbf{I}_{2,c})), \dots, (15, \ln(\mathbf{I}_{14,c})) \forall c \in C\}$	$\{(22, \ln(\mathbf{I}_{22,c})) \forall c \in C\}$
\vdots	\vdots	\vdots
n	$\{(n, \ln(\mathbf{I}_{n,c})), \dots, (n + 13, \ln(\mathbf{I}_{n+13,c})) \forall c \in C\}$	$\{(n + 20, \ln(\mathbf{I}_{n+20,c})) \forall c \in C\}$
\vdots	\vdots	\vdots
$t - 20$	$\{(t - 20, \ln(\mathbf{I}_{t-20,c})), \dots, (t - 7, \ln(\mathbf{I}_{t-7,c})) \forall c \in C\}$	$\{(t, \ln(\mathbf{I}_{t,c})) \forall c \in C\}$

Table 13 Training and validation data of each fold for selecting hyperparameter $\delta_t \in \{2, \dots, 14\}$ for the tcv estimator by cross-validation

For each of the folds, we then train the tcv estimators using candidate window sizes $\{2, \dots, 14\}$, forecast the incident case numbers of each county in the fold, and assess the validation error of each hyperparameter choice in each fold. The validation errors for each choice of the hyperparameter are then averaged across all folds. The hyperparameter choice with the lowest validation error is assigned to δ_t for test time evaluation (forecasting $\ln(\mathbf{I}_{t+7,c})$). This cross validation procedure and test-time evaluation is repeated for all $\delta_t : t \in \{21, \dots, T\}$.

A.2.2. ctcv Implementation Details For each county c , the ctcv estimator (20) can be directly computed from the case incidence data $\{(s, \ln(\mathbf{I}_{s,c})) : \forall s \in \{t - \delta_{t,c} + 1, \dots, t\}\}$ for any fitting window size $\delta_{t,c}$ hyperparameter, in the following fashion:

$$\hat{\mathbf{r}}_{t,c}^{\text{ols}(\delta_{t,c})} = \frac{\sum_{s=t-\delta_{t,c}+1}^t (s - \frac{\sum_{s=t-\delta_{t,c}+1}^t s}{\delta_{t,c}}) (\ln(\mathbf{I}_{s,c}) - \frac{\sum_{s=t-\delta_{t,c}+1}^t \ln(\mathbf{I}_{s,c})}{\delta_{t,c}})}{\sum_{s=t-\delta_{t,c}+1}^t \left(s - \frac{\sum_{s=t-\delta_{t,c}+1}^t s}{\delta_{t,c}} \right)^2}. \quad (32)$$

This encompasses the incidence case data of the county c from the beginning of the chosen fitting window ($t - \delta_{t,c} + 1$) to the current time of query (t). In contrast to tcv , the key characteristic of the ctcv estimator is that at each time point t , all the counties are free to use their own fitting window size hyperparameter $\delta_{t,c}$. We will now describe the cross-validation procedure to obtain the best $\delta_{t,c}$, and how the final test-time estimator is computed and evaluated.

The procedure for selecting the best hyperparameter at each time point is done independently for each county c . The test time evaluation for forecasting $\ln(\mathbf{I}_{t+7,c})$ is consistent with tcv as described in §A.2.1.

Fold Index	Training Data	Validation Data
1	$\{(1, \ln(\mathbf{I}_{1,c})), \dots, (14, \ln(\mathbf{I}_{14,c}))\}$	$\{(21, \ln(\mathbf{I}_{21,c}))\}$
2	$\{(2, \ln(\mathbf{I}_{2,c})), \dots, (15, \ln(\mathbf{I}_{14,c}))\}$	$\{(22, \ln(\mathbf{I}_{22,c}))\}$
\vdots	\vdots	\vdots
n	$\{(n, \ln(\mathbf{I}_{n,c})), \dots, (n + 13, \ln(\mathbf{I}_{n+13,c}))\}$	$\{(n + 20, \ln(\mathbf{I}_{n+20,c}))\}$
\vdots	\vdots	\vdots
$t - 20$	$\{(t - 20, \ln(\mathbf{I}_{t-20,c})), \dots, (t - 7, \ln(\mathbf{I}_{t-7,c}))\}$	$\{(t, \ln(\mathbf{I}_{t,c}))\}$

Table 14 Training and validation data of each fold for selecting hyperparameter $\delta_{t,c} \in \{2, \dots, 14\}$ for the ctcv estimator by cross-validation

Therefore, for each county c at time point t , we will generate $t - 20$ folds of training and validation pairs as per Table 14.

The hyperparameter selection process, followed by the test time evaluation (forecasting $\ln(\mathbf{I}_{t+7,c})$), will proceed similarly to the rolling window time series cross-validation procedure described in A.2.1. The only difference is that each county c will now choose its own best $\delta_{t,c}$ independently.

A.2.3. K-Means Dynamic Window Implementation Details The K-Means Dynamic Window method obtains its estimator in two steps. First, utilizing spatial information (e.g., HSA regions, Census information, Proportion of vulnerable populations), it conducts K-Means clustering on all counties in the U.S., where K is the total number of clusters. Second, once the K clusters $\{C_1, C_2, \dots, C_K\}$ have been generated, it chooses a cluster-specific fitting window for counties within the same cluster via time-based cross-validation.

We will first describe the clustering process in detail. We then describe the hyperparameter selection process for the dynamic window estimators within a given cluster.

Clustering Implementation

The goal of the clustering step is to partition all the counties of the US into $K \in \{100, 200, \dots\}$ clusters using geographic (i.e., time-invariant) information from our datasets. We first determined at the dataset level what features are time-invariant within our study:

1. The 2019 United States Census Gazetteer Files (c.f. [United States Census Bureau 2019](#)). Sample features included are:
 - Geographic Centers (Latitude, Longitude) of Counties
2. The Centers for Disease Control and Prevention Social Vulnerability Index 2018 Database (c.f. [Centers for Disease Control and Prevention 2018](#)). Sample features included are:
 - Population below the poverty line
 - Unemployment Rate
 - Proportion of Elderly (> 65 years of age)

3. The CDC SARS-CoV2 Variant Proportions Dataset (c.f. [Centers for Disease Control and Prevention 2021a](#)). We only utilize the information of which county belongs to which Health and Human Services (HHS) Region.

The K clusters are then randomly initialized using the `k-means++` procedure by [Arthur and Vassilvitskii \(2007\)](#), where the clustering procedure was run for at most 10,000 iterations.

This parallel implementation can be found on our GitHub repo: https://github.com/wangzilongri/COVID-tracking/tree/TLGRF_major_revision/analysis/benchmark_tcv_kmeans_code

Dynamic Window Selection per Cluster

For a given choice of K , once we have obtained the K clusters C_1, \dots, C_K , we can proceed with fitting the dynamic window estimator within each cluster in a similar fashion to the previously described estimators `tcv`, `ctcv`. For each county c in the k -th cluster C_k , at time point t , the K-Means Dynamic Window estimator (21) can be directly computed from the case incidence data $\{(s, \ln(\mathbf{I}_{s,c})) : \forall s \in \{t - \delta_{t,k} + 1, \dots, t\}, \forall c \in C_k\}$ for any fitting window size hyperparameter $\delta_{t,k}$, in the following fashion:

$$\hat{\mathbf{r}}_{t,k}^{ols(\delta_{t,k})} = \frac{\sum_{s=t-\delta_{t,k}+1}^t (s - \frac{\sum_{s=t-\delta_{t,k}+1}^t s}{\delta_{t,k}}) (\ln(\mathbf{I}_{s,c}) - \frac{\sum_{s=t-\delta_{t,k}+1}^t \ln(\mathbf{I}_{s,c})}{\delta_{t,k}})}{\sum_{s=t-\delta_{t,k}+1}^t \left(s - \frac{\sum_{s=t-\delta_{t,k}+1}^t s}{\delta_{t,k}} \right)^2}. \quad (33)$$

The procedure for selecting the best hyperparameter at each time point is done independently for each cluster C_k . The test time evaluation for forecasting $\ln(\mathbf{I}_{t+7,c})$ is consistent with `tcv` and `ctcv` as described in §A.2.1 and §A.2.2 respectively. Each cluster C_k independently selects its best hyperparameter $\delta_{t,k}$ at every time point t , which will be shared for all counties $c \in C_k$. Therefore, at time point t , for each cluster C_k , we will generate $t - 20$ folds of training and validation pairs as per Table 15. Once each cluster obtains its hyperparameter choices from the rolling window time series cross-validation procedure, we will proceed with the test time evaluation of forecasting $\ln(\mathbf{I}_{t+7,c})$ for all time points and all counties across all clusters.

Notably, this estimator reduces to the `tcv` estimator (19) if its fitting window size is the same for all U.S. counties each day t , i.e., $\delta_{t,k} = \delta_t$, by assigning all counties to the same cluster. In contrast, this estimator becomes the `ctcv` estimator (20) if each county is assigned to its own distinct cluster, i.e., $\delta_{t,k} = \delta_{t,c}$.

Fold Index	Training Data	Validation Data
1	$\{(1, \ln(\mathbf{I}_{1,c})), \dots, (14, \ln(\mathbf{I}_{14,c})) \forall c \in C_k\}$	$\{(21, \ln(\mathbf{I}_{21,c})) \forall c \in C_k\}$
2	$\{(2, \ln(\mathbf{I}_{2,c})), \dots, (15, \ln(\mathbf{I}_{14,c})) \forall c \in C_k\}$	$\{(22, \ln(\mathbf{I}_{22,c})) \forall c \in C_k\}$
\vdots	\vdots	\vdots
n	$\{(n, \ln(\mathbf{I}_{n,c})), \dots, (n + 13, \ln(\mathbf{I}_{n+13,c})) \forall c \in C_k\}$	$\{(n + 20, \ln(\mathbf{I}_{n+20,c})) \forall c \in C_k\}$
\vdots	\vdots	\vdots
$t - 20$	$\{(t - 20, \ln(\mathbf{I}_{t-20,c})), \dots, (t - 7, \ln(\mathbf{I}_{t-7,c})) \forall c \in C_k\}$	$\{(t, \ln(\mathbf{I}_{t,c})) \forall c \in C_k\}$

Table 15 Training and validation data of each fold for selecting hyperparameter $\delta_{t,k} \in \{2, \dots, 14\}$ for all counties in the k -th cluster at time t

The parallel implementation of this procedure can be found on our GitHub repository at: https://github.com/wangzilongri/COVID-tracking/tree/TLGRF_major_revision/analysis/benchmark_tcv_kmeans_code/cumsum_code.

Appendix B: COVID-19 Case Incidence

In epidemiology, case incidence, or incident case number, measures the number of new occurrences of a disease in a population over a specified period of time (McNutt and Krug 2016). More precisely, the incident case number at county c on day t is defined as $I_{t,c} := C_{t,c} - C_{t-\Delta t,c}$ for $t > \Delta t$, where $C_{t,c}$ and $C_{t-\Delta t,c}$ are the cumulative case number at county c up to day t and $t - \Delta t$, respectively. Case incidence describes how fast a disease spreads in a population, and thus is commonly used to guide policy decisions such as school closures (Kittitas County 2020).

Another useful measure in epidemiology is the active case number, which captures the number of still “infectious” cases. More precisely, the active case number at county c on day t is defined as

$$A_{t,c} := C_{t,c} - D_{t,c} - R_{t,c}, \quad (34)$$

where $C_{t,c}$, $D_{t,c}$ and $R_{t,c}$ are the cumulative number of cases, deaths and recoveries at county c up to day t . Clearly, calculating the active case number requires more information than calculating the incident case number, and thus may not always be feasible. In fact, we are unable to directly calculate the number of active cases as in (34), because the number of recovered cases R_t are not reported at county-level in the U.S.. In addition, we find that the cumulative number of case and death numbers are not always consistent in our dataset (c.f. The New York Times 2020), i.e., $\exists c \in C, t \in \mathbb{Z}^+ \text{ s.t. } C_{t,c} < D_{t,c}$.

To better capture COVID-19 case growth trajectories, we focus on analyzing the 22-day incident case number in this paper, i.e.

$$I_{t,c} := \begin{cases} C_{t,c} - C_{t-22,c} & , \text{ if } t \geq 23 \\ C_{t,c} & , \text{ if } 1 \leq t < 23. \end{cases} \quad (35)$$

Here, defining the incident case using a period of 22 days was based on the early practices observed during the pandemic. Specifically, patients were recommended to undergo a self-quarantine period of 17-22 days to confirm recovery from COVID-19 (c.f. Zhang 2021). Therefore, we chose the most stringent duration of 22 days to account for potential delays in resolving active cases. Notably, other studies also use a similar time to resolution of COVID-19 (c.f. Ben Phillips 2020). As such, (35) measures how quickly COVID-19 spreads in a county. In addition, (35) provides a good proxy for the active case number (34) as well, assuming that a COVID-19 case takes at most 22 days to resolve. Lastly, we use the 7-day moving average to smooth out oscillations in case number reporting (c.f. Bergman et al. 2020) and exclude $I_{t,c}$ observations with value below 20 in this study.

Appendix C: Feature Data

All feature data we used, i.e., $\{X_{t,c}\}_{t \in \mathbb{Z}^+, c \in C}$, are publicly available online. In this section, we briefly describe what these datasets are and how we incorporated them in our work.

C.1. 2019 US Census Gazetteer Files

The 2019 United States Census Gazetteer Files (c.f. [United States Census Bureau 2019](#)) were used to obtain the geographic locations (latitude-longitude centroids) of each county officially registered by the United States Census Bureau. This provides a spatial feature space for the GRF to further split upon.

C.2. Centers for Disease Control and Prevention Social Vulnerability Index 2018 Database

The Social Vulnerability Index (SVI) database (c.f. [Centers for Disease Control and Prevention 2018](#)) is a compilation of socio-economic factors such as unemployment rate, poverty rate, education attainment level etc. at the county level. These features are also included in our methodology.

C.3. COVID-19 US state policy database (CUSP)

The CUSP database (c.f. [Julia 2020](#)) tracks when each state implemented and ended policies such as mask mandates, lockdowns, economic policies in response to the COVID-19 pandemic. As such, it is a vector of features capturing daily policy changes in each state. As these policies is state-wide, we naturally extend them to the respective county level.

C.4. The COVID Tracking Project

From the COVID Tracking Project (c.f. [The Atlantic 2018](#)), we obtained the daily numbers of PCR, Antibody and Antigen tests performed and their positivity rates at each state. These are used as features in our estimation algorithm as well.

C.5. SARS-CoV2 Variant Proportions

This dataset provided by the CDC (c.f. [Centers for Disease Control and Prevention 2021b](#)) contains the mean estimate (along with its lower and upper estimation bounds) of the share of variants, e.g., “B.1”, “P.1”, “XBB.1.5”, “others” of each Health and Human Services (HHS) region every week (or biweekly if indicated) starting from the 2nd of January 2021. Each date and region record can potentially have multiple published estimates and we decided to take the latest published estimates (not later than the day of estimation). For data imputation, each county can be mapped to its HHS region and for the days in between every reporting interval, we decided to forward fill the missing entries (i.e., for the days between week T to week $T + 1$, we will use the entries from week T). For the dates beyond the last reporting date, we also decided to forward fill. For the dates before the first record, we decided to backfill, i.e., for dates before the 2nd of January 2021, we will use the entries for the 2nd of January 2021. The variants’ proportions are then normalized into percentages and joined with our current dataset to be used as features for TLFGRF

Appendix D: Feature Importance

D.1. Feature Importance by Splitting Frequency and Depth

The native `variable_importance` method of the `grf` package calculates the importance of features by tallying how often the individual trees split upon said feature weighted by how early they are split within each tree. The earlier the split, the more informative the feature is and hence it holds higher weight. More formally, if we wish to compute the feature importance of feature f , for each tree in the `grf`, we traverse the tree and check each node to see if said node split on f . The level of the node increments by 1 as we descend

the tree, with the root node having a level of 0. For every level we descend, we halve the importance of the contribution of the feature. This can be succinctly represented in equation (36),

$$\text{Importance}(f) = \sum_{b \in B} \sum_{\text{node} \in b} \mathbb{1}\{\text{node split on } f\}^{-2 \times \text{level}(\text{node})} \quad (36)$$

where B is a forest consisting of tress b ; each tree b consists of nodes (representing splits); the level of the node is given by $\text{level}(\text{node})$.

D.2. Top 20 Most Important Features

We show the Top 20 features which we presented in §D.3 and explain what each feature means in descending order of importance.

For the purposes of our algorithm, if the feature is a date, we transformed it into a vector representing how many days have elapsed since the policy was implemented, with all days before it being 0, and the start date itself being 1. For example, if a county c 's feature f date is 2020-02-05 i.e., policy f was implemented for that county on the 5th of May 2020, the feature for county c would look like:

$$\left[0, \dots, 0, \underbrace{1}_{2020-02-05}, 2, 3, \dots \right]$$

Top 20 Features in Descending Order of Importance

1. Stopped Personal Visitation in State Prisons
 - The date a state stopped personal visitations to state prisons
2. State of emergency issued
 - The date a state first issued any type of emergency declaration
3. Expanding Supplemental Nutrition Assistance Program (SNAP)
 - The date a state was approved the use of a waiver to provide many SNAP households with emergency supplementary benefits up to the maximum benefit a household can receive
4. Closed K-12 Public Schools
 - The date states closed K-12 public schools
5. Closed Bars
 - The date states closed bars statewide. Unless otherwise noted, bars are defined as establishments that derive more than 50 percent of gross revenue from the sales of alcoholic beverages
6. Expanding Medicaid benefits (1135 Waivers)
 - The date a state used a 1135 waiver to modify or waive Medicaid requirements
7. Closed Gyms
 - The date states closed gyms statewide.
8. Closed Restaurants Except Takeout
 - The date when restaurants are closed for in person dining with the exception of takeout orders

9. Closed Other Non-Essential Businesses
 - The date a state closed non-essential businesses statewide. Only included directives/orders
10. Allow/Expand Medicaid Telehealth Coverage
 - The date a state expanded Telehealth coverage for Medicaid recipients
11. Closed Movie Theaters
 - The date a state closed cinemas and theaters
12. Variant - B.1.617.2
 - Proportion of positive COVID test cases being of the 'B.1.617.2' strain, updated bi-weekly by the CDC
13. Ratio of Positive Tests
 - Ratio of Positive COVID-19 tests across a rolling 7 day average
14. Variant - Other
 - Proportion of positive COVID test cases with undetermined/unrecorded strains, updated bi-weekly by the CDC
15. Variant - AY.3
 - Proportion of positive COVID test cases being of the 'AY.3' strain, updated bi-weekly by the CDC
16. Date General Public Became Eligible for COVID-19 Vaccination
 - The date in which a state made the general public eligible for COVID-19 vaccination.
17. Date Adults Ages 30+ Became Eligible for Covid-19 Vaccination
 - The date in which a state made adults ages 30+ eligible for COVID-19 vaccination
18. Allowed Restaurants to Sell Takeout Alcohol
 - The date when restaurants, not classified as bars by percentage of revenue, are allowed to sell takeout alcohol
19. Variant - BA.1.1
 - Proportion of positive COVID test cases being of the 'BA.1.1' strain, updated bi-weekly by the CDC
20. Date Adults Ages 80+ Became Eligible for Covid-19 Vaccination
 - The date in which a state made adults ages 80+ eligible for COVID-19 vaccination

D.3. Feature Importance and Transfer Learning

As shown in the previous section, TLGRF derives much of its predictive power from transfer learning. This finding suggests that instead of relying on possibly limited historical data of a county in isolation for training, we can pool together data of counties which experienced similar events to generate a more robust and accurate rate estimate. A remaining question though is “what are the most important determinants of ‘similarity’

across counties”. Motivated by this question, in this section, we analyze the most important features used by TLGRF in determining similarity across time and space.

As in the classic GRF algorithm, we calculate the feature importance in TLGRF based on the frequency and depth of feature splitting. That is, a feature that is split more frequently in the random forest and split earlier within each decision tree holds higher weight. This feature importance calculation assigns non-zero importance to 398 out of the 468 of features incorporated in our dataset. In other words, our algorithm uses at least 398 features to determine which proxy data should be pooled together with the target data for estimation purposes.

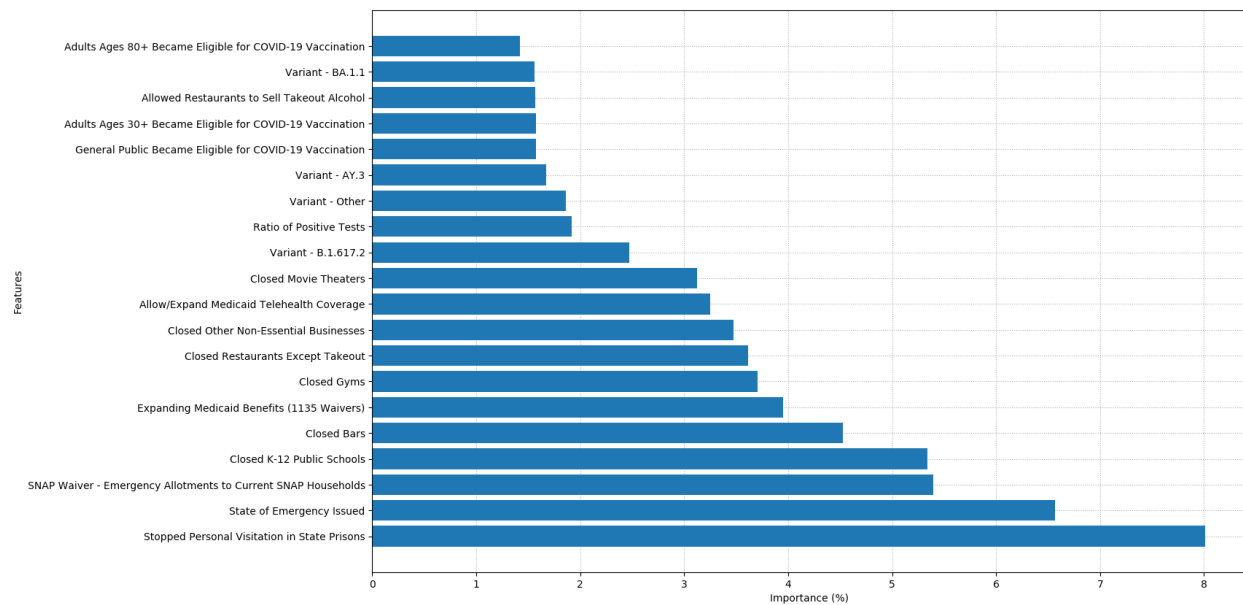


Figure 8 Top 20 most important features of TLGRF based on weighted split frequency

Figure 8 presents the top 20 most important features used by TLGRF in determining similarity in terms of COVID-19 spreading patterns. The top 20 most important features account for over 66.6% of the total feature importance. Amongst them, we first observe that policies that aim to reduce social interactions (e.g., closing of bars, closing of restaurants, closing of non-essential businesses, stopping personal visitation to prisons, state of emergency issued, closing of K12 public schools etc.) collectively account for a total of 43.7 out of 100 percent of the weighted splits. Next, safety net policies (Expanding Supplementary Nutrition Benefits, Expanding Medicaid Benefits w/ 1135 Waiver, Expanding Telehealth Coverage) account for a total of 12.6%. We then see that the proportion of positive COVID-19 tests and various strains account for 9.49%. Finally, we see that policies pertaining to the availability of vaccinations account for a total of 4.6%. These findings indicate that isolation policies, safety net policies, COVID-19 strain information, and vaccination availability provide the strongest signals in determining experienced growth rates and county similarity for our algorithm.

Appendix E: Proofs and Additional Theoretical Results

E.1. Proof for Lemmas and Theorems Stated in the Main Text

Proof of Lemma 1:

By the definition (4) of $\mathbf{r}_{t,c}$, we have

$$\begin{aligned} \mathbf{r}_{t,c} &= \mathbb{E}\left[\ln\left(\frac{\mathbf{I}_{s,c}^t}{\mathbf{I}_{s-1,c}^t}\right) \middle| \mathbf{X}_{t,c}\right] \\ &= \mathbb{E}\left[\ln(\mathbf{I}_{s,c}^t) - \ln(\mathbf{I}_{s-1,c}^t) \middle| \mathbf{X}_{t,c}\right] \\ &= \sum_{t'=2}^{\infty} \mathbb{P}[s = t' | \mathbf{X}_{t,c}] \mathbb{E}\left[\ln(\mathbf{I}_{s,c}^t) - \ln(\mathbf{I}_{s-1,c}^t) \middle| s = t', \mathbf{X}_{t,c}\right], \end{aligned}$$

which implies

$$\mathbf{r}_{t,c} = r(\mathbf{X}_{t,c})$$

by Assumption 1 as

$$\mathbb{E}[\ln(\mathbf{I}_{s,c}^t) | s, \mathbf{X}_{t,c}] = \alpha(\mathbf{X}_{t,c}) + r(\mathbf{X}_{t,c})t' + \mathbb{E}[\varepsilon_{t,c} | \mathbf{X}_{t,c}]$$

and

$$\mathbb{E}[\ln(\mathbf{I}_{s,c}^t) | s = t' - 1, \mathbf{X}_{t,c}] = \alpha(\mathbf{X}_{t,c}) + r(\mathbf{X}_{t,c})(t' - 1) + \mathbb{E}[\varepsilon_{t,c} | \mathbf{X}_{t,c}].$$

□

Proof of Theorem 1:

We aim to establish the equality (5) between the county-level instantaneous exponential growth rate and the observed log case number changes, i.e.,

$$\mathbf{r}_{t,c} = \mathbb{E}[\ln(\mathbf{I}_{s,c}^t) | s = t, \mathbf{X}_{t,c}] - \mathbb{E}[\ln(\mathbf{I}_{s,c}^{t-1}) | s = t - 1, \mathbf{X}_{t-1,c}].$$

To this end, we utilize the following decomposition:

$$\begin{aligned} &\mathbb{E}[\ln(\mathbf{I}_{s,c}^t) | s = t, \mathbf{X}_{t,c}] - \mathbb{E}[\ln(\mathbf{I}_{s,c}^{t-1}) | s = t - 1, \mathbf{X}_{t-1,c}] \\ &= (\mathbb{E}[\ln(\mathbf{I}_{s,c}^t) | s = t, \mathbf{X}_{t,c}] - \mathbb{E}[\ln(\mathbf{I}_{s,c}^t) | s = t - 1, \mathbf{X}_{t,c}]) \\ &\quad + (\mathbb{E}[\ln(\mathbf{I}_{s,c}^t) | s = t - 1, \mathbf{X}_{t,c}] - \mathbb{E}[\ln(\mathbf{I}_{s,c}^{t-1}) | s = t - 1, \mathbf{X}_{t-1,c}]). \end{aligned} \tag{37}$$

By Lemma 1, the county-level instantaneous exponential growth rate $\mathbf{r}_{t,c}$ is given by the first term in the decomposition (37), i.e.,

$$\mathbf{r}_{t,c} = \mathbb{E}[\ln(\mathbf{I}_{s,c}^t) | s = t, \mathbf{X}_{t,c}] - \mathbb{E}[\ln(\mathbf{I}_{s,c}^t) | s = t - 1, \mathbf{X}_{t,c}].$$

The second term in the decomposition (37) is 0, i.e.,

$$0 = \mathbb{E}[\ln(\mathbf{I}_{s,c}^t) | s = t - 1, \mathbf{X}_{t,c}] - \mathbb{E}[\ln(\mathbf{I}_{s,c}^{t-1}) | s = t - 1, \mathbf{X}_{t-1,c}],$$

by Assumption 2 (Overlap). Therefore, the decomposition (37) establishes the desired equality (5) under Assumptions 1 and 2. □

Proof of Theorem 2:

To begin, we take the expectation of (9) conditional on $\mathbf{X} = \mathbf{X}_{t,c}$, i.e.,

$$\begin{aligned} 0 &= \mathbb{E}[\mathbf{Y}_{t,c}(\mathbf{s}) - r(\mathbf{X})W_{t,c}(\mathbf{s}) | \mathbf{X} = \mathbf{X}_{t,c}] \\ &= \mathbb{E}[\mathbb{E}[\ln(\mathbf{I}_{s,c}) | \mathbf{s}] - \mathbb{E}[\ln(\mathbf{I}_{s,c}) | \mathbf{s} = t-1] - r(\mathbf{X})W_{t,c}(\mathbf{s}) | \mathbf{X} = \mathbf{X}_{t,c}] \\ &= \mathbb{E}[\ln(\mathbf{I}_{s,c}) - \ln(\mathbf{I}_{t-1,c}) - r(\mathbf{X})W_{t,c}(\mathbf{s}) | \mathbf{X} = \mathbf{X}_{t,c}, \mathbf{s}]. \end{aligned} \quad (38)$$

To see that (10), i.e.,

$$\mathbb{E}[(\mathbf{Y}_{t,c}(\mathbf{s}) - r(\mathbf{X})W_{t,c}(\mathbf{s})) W_{t,c}(\mathbf{s}) | \mathbf{X} = x_{t,c}] = 0$$

is a local moment condition identifying $\mathbf{r}_{t,c}$, we note that (38) implies

$$\begin{aligned} 0 &= \mathbb{E}[(\ln(\mathbf{I}_{s,c}) - \ln(\mathbf{I}_{t-1,c}) - r(\mathbf{X})W_{t,c}(\mathbf{s})) W_{t,c}(\mathbf{s}) | \mathbf{X} = \mathbf{X}_{t,c}] \\ &= \mathbb{E}[(\mathbf{Y}_{t,c}(\mathbf{s}) - r(\mathbf{X})W_{t,c}(\mathbf{s})) W_{t,c}(\mathbf{s}) | \mathbf{X} = \mathbf{X}_{t,c}], \end{aligned} \quad (39)$$

which is (10) given the realized features $x_{t,c}$.

Last, by rearranging the terms of (39), we have

$$r(x_{t,c}) = \frac{\mathbb{E}[(\mathbf{Y}_{t,c}(\mathbf{s}) W_{t,c}(\mathbf{s}) | \mathbf{X} = x_{t,c})]}{\mathbb{E}[W_{t,c}(\mathbf{s}) W_{t,c}(\mathbf{s}) | \mathbf{X} = x_{t,c}]} = \frac{\mathbb{P}(\mathbf{s} = t) \mathbb{E}[\mathbf{Y}_{t,c}(t) | \mathbf{X} = x_{t,c}]}{\mathbb{P}(\mathbf{s} = t)} = \mathbb{E}[\mathbf{Y}_{t,c}(t) | \mathbf{X} = x_{t,c}],$$

whose sample counterpart is (11). \square

The last step of the proof for Theorem 2 makes use of the identities, i.e.

$$\mathbb{V}\text{ar}[W_{t,c}(\mathbf{s}) | \mathbf{X}_{t,c}] = \mathbb{V}\text{ar}[W_{t,c}(\mathbf{s})] \quad \text{and} \quad \mathbb{E}[W_{t,c}(\mathbf{s}) | \mathbf{X}_{t,c}] = \mathbb{E}[W_{t,c}(\mathbf{s})],$$

which is from the following lemma.

LEMMA 2. *Assumption 3 implies that*

$$\mathbb{V}\text{ar}[W_{t,c}(\mathbf{s}) | \mathbf{X}_{t,c}] = \mathbb{V}\text{ar}[W_{t,c}(\mathbf{s})] \quad \text{and} \quad \mathbb{E}[W_{t,c}(\mathbf{s}) | \mathbf{X}_{t,c}] = \mathbb{E}[W_{t,c}(\mathbf{s})].$$

Proof of Lemma 2:

By Assumption 3, we have

$$r(\mathbf{X}_{t,c}) \mathbb{E}[W_{t,c}(\mathbf{s}) | \mathbf{X}_{t,c}] = \mathbb{E}[\mathbf{Y}_{t,c}(\mathbf{s}) | \mathbf{X}_{t,c}] = r(\mathbf{X}_{t,c}) \mathbb{E}[W_{t,c}(\mathbf{s})].$$

Assuming that there are enough variations in the incident case data, i.e., $\mathbb{E}[\mathbf{Y}_{t,c}(\mathbf{s}) | \mathbf{X}_{t,c}] \neq 0$, we have

$$\mathbb{E}[W_{t,c}(\mathbf{s}) | \mathbf{X}_{t,c}] = \mathbb{E}[W_{t,c}(\mathbf{s})],$$

which implies

$$\mathbb{V}\text{ar}[W_{t,c}(\mathbf{s}) | \mathbf{X}_{t,c}] = \mathbb{V}\text{ar}[W_{t,c}(\mathbf{s})]. \quad \square$$

Proof of Theorem 3:

Following §6.1 by Athey et al. (2019), the GRF estimator for $\mathbf{r}_{t,c}$ with realized features $x_{t,c}$ can be derived from the weighted moment condition (13), i.e.,

$$\sum_{t' \in [t]} \sum_{c' \in C} \gamma_{t',c'}(x_{t,c}) \mathbb{E}[(\mathbf{Y}_{t',c'}(\mathbf{s}) - r(x_{t,c})W_{t',c'}(\mathbf{s})) W_{t',c'}(\mathbf{s}) | \mathbf{X} = x_{t',c'}] = 0,$$

provided that $\forall t' \in [t], \forall c' \in C$,

- $\mathbb{E}[\mathbf{Y}_{t',c'}(\mathbf{s})|\mathbf{X} = x_{t',c'}]$, $\mathbb{E}[W_{t',c'}(s)|\mathbf{X} = x_{t',c'}]$, $\mathbb{Cov}[\mathbf{Y}_{t',c'}(\mathbf{s}), W_{t',c'}(s)|\mathbf{X} = x_{t',c'}]$ and $\mathbb{V}_{\text{or}}[W_{t',c'}(s)|\mathbf{X} = x_{t',c'}]$ are all Lipschitz continuous in $x_{t',c'}$;
- $\mathbb{V}_{\text{or}}[W_{t',c'}(s)|\mathbf{X} = x_{t',c'}]$ is invertible.

In this proof, we first check whether the above conditions hold, which shows (13). Subsequently, we derive (14) from (13).

First, $\mathbb{E}[\mathbf{Y}_{t',c'}(\mathbf{s})|\mathbf{X} = x_{t',c'}]$ is Lipschitz continuous in $x_{t',c'}$ by Assumption 4. $\mathbb{E}[W_{t',c'}(s)|\mathbf{X} = x_{t',c'}]$ and $\mathbb{V}_{\text{or}}[W_{t',c'}(s)|\mathbf{X} = x_{t',c'}]$ are constant functions of $x_{t',c'}$ by Lemma 2 and thus are Lipschitz continuous in $x_{t',c'}$. $\mathbb{Cov}[\mathbf{Y}_{t',c'}(\mathbf{s}), W_{t',c'}(s)|\mathbf{X} = x_{t',c'}]$ is Lipschitz continuous in $x_{t',c'}$ by Assumption 4 by the identity

$$\begin{aligned} \mathbb{Cov}[\mathbf{Y}_{t',c'}(\mathbf{s}), W_{t',c'}(s)|\mathbf{X} = x_{t',c'}] &= \mathbb{E}[\mathbf{Y}_{t',c'}(\mathbf{s})W_{t',c'}(s)|\mathbf{X} = x_{t',c'}] - \mathbb{E}[\mathbf{Y}_{t',c'}(\mathbf{s})|\mathbf{X} = x_{t',c'}]\mathbb{E}[W_{t',c'}(s)|\mathbf{X} = x_{t',c'}] \\ &= \mathbb{P}(\mathbf{s} = t')\mathbb{E}[\mathbf{Y}_{t',c'}(t')|\mathbf{X} = x_{t',c'}] - \mathbb{E}[\mathbf{Y}_{t',c'}(\mathbf{s})|\mathbf{X} = x_{t',c'}]\mathbb{E}[W_{t',c'}(s)] \\ &= \underbrace{\mathbb{E}[\mathbf{Y}_{t',c'}(\mathbf{s})|\mathbf{X} = x_{t',c'}]}_{L\text{-continuous}} - \underbrace{\mathbb{E}[\mathbf{Y}_{t',c'}(\mathbf{s})|\mathbf{X} = x_{t',c'}]}_{L\text{-continuous}} \underbrace{\mathbb{E}[W_{t',c'}(s)]}_{\text{constant}} \end{aligned}$$

and the fact that the difference between Lipschitz functions is Lipschitz, as is any constant times a Lipschitz function. $\mathbb{V}_{\text{or}}[W_{t',c'}(s)|\mathbf{X} = x_{t',c'}]$ is invertible because $\mathbb{V}_{\text{or}}[W_{t',c'}(s)|\mathbf{X}_{t',c'}] = \mathbb{V}_{\text{or}}[W_{t',c'}(s)]$ by Lemma 2, where $\mathbb{V}_{\text{or}}[W_{t',c'}(s)]$ is nonzero by construction. As such, we have established (13).

Second, since by construction $\mathbb{P}(\mathbf{s} = t') = \mathbb{P}(\mathbf{s} = t'') \quad \forall t', t'' \in [t]$ and $\sum_{t' \in [t]} \sum_{c' \in C} \gamma_{t',c'}(x_{t,c}) = 1$, we can rewrite (13) as

$$\begin{aligned} r(x_{t,c}) &= \frac{\sum_{t' \in [t]} \sum_{c' \in C} \gamma_{t',c'}(x_{t,c}) \mathbb{E}[(\mathbf{Y}_{t',c'}(\mathbf{s})W_{t',c'}(s)|\mathbf{X} = x_{t',c'})]}{\sum_{t' \in [t]} \sum_{c' \in C} \gamma_{t',c'}(x_{t,c}) \mathbb{E}[W_{t',c'}(s)W_{t',c'}(s)|\mathbf{X} = x_{t',c'}]} \\ &= \frac{\sum_{t' \in [t]} \sum_{c' \in C} \gamma_{t',c'}(x_{t,c}) \mathbb{P}(\mathbf{s} = t') \mathbb{E}[\mathbf{Y}_{t',c'}(t')|\mathbf{X} = x_{t',c'}]}{\sum_{t' \in [t]} \sum_{c' \in C} \gamma_{t',c'}(x_{t,c}) \mathbb{P}(\mathbf{s} = t')} \\ &= \sum_{t' \in [t]} \sum_{c' \in C} \gamma_{t',c'}(x_{t,c}) \mathbb{E}[\mathbf{Y}_{t',c'}(t')|\mathbf{X} = x_{t',c'}]. \end{aligned} \tag{40}$$

The sample counterpart of (40) is (14), i.e.,

$$\hat{\mathbf{r}}_{t,c}^{\text{TLGRF}} = \sum_{t' \in [t]} \sum_{c' \in C} \gamma_{t',c'}(\mathbf{X}_{t,c}) (\ln(\mathbf{I}_{t',c'}) - \ln(\mathbf{I}_{t'-1,c'})).$$

□

E.2. Comparing Identification Assumptions of $r_{t,c}$: Assumptions 1 and 2 vs. OLS Assumptions

This section provides a formal comparison of identification assumptions 1 and 2 with the OLS identification assumptions. We begin by deriving the OLS estimators of $\mathbf{r}_{t,c}$ for fixed fitting window sizes under standard identification assumptions, as outlined in Theorem 4. Following this, Theorem 5 establishes that the identification assumptions presented in Theorem 1 are, in fact, less restrictive than the OLS assumptions introduced in Theorem 4. Lastly, Theorem 6 highlights that the identification assumptions we employ facilitate the development of more versatile estimators of $\mathbf{r}_{t,c}$ in comparison to those derived from the OLS assumptions.

Within this section, we employ the abbreviations $\boldsymbol{\alpha}$ and \boldsymbol{r} to represent the random coefficients $\alpha(\mathbf{X})$ and $r(\mathbf{X})$, correspondingly, i.e.,

$$\boldsymbol{\alpha} := \alpha(\mathbf{X}) \quad \text{and} \quad \boldsymbol{r} := r(\mathbf{X}).$$

The conditional expectations of these coefficients, given the relevant features at county c on day t , are denoted as $\mathbb{E}[\boldsymbol{\alpha}|\mathbf{X}_{t,c}]$ and $\mathbb{E}[\boldsymbol{r}|\mathbf{X}_{t,c}]$, respectively, i.e.,

$$\mathbb{E}[\boldsymbol{\alpha}|\mathbf{X}_{t,c}] := \mathbb{E}[\alpha(\mathbf{X})|\mathbf{X} = \mathbf{X}_{t,c}] \quad \text{and} \quad \mathbb{E}[\boldsymbol{r}|\mathbf{X}_{t,c}] := \mathbb{E}[r(\mathbf{X})|\mathbf{X} = \mathbf{X}_{t,c}].$$

We first state the identification assumptions for OLS estimators:

OLS Assumption 1 (*Local Unconfoundedness*) $\forall t^- \in \{t - \delta + 1, \dots, t\}$,

$$\{\boldsymbol{\alpha}, \boldsymbol{r}, \boldsymbol{\varepsilon}_{t^-,c}\} \perp\!\!\!\perp \boldsymbol{s} \mid \mathbf{X}_{t^-,c};$$

OLS Assumption 2 (*Homogeneity*) $\forall t^- \in \{t - \delta + 1, \dots, t\}$,

$$\mathbb{E}[\boldsymbol{\alpha}|\mathbf{X}_{t,c}] = \mathbb{E}[\boldsymbol{\alpha}|\mathbf{X}_{t^-,c}], \quad \mathbb{E}[\boldsymbol{r}|\mathbf{X}_{t,c}] = \mathbb{E}[\boldsymbol{r}|\mathbf{X}_{t^-,c}], \quad \mathbb{E}[\boldsymbol{s}|\mathbf{X}_{t,c}] = \mathbb{E}[\boldsymbol{s}|\mathbf{X}_{t^-,c}], \quad \mathbb{E}[\boldsymbol{\varepsilon}_{t^-,c}|\mathbf{X}_{t,c}] = \mathbb{E}[\boldsymbol{\varepsilon}_{t^-,c}|\mathbf{X}_{t^-,c}];$$

OLS Assumption 3 (*Normalization*) $\forall t^- \in \{t - \delta + 1, \dots, t\}$,

$$\mathbb{E}[\boldsymbol{\varepsilon}_{t,c}|\mathbf{X}_{t,c}] = \mathbb{E}[\boldsymbol{\varepsilon}_{t^-,c}|\mathbf{X}_{t,c}].$$

Subsequently, we demonstrate Theorem 4 that the identification of $\boldsymbol{r}_{t,c}$ is also possible through these assumptions:

THEOREM 4. *Let $\delta \in \mathbb{Z}^+ \setminus \{1\}$ be a fixed fitting window size, and $c \in C$ be a fixed county. The county-level instantaneous exponential growth rate $\boldsymbol{r}_{t,c}$ is identified as*

$$\boldsymbol{r}_{t,c} = \frac{\text{Cov}[\ln(\mathbf{I}_{s,c}), \boldsymbol{s}|\mathbf{X}_{t,c}]}{\text{Var}[\boldsymbol{s}|\mathbf{X}_{t,c}]} \tag{41}$$

Before proving Theorem 4, we first show, in Lemma 3, that the OLS identification assumptions imply our identification assumptions. Therefore, the random coefficients in our potential growth model (2) can be denoted as

$$\boldsymbol{\alpha}_{t,c} := \alpha(\mathbf{X}_{t,c}) \quad \text{and} \quad \boldsymbol{r}_{t,c} := r(\mathbf{X}_{t,c}),$$

following from the equivalence between the random coefficient $r(\mathbf{X}_{t,c})$ and the county-level instantaneous exponential growth rate $\boldsymbol{r}_{t,c}$ demonstrated in Lemma 1.

LEMMA 3. *OLS Assumptions 1, 2, and 3 imply Assumptions 1 and 2.*

Proof of Lemma 3:

First, OLS Assumptions 1 and 2 imply Assumption 1 because

$$\begin{aligned} \mathbb{E}[\ln(\mathbf{I}_{s,c}^t)|\boldsymbol{s}, \mathbf{X}_{t,c}] &= \mathbb{E}[\alpha(\mathbf{X}_{t,c}) + r(\mathbf{X}_{t,c})\boldsymbol{s} + \boldsymbol{\varepsilon}_{t,c}|\boldsymbol{s}, \mathbf{X}_{t,c}] \\ &= \mathbb{E}[\mathbb{E}[\boldsymbol{\alpha}|\mathbf{X}_{t,c}]\boldsymbol{s}|\boldsymbol{s}, \mathbf{X}_{t,c}] + \mathbb{E}[\mathbb{E}[\boldsymbol{r}|\mathbf{X}_{t,c}]\boldsymbol{s}|\boldsymbol{s}, \mathbf{X}_{t,c}] + \mathbb{E}[\boldsymbol{\varepsilon}_{t,c}|\boldsymbol{s}, \mathbf{X}_{t,c}] \\ &= \alpha(\mathbf{X}_{t,c}) + r(\mathbf{X}_{t,c})\boldsymbol{s} + \mathbb{E}[\boldsymbol{\varepsilon}_{t,c}|\mathbf{X}_{t,c}]. \end{aligned}$$

Second, OLS Assumptions 1, 2, and 3 imply Assumption 2 because

$$\begin{aligned}
\mathbb{E}[\ln(\mathbf{I}_{s,c}^t) | \mathbf{s} = t-1, \mathbf{X}_{t,c}] &= \alpha(\mathbf{X}_{t,c}) + r(\mathbf{X}_{t,c})(t-1) + \mathbb{E}[\boldsymbol{\varepsilon}_{t,c} | \mathbf{X}_{t,c}] \\
&= \mathbb{E}[\boldsymbol{\alpha} | \mathbf{X}_{t,c}] + \mathbb{E}[r | \mathbf{X}_{t,c}](t-1) + \mathbb{E}[\boldsymbol{\varepsilon}_{t,c} | \mathbf{X}_{t,c}] \\
&= \mathbb{E}[\boldsymbol{\alpha} | \mathbf{X}_{t-1,c}] + \mathbb{E}[r | \mathbf{X}_{t-1,c}](t-1) + \mathbb{E}[\boldsymbol{\varepsilon}_{t,c} | \mathbf{X}_{t-1,c}] \\
&= \alpha(\mathbf{X}_{t-1,c}) + r(\mathbf{X}_{t-1,c})(t-1) + \mathbb{E}[\boldsymbol{\varepsilon}_{t-1,c} | \mathbf{X}_{t-1,c}] \\
&= \mathbb{E}[\ln(\mathbf{I}_{s,c}^{t-1}) | \mathbf{s} = t-1, \mathbf{X}_{t-1,c}].
\end{aligned}$$

□

Proof of Theorem 4:

Our goal is to identify $\mathbf{r}_{t,c}$ using the log case data $\{\ln(\mathbf{I}_{t^-,c})\}_{t^- \in \{t-\delta+1, \dots, t\}}$ from county c within the fitting window of size δ . To achieve this, we first observe that by OLS Assumption 2, the actual growth model (1) reduces to a homogeneous growth model, i.e.,

$$\ln(\mathbf{I}_{s,c}) = \boldsymbol{\alpha}_{t,c} + \mathbf{r}_{t,c} \mathbf{s} + \sum_{t^- = t-\delta+1}^t \mathbb{1}_{t^-}(\mathbf{s}) \boldsymbol{\varepsilon}_{t^-,c}.$$

By OLS Assumptions 1 and 2, we have

$$\begin{aligned}
\mathbb{E}[\ln(\mathbf{I}_{s,c}) - \boldsymbol{\alpha} - \mathbf{r} \mathbf{s} - \sum_{t^- = t-\delta+1}^t \mathbb{1}_{t^-}(\mathbf{s}) \boldsymbol{\varepsilon}_{t^-,c} | \mathbf{s}, \mathbf{X}_{t,c}] &= 0 \\
\Rightarrow \mathbb{E}[\mathbf{s} \ln(\mathbf{I}_{s,c}) | \mathbf{X}_{t,c}] &= \mathbb{E}[\mathbf{s} \boldsymbol{\alpha} | \mathbf{X}_{t,c}] + \mathbb{E}[\mathbf{s} \mathbf{r} \mathbf{s} | \mathbf{X}_{t,c}] + \mathbb{E}[\mathbf{s} \sum_{t^- = t-\delta+1}^t \mathbb{1}_{t^-}(\mathbf{s}) \boldsymbol{\varepsilon}_{t^-,c} | \mathbf{X}_{t,c}]. \tag{42}
\end{aligned}$$

By subtracting

$$\mathbb{E}[\ln(\mathbf{I}_{s,c}) | \mathbf{X}_{t,c}] \mathbb{E}[\mathbf{s} | \mathbf{X}_{t,c}] = \mathbb{E}[\boldsymbol{\alpha} | \mathbf{X}_{t,c}] \mathbb{E}[\mathbf{s} | \mathbf{X}_{t,c}] + \mathbb{E}[\mathbf{r} \mathbf{s} | \mathbf{X}_{t,c}] \mathbb{E}[\mathbf{s} | \mathbf{X}_{t,c}] + \mathbb{E}[\sum_{t^- = t-\delta+1}^t \mathbb{1}_{t^-}(\mathbf{s}) \boldsymbol{\varepsilon}_{t^-,c} | \mathbf{X}_{t,c}] \mathbb{E}[\mathbf{s} | \mathbf{X}_{t,c}]$$

from (42), we have

$$\text{Cov}[\ln(\mathbf{I}_{s,c}), \mathbf{s} | \mathbf{X}_{t,c}] = \text{Cov}[\boldsymbol{\alpha}, \mathbf{s} | \mathbf{X}_{t,c}] + \text{Cov}[\mathbf{r} \mathbf{s}, \mathbf{s} | \mathbf{X}_{t,c}] + \mathbb{E}[\mathbf{s} \sum_{t^- = t-\delta+1}^t \mathbb{1}_{t^-}(\mathbf{s}) \boldsymbol{\varepsilon}_{t^-,c} | \mathbf{X}_{t,c}] - \mathbb{E}[\sum_{t^- = t-\delta+1}^t \mathbb{1}_{t^-}(\mathbf{s}) \boldsymbol{\varepsilon}_{t^-,c} | \mathbf{X}_{t,c}] \mathbb{E}[\mathbf{s} | \mathbf{X}_{t,c}] \tag{43}$$

Finally, (43) implies (41) because

$$\text{Cov}[\boldsymbol{\alpha}, \mathbf{s} | \mathbf{X}_{t,c}] = 0,$$

$$\text{Cov}[\mathbf{r} \mathbf{s}, \mathbf{s} | \mathbf{X}_{t,c}] = \mathbf{r}_{t,c} \text{Var}[\mathbf{s} | \mathbf{X}_{t,c}]$$

and

$$\begin{aligned}
&\mathbb{E}[\mathbf{s} \sum_{t^- = t-\delta+1}^t \mathbb{1}_{t^-}(\mathbf{s}) \boldsymbol{\varepsilon}_{t^-,c} | \mathbf{X}_{t,c}] - \mathbb{E}[\sum_{t^- = t-\delta+1}^t \mathbb{1}_{t^-}(\mathbf{s}) \boldsymbol{\varepsilon}_{t^-,c} | \mathbf{X}_{t,c}] \mathbb{E}[\mathbf{s} | \mathbf{X}_{t,c}] \\
&= \mathbb{E}[\mathbb{E}[\mathbf{s} \sum_{t^- = t-\delta+1}^t \mathbb{1}_{t^-}(\mathbf{s}) \boldsymbol{\varepsilon}_{t^-,c} | \mathbf{s}] | \mathbf{X}_{t,c}] - \sum_{t^- = t-\delta+1}^t \mathbb{E}[\mathbb{1}_{t^-}(\mathbf{s}) | \mathbf{X}_{t,c}] \mathbb{E}[\boldsymbol{\varepsilon}_{t^-,c} | \mathbf{X}_{t,c}] \mathbb{E}[\mathbf{s} | \mathbf{X}_{t,c}] \\
&= \sum_{t^- = t-\delta+1}^t \mathbb{P}[\mathbf{s} = t^- | \mathbf{X}_{t,c}] \mathbb{E}[\mathbf{s} \sum_{t^- = t-\delta+1}^t \mathbb{1}_{t^-}(\mathbf{s}) \boldsymbol{\varepsilon}_{t^-,c} | \mathbf{s} = t^-, \mathbf{X}_{t,c}]
\end{aligned}$$

$$\begin{aligned}
& - \sum_{t^- = t - \delta + 1}^t \mathbb{E}[\mathbb{1}_{t^-}(\mathbf{s}) | \mathbf{X}_{t,c}] \mathbb{E}[\boldsymbol{\varepsilon}_{t,c} | \mathbf{X}_{t,c}] \mathbb{E}[\mathbf{s} | \mathbf{X}_{t,c}] \\
& = \sum_{t^- = t - \delta + 1}^t \mathbb{P}[\mathbf{s} = t^- | \mathbf{X}_{t,c}] \mathbb{E}[t^- \boldsymbol{\varepsilon}_{t^-,c} | \mathbf{X}_{t,c}] \\
& - \sum_{t^- = t - \delta + 1}^t \mathbb{E}[\mathbb{1}_{t^-}(\mathbf{s}) | \mathbf{X}_{t,c}] \mathbb{E}[\boldsymbol{\varepsilon}_{t,c} | \mathbf{X}_{t,c}] \mathbb{E}[\mathbf{s} | \mathbf{X}_{t,c}] \\
& = \sum_{t^- = t - \delta + 1}^t \mathbb{P}[\mathbf{s} = t^- | \mathbf{X}_{t,c}] t^- \mathbb{E}[\boldsymbol{\varepsilon}_{t^-,c} | \mathbf{X}_{t,c}] - \mathbb{E}[\boldsymbol{\varepsilon}_{t,c} | \mathbf{X}_{t,c}] \mathbb{E}[\mathbf{s} | \mathbf{X}_{t,c}] \\
& = \mathbb{E}[\boldsymbol{\varepsilon}_{t,c} | \mathbf{X}_{t,c}] \mathbb{E}[\mathbf{s} | \mathbf{X}_{t,c}] - \mathbb{E}[\boldsymbol{\varepsilon}_{t,c} | \mathbf{X}_{t,c}] \mathbb{E}[\mathbf{s} | \mathbf{X}_{t,c}] \\
& = 0
\end{aligned} \tag{44}$$

by OLS Assumptions 1, 2 and 3. \square

Subsequently, we demonstrate that the OLS identification assumptions are indeed more restrictive in comparison to ours.

THEOREM 5. *The OLS Assumptions 1, 2, and 3 imply Assumptions 1 and 2. The converse does not hold.*

Proof of Theorem 5:

The first part of this theorem is proved in Lemma 3. To demonstrate the second part of this theorem, we construct a counterexample that satisfies our identification assumptions but fails to satisfy the OLS identification assumptions. Specifically, consider

$$\ln(\mathbf{I}_{s,c}^2) = 0.5 + 0.75\mathbf{s} + \boldsymbol{\varepsilon}_{2,c} \tag{45}$$

and

$$\ln(\mathbf{I}_{s,c}^1) = 1 + 0.25\mathbf{s} + \boldsymbol{\varepsilon}_{1,c}, \tag{46}$$

where $\boldsymbol{\varepsilon}_{2,c} := 0.75\mathbf{s} - \mathbf{r}\mathbf{s}$ and $\boldsymbol{\varepsilon}_{1,c} := 0.25\mathbf{s} - \mathbf{r}\mathbf{s}$. More precisely, the parameters in this counterexample are specified as $\mathbf{r}_{2,c} = \mathbb{E}[\mathbf{r} | \mathbf{X}_{2,c}] = 0.75$, $\boldsymbol{\alpha}_{2,c} = \mathbb{E}[\boldsymbol{\alpha} | \mathbf{X}_{2,c}] = 0.5$, $\mathbf{r}_{1,c} = \mathbb{E}[\mathbf{r} | \mathbf{X}_{1,c}] = 0.25$, $\boldsymbol{\alpha}_{1,c} = \mathbb{E}[\boldsymbol{\alpha} | \mathbf{X}_{1,c}] = 1$. When $\mathbf{r} \perp\!\!\!\perp \mathbf{s} | \mathbf{X}_{2,c}$ and $\mathbf{r} \perp\!\!\!\perp \mathbf{s} | \mathbf{X}_{1,c}$, this specification satisfies Assumptions 1 and Assumption 2 but fails to satisfy OLS Assumptions 2 or 3.

To see this, we first note that $\forall t^- \in \{1, 2\}$,

$$\mathbb{E}[\boldsymbol{\varepsilon}_{t^-,c} | \mathbf{s}, \mathbf{X}_{t^-,c}] = 0,$$

because

$$\mathbb{E}[\boldsymbol{\varepsilon}_{2,c} | \mathbf{s}, \mathbf{X}_{2,c}] = \mathbb{E}[0.75\mathbf{s} - \mathbf{r}\mathbf{s} | \mathbf{s}, \mathbf{X}_{2,c}] = \mathbb{E}[\mathbb{E}[\mathbf{r} | \mathbf{X}_{2,c}] \mathbf{s} - \mathbb{E}[\mathbf{r} | \mathbf{X}_{2,c}] \mathbf{s} | \mathbf{s}, \mathbf{X}_{2,c}] = 0$$

and

$$\mathbb{E}[\boldsymbol{\varepsilon}_{1,c} | \mathbf{s}, \mathbf{X}_{1,c}] = \mathbb{E}[0.25\mathbf{s} - \mathbf{r}\mathbf{s} | \mathbf{s}, \mathbf{X}_{1,c}] = \mathbb{E}[\mathbb{E}[\mathbf{r} | \mathbf{X}_{1,c}] \mathbf{s} - \mathbb{E}[\mathbf{r} | \mathbf{X}_{1,c}] \mathbf{s} | \mathbf{s}, \mathbf{X}_{1,c}] = 0.$$

As such, (45) and (46) satisfy **Assumptions 1** by their specifications. In addition, they satisfy **Assumption 2** because

$$\mathbb{E}[\ln(\mathbf{I}_{s,c}^2) | \mathbf{s} = 1, \mathbf{X}_{2,c}] = 0.5 + 0.75 \times 1 = 1 + 0.25 \times 1 = \mathbb{E}[\ln(\mathbf{I}_{s,c}^1) | \mathbf{s} = 1, \mathbf{X}_{1,c}].$$

Therefore, as depicted in Figure 1, $\mathbf{r}_{2,c}$ is identifiable from observations (1,1.25) and (2,2) by Theorem 1, i.e.,

$$0.75 = \mathbf{r}_{2,c} = \mathbb{E}[\ln(\mathbf{I}_{s,c}) | \mathbf{s} = 2, \mathbf{X}_{2,c}] - \mathbb{E}[\ln(\mathbf{I}_{s,c}) | \mathbf{s} = 1, \mathbf{X}_{1,c}] = 2 - 1.25.$$

However, since

$$\mathbf{r}_{2,c} = 0.5 \neq 0.25 = \mathbf{r}_{1,c},$$

(45) and (46) do not satisfy **OLS Assumption 2**. In addition, since

$$\mathbb{E}[\varepsilon_{2,c} | \mathbf{X}_{2,c}] = \mathbb{E}[0.75\mathbf{s} - \mathbf{r}\mathbf{s} | \mathbf{X}_{2,c}] = \mathbb{E}[0.75\mathbf{s} - \mathbb{E}[\mathbf{r} | \mathbf{X}_{2,c}] \mathbf{s} | \mathbf{X}_{2,c}] = \mathbb{E}[0.75\mathbf{s} - 0.75\mathbf{s} | \mathbf{X}_{2,c}] = 0$$

and

$$\mathbb{E}[\varepsilon_{1,c} | \mathbf{X}_{2,c}] = \mathbb{E}[0.25\mathbf{s} - \mathbf{r}\mathbf{s} | \mathbf{X}_{2,c}] = \mathbb{E}[0.25\mathbf{s} - \mathbb{E}[\mathbf{r} | \mathbf{X}_{2,c}] \mathbf{s} | \mathbf{X}_{2,c}] = \mathbb{E}[0.25\mathbf{s} - 0.75\mathbf{s} | \mathbf{X}_{2,c}] = -0.5\mathbb{E}[\mathbf{s} | \mathbf{X}_{2,c}],$$

(45) and (46) do not satisfy **OLS Assumption 3**.

Lastly, we note that Assumptions 1 and 2 do not imply assumptions commonly employed in OLS identification such as strict or sequential ignorability, i.e.,

$$\text{Assumptions 1 and 2} \not\Rightarrow \varepsilon_{t,c} \perp\!\!\!\perp \mathbf{s} \mid \mathbf{X}_{t-1,c}.$$

To see this, we observe that specifications (45) and (46) satisfy Assumptions 1 and 2 but do not satisfy strict or sequential ignorability as

$$\begin{aligned} \text{Cov}[\mathbf{s}, \varepsilon_{2,c} | \mathbf{X}_{1,c}] &= \mathbb{E}[\mathbf{s}\varepsilon_{2,c} | \mathbf{X}_{1,c}] - \mathbb{E}[\mathbf{s} | \mathbf{X}_{1,c}]\mathbb{E}[\varepsilon_{2,c} | \mathbf{X}_{1,c}] \\ &= \mathbb{E}[\mathbf{s}(0.75\mathbf{s} - \mathbf{r}\mathbf{s}) | \mathbf{X}_{1,c}] - \mathbb{E}[\mathbf{s} | \mathbf{X}_{1,c}]\mathbb{E}[0.75\mathbf{s} - \mathbf{r}\mathbf{s} | \mathbf{X}_{1,c}] \\ &= \mathbb{E}[\mathbf{s}(0.75\mathbf{s} - \mathbb{E}[\mathbf{r} | \mathbf{X}_{1,c}]\mathbf{s}) | \mathbf{X}_{1,c}] - \mathbb{E}[\mathbf{s} | \mathbf{X}_{1,c}]\mathbb{E}[0.75\mathbf{s} - \mathbb{E}[\mathbf{r} | \mathbf{X}_{1,c}]\mathbf{s} | \mathbf{X}_{1,c}] \\ &= \mathbb{E}[\mathbf{s}(0.75\mathbf{s} - 0.25\mathbf{s}) | \mathbf{X}_{1,c}] - \mathbb{E}[\mathbf{s} | \mathbf{X}_{1,c}]\mathbb{E}[0.75\mathbf{s} - 0.25\mathbf{s} | \mathbf{X}_{1,c}] \\ &= 0.5\text{Var}[\mathbf{s} | \mathbf{X}_{2,c}] \\ &> 0. \end{aligned}$$

□

Finally, we show that our identification assumptions 1 and 2 allow for more adaptive estimators of the instantaneous county-level exponential growth rate compared to those derived from the OLS Assumptions 1 and 2.

THEOREM 6. *Any OLS estimators (41) of $\mathbf{r}_{t,c}$ with a δ -day fitting window can be expressed as a convex combination of $\delta - 1$ two-point estimators in the form (5), i.e., $\forall \delta \in \mathbb{Z}^+ \setminus \{1\}$,*

$$\frac{\text{Cov}[\ln(\mathbf{I}_{s,c}), \mathbf{s} | \mathbf{X}_{t,c}]}{\text{Var}[\mathbf{s} | \mathbf{X}_{t,c}]} = \sum_{t^- = t - \delta + 2}^t \boldsymbol{\mu}_{t^-,c} (\mathbb{E}[\ln(\mathbf{I}_{s,c}) | \mathbf{s} = t^-, \mathbf{X}_{t,c}] - \mathbb{E}[\ln(\mathbf{I}_{s,c}) | \mathbf{s} = t^- - 1, \mathbf{X}_{t,c}]), \quad (47)$$

where $\{\boldsymbol{\mu}_{t^-,c}\}_{t^- \in \{t - \delta + 2, \dots, t\}}$ are non-negative weights that sum to 1, i.e.,

$$\boldsymbol{\mu}_{t^-,c} = \frac{\sum_{i=t^-}^t \mathbb{P}[\mathbf{s} = i | \mathbf{X}_{t,c}] (i - \mathbb{E}[\mathbf{s} | \mathbf{X}_{t,c}])}{\sum_{i=t^- - \delta + 1}^t \mathbb{P}[\mathbf{s} = i | \mathbf{X}_{t,c}] (i - (t - \delta + 1))(i - \mathbb{E}[\mathbf{s} | \mathbf{X}_{t,c}])}. \quad (48)$$

As such, the sample counterpart of the OLS estimator (41) with a δ -day fitting window is

$$\hat{\mathbf{r}}_{t,c}^{ols(\delta)} = \sum_{t^- = t - \delta + 2}^t \hat{\mu}_{t^-,c} (\ln(\mathbf{I}_{t^-,c}) - \ln(\mathbf{I}_{t^- - 1,c})), \quad (49)$$

where

$$\hat{\mu}_{t^-,c} = \frac{\sum_{i=t^-}^t (i - \frac{2t - \delta + 1}{2})}{\sum_{i=t^- - \delta + 1}^t (i - (t - \delta + 1))(i - \frac{2t - \delta + 1}{2})}. \quad (50)$$

Proof of Theorem 6:

First, the numerator of the OLS estimator (41) can be rewritten as

$$\begin{aligned} \text{Cov}[\ln(\mathbf{I}_{s,c}), \mathbf{s} | \mathbf{X}_{t,c}] &= \mathbb{E}[(\ln(\mathbf{I}_{s,c}) - \mathbb{E}[\ln(\mathbf{I}_{s,c}) | \mathbf{X}_{t,c}])(\mathbf{s} - \mathbb{E}[\mathbf{s} | \mathbf{X}_{t,c}]) | \mathbf{X}_{t,c}] \\ &= \mathbb{E}[\ln(\mathbf{I}_{s,c})(\mathbf{s} - \mathbb{E}[\mathbf{s} | \mathbf{X}_{t,c}]) | \mathbf{X}_{t,c}] \\ &= \mathbb{E}[\mathbb{E}[\ln(\mathbf{I}_{s,c}) | \mathbf{s}, \mathbf{X}_{t,c}](\mathbf{s} - \mathbb{E}[\mathbf{s} | \mathbf{X}_{t,c}]) | \mathbf{X}_{t,c}] \end{aligned} \quad (51)$$

Additionally, by rewriting $r_{t^-,c}$ as (5), i.e., $\forall t^- \in \{t - \delta + 2, \dots, t\}$,

$$\mathbf{r}_{t^-,c} = \mathbb{E}[\ln(\mathbf{I}_{s,c}) | \mathbf{s} = t^-, \mathbf{X}_{t,c}] - \mathbb{E}[\ln(\mathbf{I}_{s,c}) | \mathbf{s} = t^- - 1, \mathbf{X}_{t,c}], \quad (52)$$

we have $\forall \delta \in \mathbb{Z}^+ \setminus \{1\}$, $\forall i \in \{t - \delta + 2, \dots, t\}$,

$$\begin{aligned} \mathbb{E}[\ln(\mathbf{I}_{s,c}) | \mathbf{s} = i, \mathbf{X}_{t,c}] &= \mathbf{r}_{i,c} + \mathbb{E}[\ln(\mathbf{I}_{s,c}) | \mathbf{s} = i - 1, \mathbf{X}_{t,c}] \\ &= \sum_{t^- = t - \delta + 2}^i \mathbf{r}_{t^-,c} + \mathbb{E}[\ln(\mathbf{I}_{s,c}) | \mathbf{s} = t - \delta + 1, \mathbf{X}_{t,c}]. \end{aligned} \quad (53)$$

By rewriting $\mathbb{E}[\ln(\mathbf{I}_{s,c}) | \mathbf{s}, \mathbf{X}_{t,c}]$ as (53), (51) becomes

$$\begin{aligned} \text{Cov}[\ln(\mathbf{I}_{s,c}), \mathbf{s} | \mathbf{X}_{t,c}] &= \sum_{i=t-\delta+2}^t \mathbb{P}[\mathbf{s} = i | \mathbf{X}_{t,c}] \left(\sum_{t^- = t - \delta + 2}^i \mathbf{r}_{t^-,c} + \mathbb{E}[\ln(\mathbf{I}_{s,c}) | \mathbf{s} = t - \delta + 1, \mathbf{X}_{t,c}] \right) (i - \mathbb{E}[\mathbf{s} | \mathbf{X}_{t,c}]) \\ &\quad + \mathbb{P}[\mathbf{s} = t - \delta + 1 | \mathbf{X}_{t,c}] \mathbb{E}[\ln(\mathbf{I}_{s,c}) | \mathbf{s} = t - \delta + 1, \mathbf{X}_{t,c}] (t - \delta + 1 - \mathbb{E}[\mathbf{s} | \mathbf{X}_{t,c}]) \\ &= \sum_{i=t-\delta+2}^t \sum_{t^- = t - \delta + 2}^i \mathbb{P}[\mathbf{s} = i | \mathbf{X}_{t,c}] \mathbf{r}_{t^-,c} (i - \mathbb{E}[\mathbf{s} | \mathbf{X}_{t,c}]) \\ &\quad + \sum_{i=t-\delta+1}^t \mathbb{P}[\mathbf{s} = i | \mathbf{X}_{t,c}] \mathbb{E}[\ln(\mathbf{I}_{s,c}) | \mathbf{s} = t - \delta + 1, \mathbf{X}_{t,c}] (i - \mathbb{E}[\mathbf{s} | \mathbf{X}_{t,c}]) \\ &= \sum_{t^- = t - \delta + 2}^t \sum_{i=t^-}^t \mathbb{P}[\mathbf{s} = i | \mathbf{X}_{t,c}] \mathbf{r}_{t^-,c} (i - \mathbb{E}[\mathbf{s} | \mathbf{X}_{t,c}]) \\ &\quad + \mathbb{E}[\ln(\mathbf{I}_{s,c}) | \mathbf{s} = t - \delta + 1, \mathbf{X}_{t,c}] \mathbb{E}[\mathbf{s} - \mathbb{E}[\mathbf{s} | \mathbf{X}_{t,c}] | \mathbf{X}_{t,c}] \\ &= \sum_{t^- = t - \delta + 2}^t \mathbf{r}_{t^-,c} \sum_{i=t^-}^t \mathbb{P}[\mathbf{s} = i | \mathbf{X}_{t,c}] (i - \mathbb{E}[\mathbf{s} | \mathbf{X}_{t,c}]). \end{aligned}$$

Therefore, the OLS estimator (41) can be written as

$$\begin{aligned} \frac{\text{Cov}[\ln(\mathbf{I}_{s,c}), \mathbf{s}]}{\text{Var}[\mathbf{s} | \mathbf{X}_{t,c}]} &= \sum_{t^- = t - \delta + 2}^t \frac{\sum_{i=t^-}^t \mathbb{P}[\mathbf{s} = i | \mathbf{X}_{t,c}] (i - \mathbb{E}[\mathbf{s} | \mathbf{X}_{t,c}])}{\text{Var}[\mathbf{s} | \mathbf{X}_{t,c}]} \mathbf{r}_{t^-,c} \\ &= \sum_{t^- = t - \delta + 2}^t \frac{\sum_{i=t^-}^t \mathbb{P}[\mathbf{s} = i | \mathbf{X}_{t,c}] (i - \mathbb{E}[\mathbf{s} | \mathbf{X}_{t,c}])}{\mathbb{E}[(\mathbf{s} - \mathbb{E}[\mathbf{s} | \mathbf{X}_{t,c}])(\mathbf{s} - \mathbb{E}[\mathbf{s} | \mathbf{X}_{t,c}]) | \mathbf{X}_{t,c}]} \mathbf{r}_{t^-,c} \end{aligned}$$

$$\begin{aligned}
&= \sum_{t^- = t - \delta + 2}^t \frac{\sum_{i=t^-}^t \mathbb{P}[\mathbf{s} = i | \mathbf{X}_{t,c}](i - \mathbb{E}[\mathbf{s} | \mathbf{X}_{t,c}])}{\mathbb{E}[\mathbf{s}(\mathbf{s} - \mathbb{E}[\mathbf{s} | \mathbf{X}_{t,c}]) | \mathbf{X}_{t,c}]} \mathbf{r}_{t^-,c} \\
&= \sum_{t^- = t - \delta + 2}^t \frac{\sum_{i=t^-}^t \mathbb{P}[\mathbf{s} = i | \mathbf{X}_{t,c}](i - \mathbb{E}[\mathbf{s} | \mathbf{X}_{t,c}])}{\mathbb{E}[(\mathbf{s} - (t - \delta + 1))(\mathbf{s} - \mathbb{E}[\mathbf{s} | \mathbf{X}_{t,c}]) | \mathbf{X}_{t,c}]} \mathbf{r}_{t^-,c} \\
&= \sum_{t^- = t - \delta + 2}^t \frac{\sum_{i=t^-}^t \mathbb{P}[\mathbf{s} = i | \mathbf{X}_{t,c}](i - \mathbb{E}[\mathbf{s} | \mathbf{X}_{t,c}])}{\sum_{i=t^- - \delta + 1}^t \mathbb{P}[\mathbf{s} = i | \mathbf{X}_{t,c}](i - (t - \delta + 1))(i - \mathbb{E}[\mathbf{s} | \mathbf{X}_{t,c}])} \mathbf{r}_{t^-,c}.
\end{aligned}$$

As such, by defining $\{\boldsymbol{\mu}_{t^-,c}\}_{t^- \in \{t - \delta + 2, \dots, t\}}$ and $\{\mathbf{r}_{t^-,c}\}_{t^- \in \{t - \delta + 2, \dots, t\}}$ according to (48) and (52), we have (47) and its sample counterpart (49). Notably, the sample weights (50) do not depend on features because OLS estimators with fixed window sizes are estimated using uniform sampling. That is, to estimate the instantaneous case growth rate of county c on day t using the OLS estimator with fixed window size δ , the incident case number on each past δ day is sampled with probability $\frac{1}{\delta}$, i.e., $\forall t^- \in \{t - \delta + 1, \dots, t\}$, $\mathbb{P}[\mathbf{s} = t^- | \mathbf{X}_{t,c}] = \frac{1}{\delta}$.

Lastly, we show that $\{\boldsymbol{\mu}_{t^-,c}\}_{t^- \in \{t - \delta + 2, \dots, t\}}$ are non-negative weights that sum to 1. First, $\sum_{t^- = t - \delta + 2}^t \boldsymbol{\mu}_{t^-,c} = 1$ because

$$\begin{aligned}
\sum_{t^- = t - \delta + 2}^t \boldsymbol{\mu}_{t^-,c} &= \frac{\sum_{t^- = t - \delta + 2}^t \sum_{i=t^-}^t \mathbb{P}[\mathbf{s} = i | \mathbf{X}_{t,c}](i - \mathbb{E}[\mathbf{s} | \mathbf{X}_{t,c}])}{\sum_{i=t^- - \delta + 1}^t \mathbb{P}[\mathbf{s} = i | \mathbf{X}_{t,c}](i - (t - \delta + 1))(i - \mathbb{E}[\mathbf{s} | \mathbf{X}_{t,c}])} \\
&= \frac{\sum_{i=t^- - \delta + 2}^t \sum_{t^- = t - \delta + 2}^i \mathbb{P}[\mathbf{s} = i | \mathbf{X}_{t,c}](i - \mathbb{E}[\mathbf{s} | \mathbf{X}_{t,c}])}{\sum_{i=t^- - \delta + 2}^t \mathbb{P}[\mathbf{s} = i | \mathbf{X}_{t,c}](i - (t - \delta + 1))(i - \mathbb{E}[\mathbf{s} | \mathbf{X}_{t,c}])} \\
&= \frac{\sum_{i=t^- - \delta + 2}^t (i - (t - \delta + 1)) \mathbb{P}[\mathbf{s} = i | \mathbf{X}_{t,c}](i - \mathbb{E}[\mathbf{s} | \mathbf{X}_{t,c}])}{\sum_{i=t^- - \delta + 2}^t \mathbb{P}[\mathbf{s} = i | \mathbf{X}_{t,c}](i - (t - \delta + 1))(i - \mathbb{E}[\mathbf{s} | \mathbf{X}_{t,c}])} \\
&= 1.
\end{aligned}$$

Second, to see that $\{\boldsymbol{\mu}_{t^-,c}\}_{t^- \in \{t - \delta + 2, \dots, t\}}$ are non-negative, we first demonstrate that their numerators are non-negative for any realized features $x_{t,c}$.

Case 1: $\forall t^- \in \{t - \delta + 2, \dots, t\}$ where $t^- - 1 \leq \mathbb{E}[\mathbf{s} | \mathbf{X} = x_{t,c}]$, the numerator of $\boldsymbol{\mu}_{t^-,c}$ can be expressed as

$$\begin{aligned}
&\sum_{i=t^-}^t \mathbb{P}[\mathbf{s} = i | \mathbf{X} = x_{t,c}](i - \mathbb{E}[\mathbf{s} | \mathbf{X} = x_{t,c}]) \\
&= \left(\sum_{i=t^- - \delta + 1}^t \mathbb{P}[\mathbf{s} = i | \mathbf{X} = x_{t,c}]i - \mathbb{E}[\mathbf{s} | \mathbf{X} = x_{t,c}] \right) - \sum_{i=t^- - \delta + 1}^{t^- - 1} (\mathbb{P}[\mathbf{s} = i | \mathbf{X} = x_{t,c}]i - \mathbb{P}[\mathbf{s} = i | \mathbf{X} = x_{t,c}]\mathbb{E}[\mathbf{s} | \mathbf{X} = x_{t,c}]) \\
&= \sum_{i=t^- - \delta + 1}^{t^- - 1} (\mathbb{E}[\mathbf{s} | \mathbf{X} = x_{t,c}] - i) \mathbb{P}[\mathbf{s} = i | \mathbf{X} = x_{t,c}] \\
&\geq 0,
\end{aligned}$$

which is non-negative.

Case 2: $\forall t^- \in \{t - \delta + 2, \dots, t\}$ where $t^- - 1 > \mathbb{E}[\mathbf{s} | \mathbf{X} = x_{t,c}]$, the numerator of $\boldsymbol{\mu}_{t^-,c}$ is positive, i.e.,

$$\sum_{i=t^-}^t \mathbb{P}[\mathbf{s} = i | \mathbf{X} = x_{t,c}](i - \mathbb{E}[\mathbf{s} | \mathbf{X} = x_{t,c}]) > 0.$$

By combining Case 1 and Case 2, we thus prove that the numerator of each $\mu_{t-,c}$ is non-negative for any realized features $x_{t,c}$.

In addition, since $\sum_{i=t-\delta+2}^t \mu_{i-,c} = 1$, the denominator of each $\mu_{t-,c}$, as a sum of non-negative numerators, is also non-negative. Hence $\{\mu_{t-,c}\}_{t \in \{t-\delta+2, \dots, t\}}$ are non-negative. \square

Lastly, we state and prove a useful lemma that clarifies the distribution of OLS weights (50).

LEMMA 4. *The OLS weights $\{\hat{\mu}_{t-,c}\}_{t \in \{t-\delta+2, \dots, t\}}$, where*

$$\hat{\mu}_{t-,c} = \frac{\sum_{i=t-\delta+2}^t (i - \frac{2t-\delta+1}{2})}{\sum_{i=t-\delta+1}^t (i - (t - \delta + 1))(i - \frac{2t-\delta+1}{2})},$$

are concentrated towards the center, i.e.,

$\hat{\mu}_{t,c} = 1$ when $\delta = 2$, $\hat{\mu}_{t,c} = \hat{\mu}_{t-1,c}$ when $\delta = 3$, and

$$\hat{\mu}_{t,c} < \dots < \hat{\mu}_{\lfloor \frac{2t-\delta+2}{2} \rfloor, c} = \hat{\mu}_{\lceil \frac{2t-\delta+2}{2} \rceil, c} > \dots > \hat{\mu}_{t-\delta+2, c}$$

when $\delta > 3$.

Proof of Lemma 4:

The first two claims, i.e., $\hat{\mu}_{t,c} = 1$ when $\delta = 2$, $\hat{\mu}_{t,c} = \hat{\mu}_{t-1,c}$ when $\delta = 3$, can be directly verified.

To see that the third claim is true, we first verify $\hat{\mu}_{\lfloor \frac{2t-\delta+2}{2} \rfloor, c} = \hat{\mu}_{\lceil \frac{2t-\delta+2}{2} \rceil, c}$. When δ is an even number, we have $\lfloor \frac{2t-\delta+2}{2} \rfloor = \lceil \frac{2t-\delta+2}{2} \rceil$, which directly implies $\hat{\mu}_{\lfloor \frac{2t-\delta+2}{2} \rfloor, c} = \hat{\mu}_{\lceil \frac{2t-\delta+2}{2} \rceil, c}$. When δ is an odd number, we have

$$\begin{aligned} \hat{\mu}_{\lceil \frac{2t-\delta+2}{2} \rceil, c} &= \frac{\sum_{i=\lceil \frac{2t-\delta+2}{2} \rceil}^t (i - \frac{2t-\delta+1}{2})}{\sum_{i=t-\delta+1}^t (i - (t - \delta + 1))(i - \frac{2t-\delta+1}{2})} \\ &= \frac{\sum_{i=\lfloor \frac{2t-\delta+2}{2} \rfloor}^t (i - \frac{2t-\delta+1}{2}) - (\frac{2t-\delta+1}{2} - \frac{2t-\delta+1}{2})}{\sum_{i=t-\delta+1}^t (i - (t - \delta + 1))(i - \frac{2t-\delta+1}{2})} \\ &= \frac{\sum_{i=\lfloor \frac{2t-\delta+2}{2} \rfloor}^t (i - \frac{2t-\delta+1}{2})}{\sum_{i=t-\delta+1}^t (i - (t - \delta + 1))(i - \frac{2t-\delta+1}{2})} \\ &= \hat{\mu}_{\lfloor \frac{2t-\delta+2}{2} \rfloor, c}. \end{aligned}$$

Additionally, for all $\eta \in \mathbb{Z}^+$ such that $t - \delta + 2 < \lfloor \frac{2t-\delta+2}{2} \rfloor - \eta < \lceil \frac{2t-\delta+2}{2} \rceil + \eta < t$, we have $\hat{\mu}_{\lceil \frac{2t-\delta+2}{2} \rceil + \eta, c} > \hat{\mu}_{\lfloor \frac{2t-\delta+2}{2} \rfloor + \eta + 1, c}$, i.e.,

$$\begin{aligned} \hat{\mu}_{\lceil \frac{2t-\delta+2}{2} \rceil + \eta + 1, c} &= \frac{\sum_{i=\lceil \frac{2t-\delta+2}{2} \rceil + \eta + 1}^t (i - \frac{2t-\delta+1}{2})}{\sum_{i=t-\delta+1}^t (i - (t - \delta + 1))(i - \frac{2t-\delta+1}{2})} \\ &= \frac{\sum_{i=\lceil \frac{2t-\delta+2}{2} \rceil + \eta}^t (i - \frac{2t-\delta+1}{2}) - (\lceil \frac{2t-\delta+2}{2} \rceil + \eta + 1 - \frac{2t-\delta+1}{2})}{\sum_{i=t-\delta+1}^t (i - (t - \delta + 1))(i - \frac{2t-\delta+1}{2})} \\ &< \frac{\sum_{i=\lceil \frac{2t-\delta+2}{2} \rceil + \eta}^t (i - \frac{2t-\delta+1}{2})}{\sum_{i=t-\delta+1}^t (i - (t - \delta + 1))(i - \frac{2t-\delta+1}{2})} \\ &= \hat{\mu}_{\lceil \frac{2t-\delta+2}{2} \rceil + \eta, c}, \end{aligned}$$

and $\hat{\mu}_{\lfloor \frac{2t-\delta+2}{2} \rfloor - \eta, c} > \hat{\mu}_{\lfloor \frac{2t-\delta+2}{2} \rfloor - \eta - 1, c}$, i.e.,

$$\hat{\mu}_{\lfloor \frac{2t-\delta+2}{2} \rfloor - \eta - 1, c} = \frac{\sum_{i=\lfloor \frac{2t-\delta+2}{2} \rfloor - \eta - 1}^t (i - \frac{2t-\delta+1}{2})}{\sum_{i=t-\delta+1}^t (i - (t - \delta + 1))(i - \frac{2t-\delta+1}{2})}$$

$$\begin{aligned}
&= \frac{\sum_{i=\lfloor \frac{2t-\delta+2}{2} \rfloor - \eta}^t (i - \frac{2t-\delta+1}{2}) + (\lfloor \frac{2t-\delta+2}{2} \rfloor - \eta - 1 - \frac{2t-\delta+1}{2})}{\sum_{i=t-\delta+1}^t (i - (t - \delta + 1))(i - \frac{2t-\delta+1}{2})} \\
&< \frac{\sum_{i=\lfloor \frac{2t-\delta+2}{2} \rfloor - \eta}^t (i - \frac{2t-\delta+1}{2})}{\sum_{i=t-\delta+1}^t (i - (t - \delta + 1))(i - \frac{2t-\delta+1}{2})} \\
&= \hat{\mu}_{\lfloor \frac{2t-\delta+2}{2} \rfloor - \eta, c}.
\end{aligned}$$

As such, we have shown that for $\delta > 3$,

$$\hat{\mu}_{t,c} < \cdots < \hat{\mu}_{\lfloor \frac{2t-\delta+2}{2} \rfloor, c} = \hat{\mu}_{\lceil \frac{2t-\delta+2}{2} \rceil, c} > \cdots > \hat{\mu}_{t-\delta+2,c}.$$

□

E.3. Derivations for TLGRF δ Estimators

To derive the TLGRF δ estimators (26), this section follows the same steps as in §4. Specifically, we first characterize the local moment condition corresponding to the initial estimator and subsequently the weighted moment conditions that yield the TLGRF δ estimators.

First, Theorem 7 characterizes the local moment condition of an initial estimator with a δ -day fitting window.

THEOREM 7. *Under OLS Assumptions 1, 2, and 3, an instantaneous county-level exponential growth rate $\mathbf{r}_{t,c}$ with realized features $x_{t,c}$ can be estimated from data $\{\ln(\mathbf{I}_{t^-,c}), \ln(\mathbf{I}_{t^--1,c}), x_{t^-,c}\}_{t^- \in \{t-\delta+2, \dots, t\}}$ using the OLS estimator with a δ -day fitting window (49). The corresponding local moment condition of this estimator is*

$$\sum_{t^- = t-\delta+2}^t \hat{\mu}_{t^-,c} \mathbb{E}[(\mathbf{Y}_{t^-,c}(\mathbf{s}) - r(\mathbf{X})W_{t^-,c}(\mathbf{s})) W_{t^-,c}(\mathbf{s}) | \mathbf{X} = x_{t^-,c}] = 0. \quad (54)$$

where random variables $\{\mathbf{Y}_{t^-,c}(\mathbf{s}), W_{t^-,c}(\mathbf{s})\}_{t^- \in \{t-\delta+2, \dots, t\}}$ and weights $\{\hat{\mu}_{t^-,c}\}_{t^- \in \{t-\delta+2, \dots, t\}}$ are defined in (8) and (50), respectively.

Proof of Theorem 7:

By Theorems 4 and 6, the OLS estimator with a δ -day fitting window (49), i.e.,

$$\hat{\mathbf{r}}_{t,c}^{ols(\delta)} = \sum_{t^- = t-\delta+2}^t \hat{\mu}_{t^-,c} (\ln(\mathbf{I}_{t^-,c}) - \ln(\mathbf{I}_{t^--1,c})),$$

is an unbiased estimator of $\mathbf{r}_{t,c}$ under OLS Assumptions 1 and 2. In addition, by Theorem 2, the two-point estimator (11), i.e.,

$$\hat{\mathbf{r}}_{t^-,c} = \ln(\mathbf{I}_{t^-,c}) - \ln(\mathbf{I}_{t^--1,c}),$$

is an unbiased estimator of $\mathbf{r}_{t^-,c}$, $\forall t^- \in \{t-\delta+2, \dots, t\}$. As such, the corresponding local moment condition of (49) is

$$\sum_{t^- = t-\delta+2}^t \hat{\mu}_{t^-,c} \mathbb{E}[\mathbf{r} | \mathbf{X}_{t^-,c}] = \sum_{t^- = t-\delta+2}^t \hat{\mu}_{t^-,c} \mathbb{E}[(\mathbb{E}[\ln(\mathbf{I}_{s,c}) | \mathbf{s} = t^-, \mathbf{X}_{t^-,c}] - \mathbb{E}[\ln(\mathbf{I}_{s,c}) | \mathbf{s} = t^- - 1, \mathbf{X}_{t^-,c}]) | \mathbf{X}_{t^-,c}],$$

which is equivalent to (54) as

$$\begin{aligned}
0 &= \sum_{t^- = t - \delta + 2}^t \hat{\mu}_{t^-, c} \mathbb{E}[(\mathbb{E}[\ln(\mathbf{I}_{s,c}) | \mathbf{s} = t^-, \mathbf{X}_{t^-, c}] - \mathbb{E}[\ln(\mathbf{I}_{s,c}) | \mathbf{s} = t^- - 1, \mathbf{X}_{t^-, c}]) - \mathbb{E}[r | \mathbf{X}_{t^-, c}] | \mathbf{X}_{t^-, c}] \\
&= \sum_{t^- = t - \delta + 2}^t \hat{\mu}_{t^-, c} \mathbb{P}[\mathbf{s} = t^-] \mathbb{E}[\mathbb{1}_{t^-}(\mathbf{s}) (\mathbb{E}[\ln(\mathbf{I}_{s,c}) | \mathbf{s}, \mathbf{X}_{t^-, c}] - \mathbb{E}[\ln(\mathbf{I}_{s,c}) | \mathbf{s} = t^- - 1, \mathbf{X}_{t^-, c}]) - r(\mathbf{X}_{t^-, c}) | \mathbf{s} = t^-, \mathbf{X}_{t^-, c}] \\
&= \sum_{t^- = t - \delta + 2}^t \hat{\mu}_{t^-, c} \mathbb{P}[\mathbf{s} = t^-] \mathbb{E}[\mathbf{Y}_{t^-, c}(\mathbf{s}) - r(\mathbf{X}_{t^-, c}) W_{t^-, c}(\mathbf{s}) | \mathbf{s} = t^-, \mathbf{X}_{t^-, c}] \\
&= \sum_{t^- = t - \delta + 2}^t \hat{\mu}_{t^-, c} \mathbb{E}[(\mathbf{Y}_{t^-, c}(\mathbf{s}) - r(\mathbf{X}_{t^-, c}) W_{t^-, c}(\mathbf{s})) W_{t^-, c}(\mathbf{s}) | \mathbf{s} = t^-, \mathbf{X}_{t^-, c}].
\end{aligned}$$

□

Second, Theorem 8 characterizes the weighted moment conditions that yield the TLGRF δ estimators.

THEOREM 8. *For any county $c, c' \in C$ on any day $t' \in [t^-]$ with realized features $x_{t^-, c}$ and $x_{t', c'}$ such that $x_{t', c'} \in \bigcup_{b \in B} L_b(x_{t^-, c})$, its instantaneous county-level exponential growth rate $\mathbf{r}_{t^-, c}$ can be estimated from data $\{\{\ln(\mathbf{I}_{t', c'}), \ln(\mathbf{I}_{t'-1, c'}), x_{t', c'}\}_{t' \in [t^-], c' \in C}\}_{t^- \in \{t - \delta + 2, \dots, t\}}$ via the weighted moment condition*

$$\sum_{t^- = t - \delta + 2}^t \hat{\mu}_{t^-, c} \sum_{c' \in C} \sum_{t' \in [t^-]} \gamma_{t', c'}(x_{t^-, c}) \mathbb{E}[(\mathbf{Y}_{t', c'}(\mathbf{s}) - r(x_{t^-, c}) W_{t', c}(\mathbf{s})) W_{t', c'}(\mathbf{s}) | \mathbf{X} = x_{t', c'}] = 0, \quad (55)$$

resulting in the following TLGRF δ estimator:

$$\hat{\mathbf{r}}_{t^-, c}^{TLGRF(\delta)} = \sum_{t^- = t - \delta + 2}^t \hat{\mu}_{t^-, c} \sum_{c' \in C} \sum_{t' \in [t^-]} \gamma_{t', c'}(\mathbf{X}_{t^-, c}) (\ln(\mathbf{I}_{t', c'}) - \ln(\mathbf{I}_{t'-1, c'})), \quad (56)$$

where weights $\{\hat{\mu}_{t^-, c}\}_{t^- \in \{t - \delta + 2, \dots, t\}}$ are defined in (50).

Proof of Theorem 8:

By Theorem 3, $\forall t^- \in \{t - \delta + 2, \dots, t\}$, $\mathbf{r}_{t^-, c}$ can be estimated from data $\{\{\ln(\mathbf{I}_{t', c'}), \ln(\mathbf{I}_{t'-1, c'}), x_{t', c'}\}_{t' \in [t^-], c' \in C}\}$ via the weighted moment condition

$$\sum_{c' \in C} \sum_{t' \in [t^-]} \gamma_{t', c'}(x_{t^-, c}) \mathbb{E}[(\mathbf{Y}_{t', c'}(\mathbf{s}) - r(x_{t^-, c}) W_{t', c}(\mathbf{s})) W_{t', c'}(\mathbf{s}) | \mathbf{X} = x_{t', c'}] = 0, \quad (57)$$

which yields the estimator

$$\hat{\mathbf{r}}(\mathbf{X}_{t^-, c}) = \sum_{c' \in C} \sum_{t' \in [t^-]} \gamma_{t', c'}(\mathbf{X}_{t^-, c}) (\ln(\mathbf{I}_{t', c'}) - \ln(\mathbf{I}_{t'-1, c'})). \quad (58)$$

Clearly, (57) implies (55). In addition, (58) implies (56) by Theorem 6. □

E.4. Analytical Results of the Bias-variance Trade-off for Instantaneous Growth Rate Estimations

This section examines how the choice of fitting window size affects the bias-variance trade-off in estimating instantaneous growth rates.

First, we obtain the standard bias-variance decomposition of an estimator's MSE:

THEOREM 9. *For any estimator $\hat{r}_{t,c}$ of the county-level instantaneous exponential growth rate $r(x_{t,c})$, its Mean-squared error (MSE) has the following bias-variance decomposition:*

$$\mathbb{E}[(r(\mathbf{X}) - \hat{r}_{t,c})^2 | \mathbf{X} = x_{t,c}] = \underbrace{(r(x_{t,c}) - \mathbb{E}[\hat{r}_{t,c} | \mathbf{X} = x_{t,c}])^2}_{\text{Bias}} + \underbrace{\text{Var}[\hat{r}_{t,c} | \mathbf{X} = x_{t,c}]}_{\text{Variance}}. \quad (59)$$

Second, We provide an analytical result for how the bias-variance trade-off of OLS estimators is affected by their fitting window sizes:

COROLLARY 1. *For an OLS estimator with δ -day fitting window ($\hat{r}_{t,c}^{\text{ols}(\delta)}$), its MSE, i.e.,*

$$\begin{aligned} & \mathbb{E}\left[\left(r(\mathbf{X}) - \hat{r}_{t,c}^{\text{ols}(\delta)}\right)^2 \mid \mathbf{X} = x_{t,c}\right] \\ &= \underbrace{\left(r(x_{t,c}) - \mathbb{E}\left[\sum_{t^- = t - \delta + 2}^t \hat{\mu}_{t^-,c} (\ln(\mathbf{I}_{t^-,c}) - \ln(\mathbf{I}_{t^- - 1,c})) \mid \mathbf{X} = x_{t,c}\right]\right)^2}_{\text{Bias}} \\ &+ \underbrace{\text{Var}\left[\sum_{t^- = t - \delta + 2}^t \hat{\mu}_{t^-,c} (\ln(\mathbf{I}_{t^-,c}) - \ln(\mathbf{I}_{t^- - 1,c})) \mid \mathbf{X} = x_{t,c}\right]}_{\text{Variance}}, \end{aligned} \quad (60)$$

has a zero bias term when $\delta = 2$ and has an asymptotically vanishing variance term when $\delta = t$.

Notably, changing the fitting window size δ cannot strike the right balance for the bias-variance tradeoff in (60) due to the non-adaptive weighting scheme $\{\hat{\mu}_{t^-,c}\}_{t^- \in \{t - \delta + 2, \dots, t\}}$.

In contrast, through adaptive weighting, the TLGRF estimator $\hat{r}_{t,c}^{\text{TLGRF}}$ can more effectively balance the bias and variance tradeoff in its MSE:

$$\begin{aligned} & \mathbb{E}\left[\left(r(\mathbf{X}) - \hat{r}_{t,c}^{\text{TLGRF}}\right)^2 \mid \mathbf{X} = x_{t,c}\right] \\ &= \underbrace{\left(r(x_{t,c}) - \mathbb{E}\left[\sum_{t' \in [t]} \sum_{c' \in C} \gamma_{t',c'}(\mathbf{X}) (\ln(\mathbf{I}_{t',c'}) - \ln(\mathbf{I}_{t' - 1,c'})) \mid \mathbf{X} = x_{t,c}\right]\right)^2}_{\text{Bias}} \\ &+ \underbrace{\text{Var}\left[\sum_{t' \in [t]} \sum_{c' \in C} \gamma_{t',c'}(\mathbf{X}) (\ln(\mathbf{I}_{t',c'}) - \ln(\mathbf{I}_{t' - 1,c'})) \mid \mathbf{X} = x_{t,c}\right]}_{\text{Variance}}. \end{aligned} \quad (61)$$

That is, by selecting $\{\gamma_{t',c'}(x_{t,c})\}_{t' \in [t], c' \in C}$ to minimize (61), one can achieve better or at least equal MSE compared to selecting δ to minimize (60).¹ The key insight here is that TLGRF offers a generalized approach to solving the fitting window selection problem by transforming it into a weight assignment problem.

¹ Particularly, (61) would yield the same value as (60) if we choose the weights $\gamma_{t',c'}(x_{t,c}) = \hat{\mu}_{t',c} \quad \forall t' \in \{t - \delta + 2, \dots, t\}$ and $\gamma_{t',c'}(x_{t,c}) = 0 \quad \forall t' \in \{2, \dots, t - \delta + 1\}$ or $\forall c' \in C \setminus \{c\}$.

Third, we discuss how TLGRF manages its bias-variance trade-off. Notably, balancing the bias-variance trade-off for TLGRF essentially involves choosing $\hat{r}_{t,c}^{TLGRF}$ to minimize (61). However, since the ground truth, i.e., growth rate $r(x_{t,c})$, is not observable, optimizing (61) empirically requires certain transformations. For example, choosing $\hat{r}_{t,c}^{TLGRF}$ to minimize (61) is equivalent to choosing $\hat{r}_{t,c}^{TLGRF}$ to maximize

$$r^2(x_{t,c}) - \mathbb{E}[(r(\mathbf{X}) - \hat{r}_{t,c}^{TLGRF})^2 | \mathbf{X} = x_{t,c}]. \quad (62)$$

Athey and Imbens (2016) observed that if $\mathbb{E}[\hat{r}_{t,c}^{TLGRF} | \mathbf{X} = x_{t,c}] = r(x_{t,c})$, the sample counterpart of (62) reduces to $(\hat{r}_{t,c}^{TLGRF})^2$, which is directly measurable and thus can be optimized empirically. Subsequently, Athey et al. (2019) further relaxed this assumption and demonstrated that their GRF method achieves consistency if the parameter of interest is identifiable by a local moment condition. Therefore, to balance the bias-variance trade-off of TLGRF, we first find a local moment condition that identifies $r(x_{t,c})$ in §4.1 and subsequently apply the GRF algorithm to obtain a consistent final estimator in §4.2.

Proofs for this section:

Proof of Theorem 9:

$$\begin{aligned} & \mathbb{E}[(r(\mathbf{X}) - \hat{r}_{t,c})^2 | \mathbf{X} = x_{t,c}] \\ &= r^2(x_{t,c}) - 2r(x_{t,c})\mathbb{E}[\hat{r}_{t,c} | \mathbf{X} = x_{t,c}] + \mathbb{E}[\hat{r}_{t,c}^2 | \mathbf{X} = x_{t,c}] \\ &= r^2(x_{t,c}) - 2r(x_{t,c})\mathbb{E}[\hat{r}_{t,c} | \mathbf{X} = x_{t,c}] + \mathbb{E}[\hat{r}_{t,c}^2 | \mathbf{X} = x_{t,c}] + (\mathbb{E}[\hat{r}_{t,c} | \mathbf{X} = x_{t,c}])^2 - (\mathbb{E}[\hat{r}_{t,c} | \mathbf{X} = x_{t,c}])^2 \\ &= r^2(x_{t,c}) - 2r(x_{t,c})\mathbb{E}[\hat{r}_{t,c} | \mathbf{X} = x_{t,c}] + (\mathbb{E}[\hat{r}_{t,c} | \mathbf{X} = x_{t,c}])^2 + \mathbb{E}[\hat{r}_{t,c}^2 | \mathbf{X} = x_{t,c}] - (\mathbb{E}[\hat{r}_{t,c} | \mathbf{X} = x_{t,c}])^2 \\ &= \underbrace{(r(x_{t,c}) - \mathbb{E}[\hat{r}_{t,c} | \mathbf{X} = x_{t,c}])^2}_{\text{Bias}} + \underbrace{\mathbb{V}\text{ar}[\hat{r}_{t,c} | \mathbf{X} = x_{t,c}]}_{\text{Variance}}. \end{aligned}$$

□

Proof of Corollary 1:

By Theorem 6, an OLS estimator with δ -day fitting window can be expressed as:

$$\hat{r}_{t,c}^{ols(\delta)} = \sum_{t^- = t - \delta + 2}^t \hat{\mu}_{t^-,c} (\ln(\mathbf{I}_{t^-,c}) - \ln(\mathbf{I}_{t^- - 1,c})),$$

where

$$\hat{\mu}_{t^-,c} = \frac{\sum_{i=t^-}^t (i - \frac{2t - \delta + 1}{2})}{\sum_{i=t^- - \delta + 1}^t (i - (t - \delta + 1))(i - \frac{2t - \delta + 1}{2})}.$$

First, when $\delta = 2$, the bias term of its MSE (59), i.e.,

$$r(x_{t,c}) - \mathbb{E}[\ln(\mathbf{I}_{t,c}) - \ln(\mathbf{I}_{t-1,c}) | \mathbf{X} = x_{t,c}],$$

is zero by Theorem 1.

Second, when $\delta = t$, we show that the variance term of its MSE (59) vanishes asymptotically, i.e.,

$$\lim_{t \rightarrow \infty} \mathbb{V}\text{ar}[\hat{r}_{t,c}^{ols(\delta)} | \mathbf{X} = x_{t,c}] = 0. \quad (63)$$

To see this, We first note that the variance term can be upper-bounded in the following fashion:

$$\begin{aligned}
& \text{Var}[\hat{\mathbf{r}}_{t,c}^{ols(\delta)} | \mathbf{X} = x_{t,c}] \\
&= \text{Var}\left[\sum_{t^-=2}^t \hat{\mu}_{t^-,c} (\ln(\mathbf{I}_{t^-,c}) - \ln(\mathbf{I}_{t^--1,c})) | \mathbf{X} = x_{t,c}\right] \\
&= \sum_{t'=2}^t \sum_{t''=2}^t \hat{\mu}_{t',c} \hat{\mu}_{t'',c} \text{Cov}[\ln(\mathbf{I}_{t',c}) - \ln(\mathbf{I}_{t'-1,c}), \ln(\mathbf{I}_{t'',c}) - \ln(\mathbf{I}_{t''-1,c}) | \mathbf{X} = x_{t,c}] \\
&\leq \sum_{t'=2}^t \sum_{t''=2}^t (\hat{\mu}_{\lfloor \frac{t+2}{2} \rfloor, c})^2 \left| \text{Cov}[\ln(\mathbf{I}_{t',c}) - \ln(\mathbf{I}_{t'-1,c}), \ln(\mathbf{I}_{t'',c}) - \ln(\mathbf{I}_{t''-1,c}) | \mathbf{X} = x_{t,c}] \right| \tag{64}
\end{aligned}$$

$$= (\hat{\mu}_{\lfloor \frac{t+2}{2} \rfloor, c})^2 \sum_{t'=2}^t \sum_{t''=2}^t \left| \text{Cov}[\ln(\mathbf{I}_{t',c}) - \ln(\mathbf{I}_{t'-1,c}), \ln(\mathbf{I}_{t'',c}) - \ln(\mathbf{I}_{t''-1,c}) | \mathbf{X} = x_{t,c}] \right|, \tag{65}$$

where (64) follows from Lemma 4, i.e.,

$$\hat{\mu}_{t,c} < \cdots < \hat{\mu}_{\lfloor \frac{t+2}{2} \rfloor, c} = \hat{\mu}_{\lceil \frac{t+2}{2} \rceil, c} > \cdots > \hat{\mu}_{t-\delta+2,c}.$$

Therefore, to show (63), it suffices to show (65) approaches zero as t approaches infinity.

In addition, as a sufficient condition for ergodicity of second moments, it is common to assume that the autocovariance is absolutely summable, i.e.,

$$\lim_{t \rightarrow \infty} \sum_{t'=2}^t \sum_{t''=2}^t \left| \text{Cov}[\ln(\mathbf{I}_{t',c}) - \ln(\mathbf{I}_{t'-1,c}), \ln(\mathbf{I}_{t'',c}) - \ln(\mathbf{I}_{t''-1,c}) | \mathbf{X} = x_{t,c}] \right| < \infty,$$

when proving limit theorems for serially dependent observations (Hamilton 2020).

As such, to show (65) approaches zero as t approaches infinity, it suffices to show that

$$\lim_{t \rightarrow \infty} (\hat{\mu}_{\lfloor \frac{t+2}{2} \rfloor, c})^2 = 0. \tag{66}$$

In fact, by fixing the fitting window size $\delta = t$, we have

$$\begin{aligned}
\hat{\mu}_{\lfloor \frac{t+2}{2} \rfloor, c} &= \frac{\sum_{i=\lfloor \frac{t+2}{2} \rfloor}^t (i - \frac{2t-t+1}{2})}{\sum_{i=t-t+1}^t (i - (t-t+1))(i - \frac{2t-t+1}{2})} \\
&= \frac{\sum_{i=\lfloor \frac{t+2}{2} \rfloor}^t (i - \frac{t+1}{2})}{\sum_{i=1}^t (i-1)(i - \frac{t+1}{2})} \\
&= \frac{\frac{1}{2} (t - \lfloor \frac{t}{2} \rfloor) \lfloor \frac{t}{2} \rfloor}{\frac{1}{12} t (t^2 - 1)} \\
&= \begin{cases} \frac{\frac{1}{8} t^2}{\frac{1}{12} (t)(t-1)(t+1)} & , \text{ when } t \text{ even} \\ \frac{\frac{1}{8} (t-1)(t+1)}{\frac{1}{12} (t)(t-1)(t+1)} & , \text{ when } t \text{ odd} \end{cases} \\
&= \begin{cases} \frac{3}{2} (\frac{t}{t^2-1}) & , \text{ when } t \text{ even} \\ \frac{3}{2} (\frac{1}{t}) & , \text{ when } t \text{ odd,} \end{cases}
\end{aligned}$$

which implies (66). □

Appendix F: Supplementary Tables and Figures

F.1. TLGRF vs Fixed Window Size Estimators

This subsection contains the additional RSME plot of TLGRF against fixed window size estimators mentioned in §5.1.

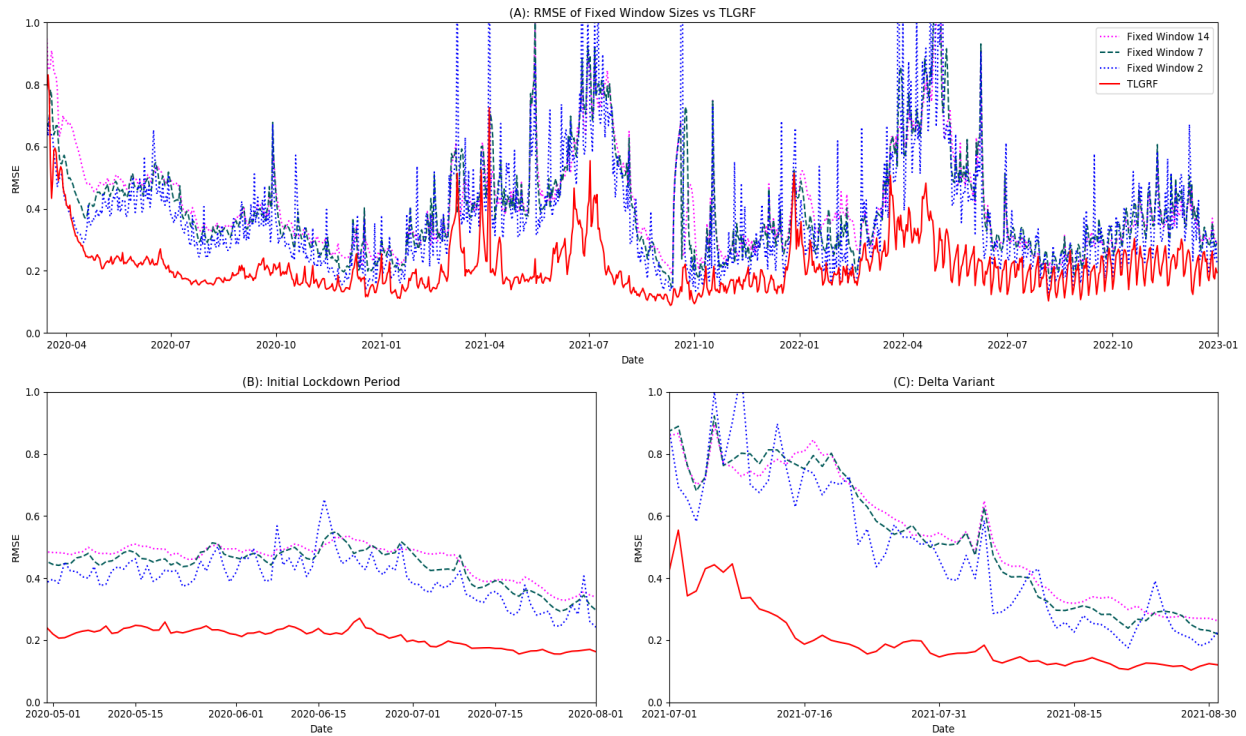


Figure 9 RMSE plot of prediction accuracy (TLGRF vs. Fixed 2-, 7-, and 14-Day Fitting Window): Plot A (Top) shows the RMSE comparison across the study period. Plot B (bottom left) zooms in on the initial lockdown period. Plot C (bottom right) zooms in on the period during the outbreak of the Delta variant.

F.2. TLGRF vs Dynamic Window Comparison

This subsection contains the additional RMSE plots of the Dynamic Window Size estimators in §5.2

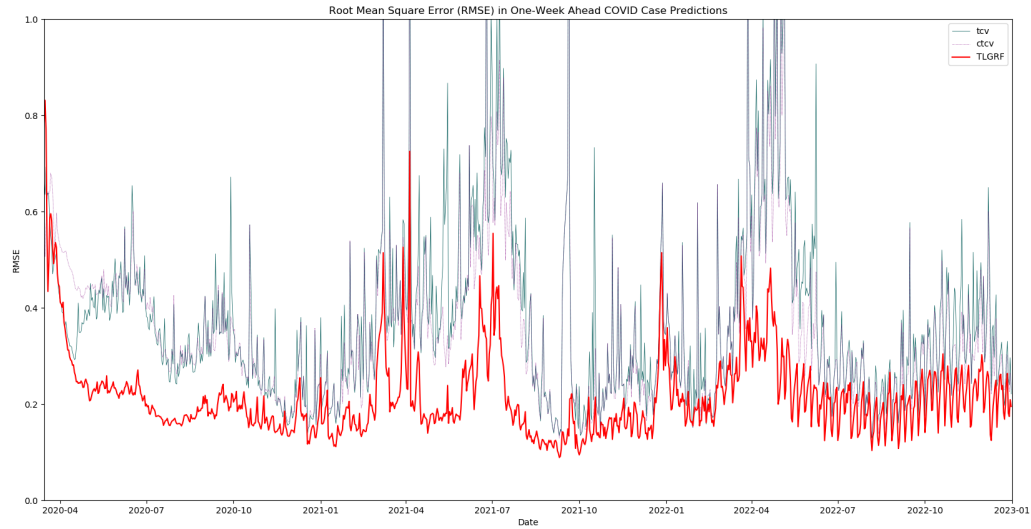


Figure 10 RMSE plot of prediction accuracy (TLGRF vs. Time-based Cross Validation (tcv) and County Time-based Cross Validation ($ctcv$))

F.3. TLGRF vs K-Means Dynamic Window Comparison

This subsection contains the RMSE plots of TLGRF vs. the K-Means Dynamic Window estimators with the lowest RMSE as mentioned in §5.3. This subsection also includes the plots of MAE and RMSE for different choices of K for the K-Means Dynamic Window estimators.

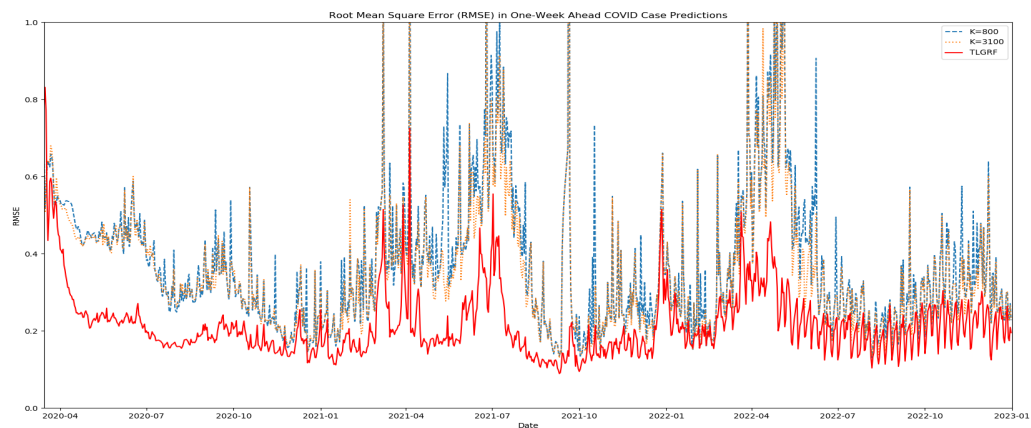


Figure 11 RMSE plot of prediction accuracy (TLGRF vs. K-Means Dynamic Window Estimators with choices $K = 800$ and $K = 3100$)

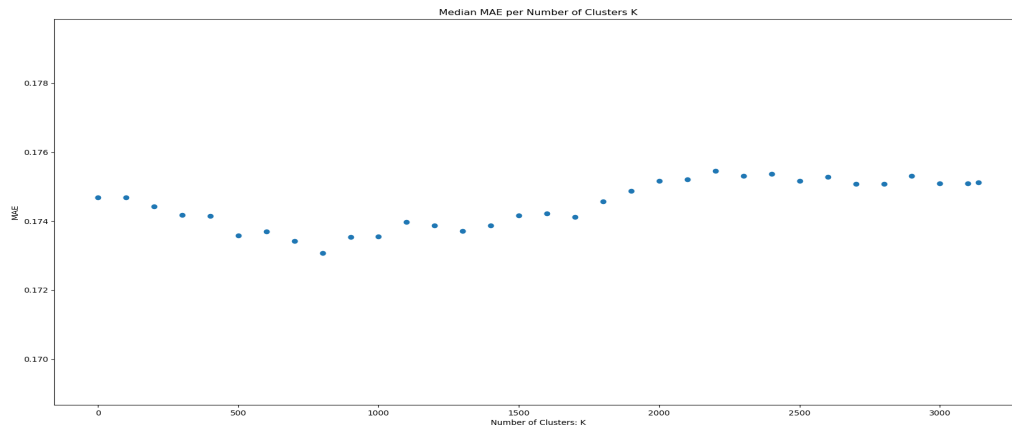


Figure 12 Median MAE by K for K-means Dynamic Window Estimator

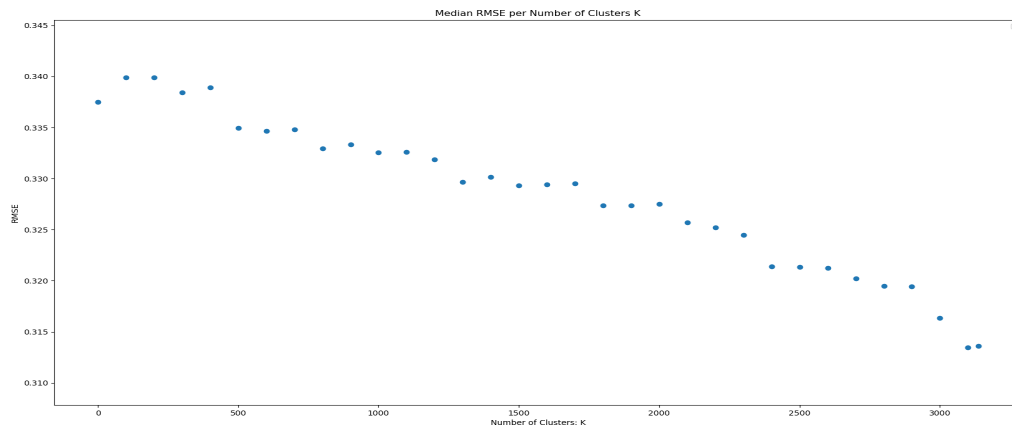


Figure 13 Median RMSE by K for K-means Dynamic Window Estimator

F.4. TLGRF vs Classical GRF Comparison

This subsection contains the additional RMSE plots of TLGRF against Classical GRF with and without time varying features mentioned in §6.1.

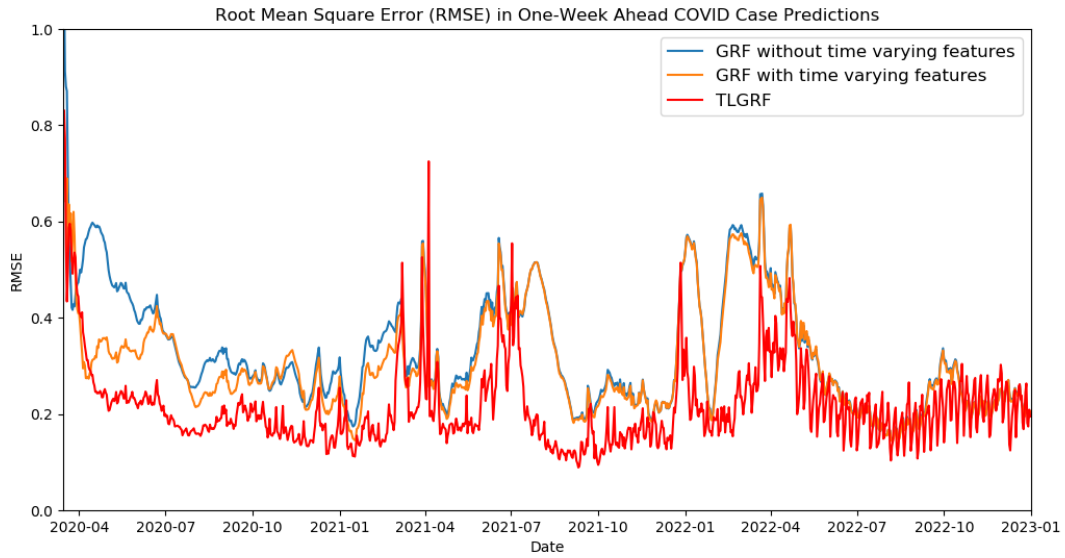


Figure 14 RMSE plot of prediction accuracy (TLGRF vs. Classical GRF with/without Time-varying Features)

F.5. TLGRF vs TLGRF Time Only Comparison

This subsection contains the median MAE and RMSE comparison of TLGRF vs TLGRF Time Only.

Method	MAE	RMSE
TLGRF Time Only	0.216	0.291
TLGRF	0.127	0.195

Table 16 Median MAE and RMSE of TLGRF vs. TLGRF Time Only

F.6. TLGRF vs TLGRF δ Comparison

This subsection contains the MAE and RMSE plots of TLGRF($\delta = 2$) vs. $\delta \in \{3, 4, 7, 14\}$ mentioned in §6.2

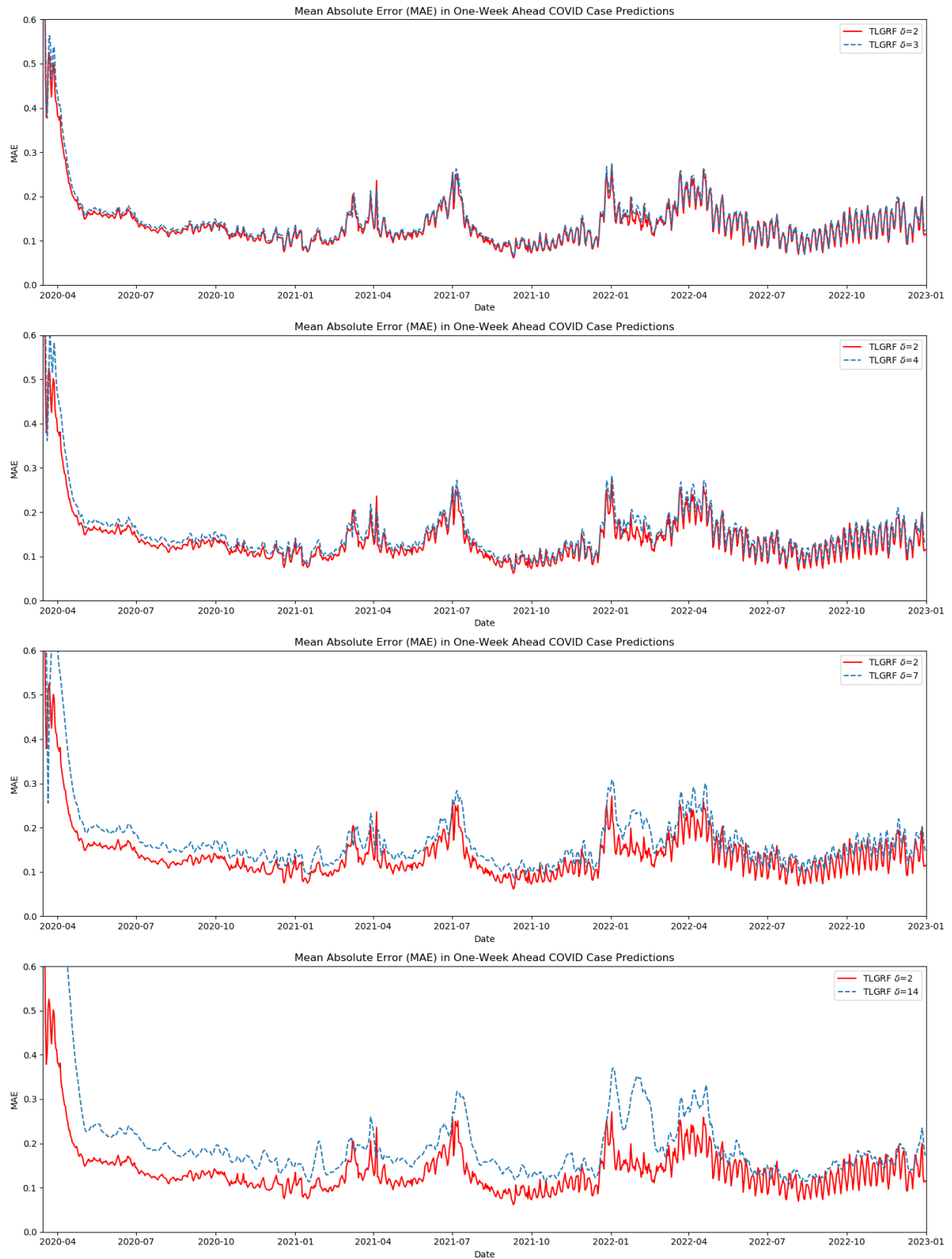


Figure 15 MAE plot of prediction accuracy (TLGRF with choices $\delta = 2$ vs $\delta = 3, 4, 7, 14$)

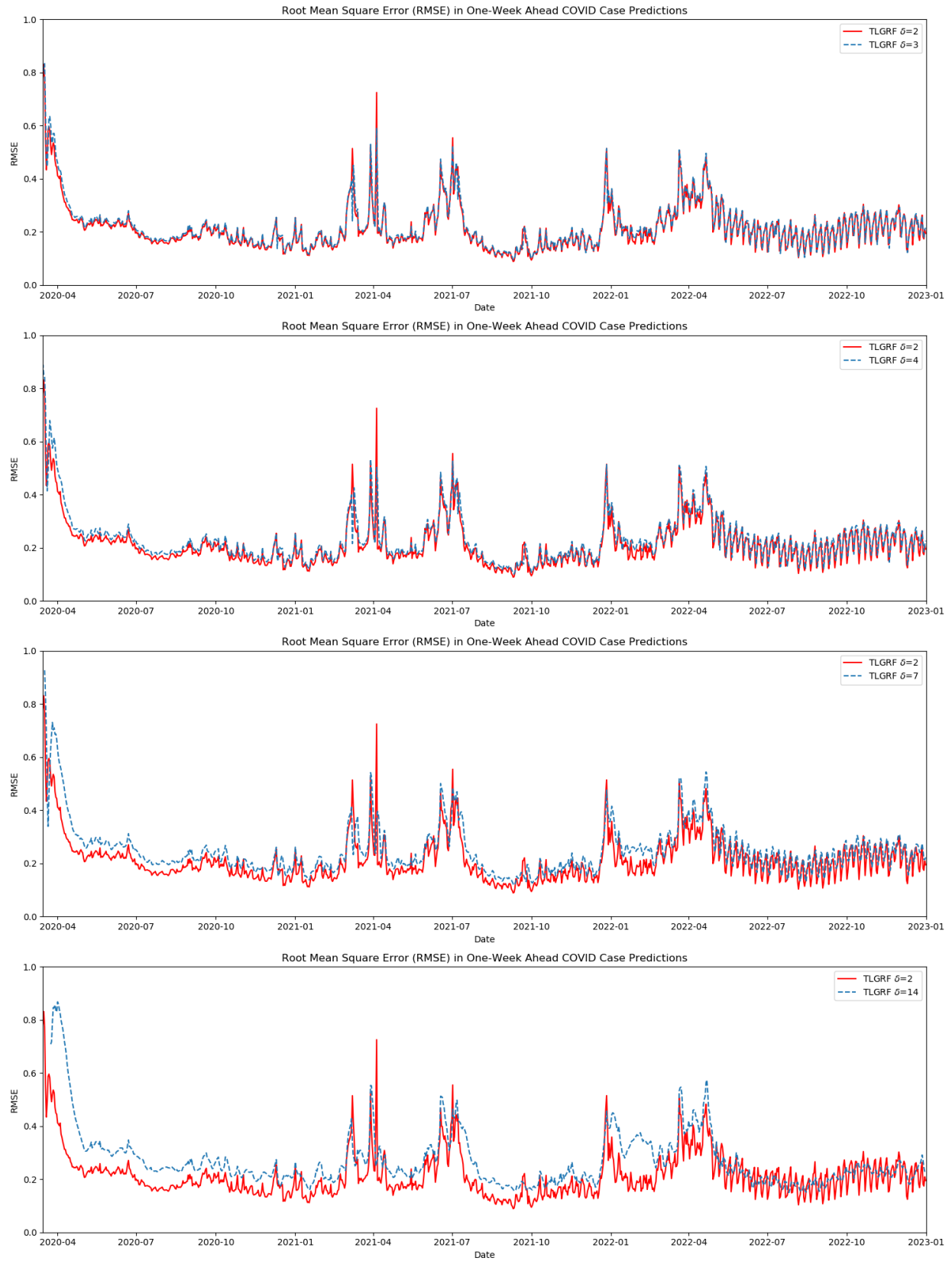


Figure 16 RMSE plot of prediction accuracy (TLGRF with $\delta = 2$ vs $\delta = 3, 4, 7, 14$)

Appendix G: Additional Analyses

This section provides additional details on the TLGRF tuning process and offers a more in-depth discussion of the Case Study.

G.1. Robustness and Stability of the TLGRF Algorithm

This section examines the robustness of the TLGRF regarding its key hyperparameters and performance indicators, i.e., fitting window size for the initial estimator, number of trees, leaf node sizes, and tree depth.

Fitting Window Size for the Initial Estimator (δ)

Results of extensive computational experiments on the impact of δ on TLGRF’s performance are presented and discussed in §6.2. These experiments reveal that the choice $\delta = 2$ achieves the best empirical performance.

Number of Trees

For the number of trees in TLGRF, we originally followed the default setting (i.e., `num.trees = 2000`) in the `grf` package (c.f. Athey et al. 2019). To seek more efficient implementations of TLGRF, we have conducted additional computational experiments and found that there was no substantial improvement in the algorithm’s empirical performance beyond 200 trees. Therefore, in the weekly update of our online decision support tool, we decided to keep the number of trees at 200 to alleviate the computational burden.

Leaf Node Sizes

Our TLGRF algorithm adopts the default leaf node size figuration (i.e., `min.node.size=5`) in the `grf` package (c.f. Athey et al. 2019). To investigate the potential impact of this hyperparameter on our algorithm’s behavior, we have conducted additional computational experiments in this revision. Specifically, we examine whether this minimum node size hyperparameter forces the split terminations in TLGRF. As illustrated in Figure 17, we have not found any evidence of this nature. Particularly, both the mean and median leaf node sizes observed in TLGRF significantly surpass the default minimum node size, which suggests that this hyperparameter does not affect the quality of TLGRF’s splits. Therefore, the performance of TLGRF is not affected by the default setting of minimum node size.

Tree Depth

Sufficient tree depth within the TLGRF algorithm is important to effectively identify meaningful subpopulations for splitting. However, excessively deep trees may risk overfitting to specific subpopulations. This section focuses on the evolution of trees in TLGRF with increasing training data volume and assesses whether an adequate tree depth is achieved by this algorithm. Figure 18 portrays a progression in tree depth of TLGRF, initially averaging at a depth of 11 and eventually stabilizing around a depth of 33 as the dataset expanded. Additionally, Figure 17 reveals a consistency in both mean and median leaf node sizes of TLGRF throughout our study period. Observations from Figures 17 and 18 highlight that the splitting behavior of TLGRF remains consistent even with increasing data fed into the algorithm. Such evidence supports the notion that TLGRF has achieved an adequate tree depth, allowing it to accurately classify large volumes of data.

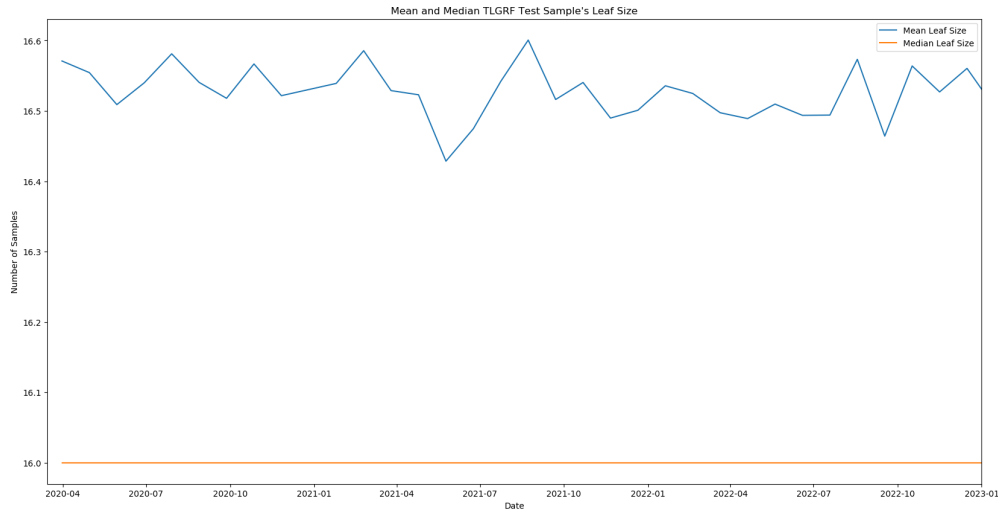


Figure 17 Mean and Median Leaf Sizes of TLGRF

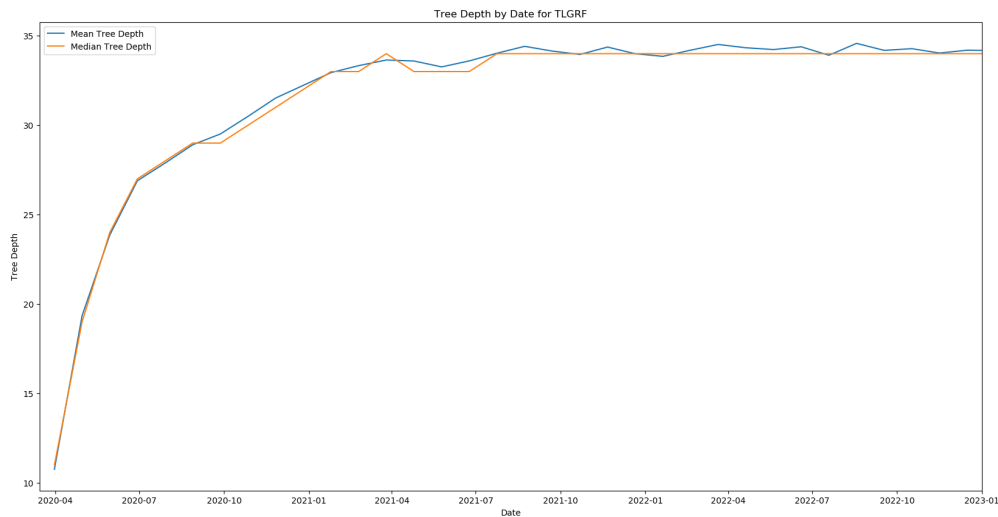


Figure 18 Mean and Median Tree Depth of TLGRF

G.2. TLGRF Time Only Characteristics

To investigate TGLRF *Time Only*'s decrease in performance with respect to TLGRF, we decided to inspect the mean and median depths of each tree in both TLGRF and TLGRF *Time Only*.

As seen in Figure 19, TLGRF *Time Only*'s trees are considerably more shallow than that of TLGRF's, where the latter's depths are typically 10 times that of the former. It is clear that the historical data of one county, which is what TLGRF *Time Only* has access to, contains significantly less information than that of the entire country, which is utilized by TLGRF. This comparison shows that the lack of access to spatial information hinder TLGRF *Time Only*'s ability to properly conduct transfer learning, resulting in decreased performance.

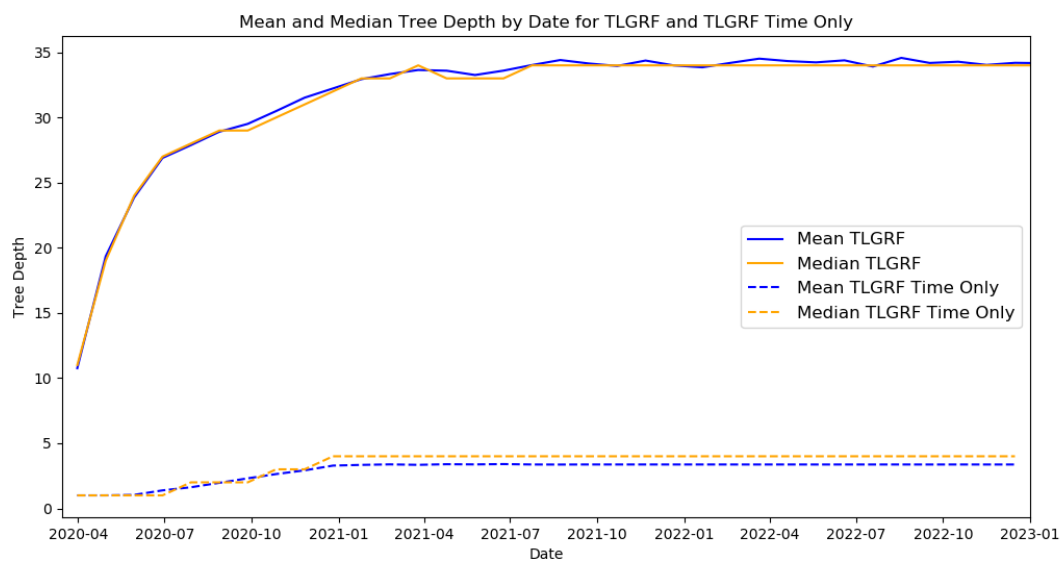


Figure 19 Mean and median tree depth by date (TLGRF vs. TLGRF Time Only)

G.3. Additional Analyses for the CDPHE Case Study

In this appendix subsection, we present additional information complementing our case study in §8. First, in §G.3.1, we provide further details regarding the number of decision points and the counties investigated. Following that, in §G.3.2, we conduct a more in-depth analysis comparing the performance of TLGRF and CDPHE. Last, in G.3.3, we consider an alternative use case of TLGRF.

G.3.1. Decision Points and Outbreak Investigations

Our study period, which spans 2020-03-17 to 2022-12-31, has a total of 159 decision points (DPs) and 182 investigated counties. A plot of how many investigations were made at each date is given below in Figure 20 and in Table 17.

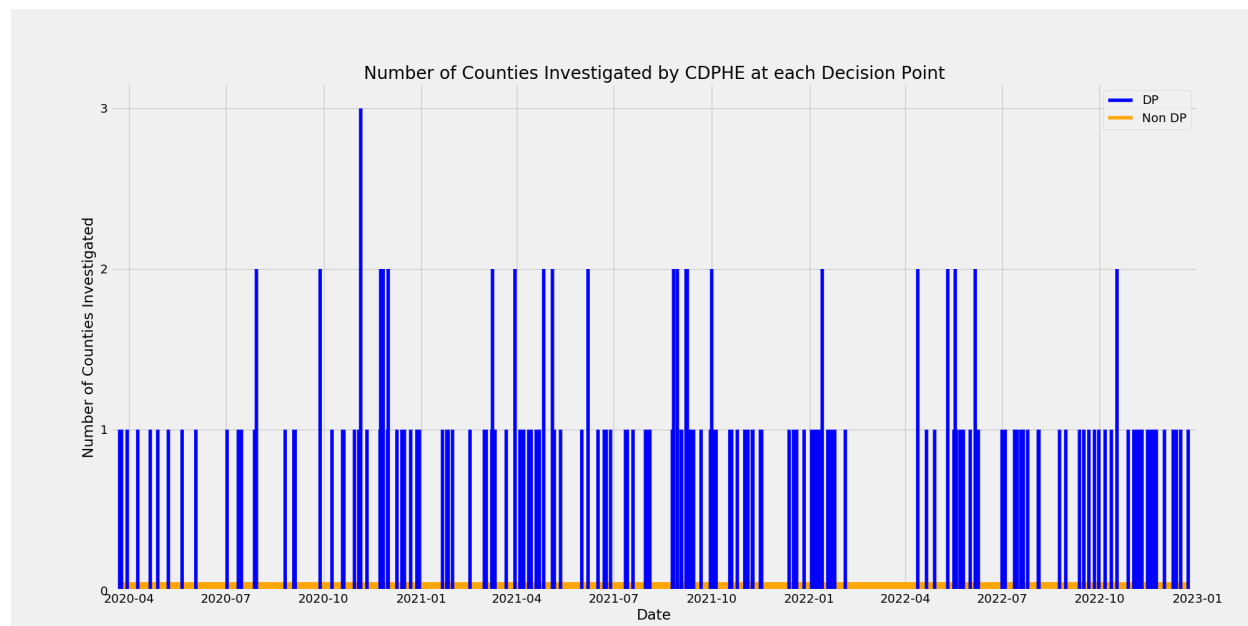


Figure 20 Daily Number of New Investigations Initiated by CDPHE

	# of Days	Daily # of New Investigations
Non-decision points	861	0
	137	1
Decision points	21	2
	1	3

Table 17 Distribution of Daily Number of New Investigations Initiated by CDPHE

G.3.2. TLGRF vs. CDPHE Further Analyses

We further examine if there are systematic differences in counties chosen for investigations by CDPHE and TLGRF. We also investigate what types of counties are most frequently misclassified by the CDPHE and TLGRF, respectively.

First, we compare CDPHE to TLGRF's performance in the more populous counties in Table 18. We observe that both the CDPHE and TLGRF exhibit higher PPV and F1 Scores in this analysis when we focus on the more populous subset of counties in Colorado. However, TLGRF still consistently outperforms CDPHE across all subsets and metrics. We provide an intuitive explanation behind this. As we explained §8, the TLGRF decision criterion is implicitly weighted by the population of counties as it prioritizes counties with high current reported incident case numbers. Therefore the TLGRF algorithm is inherently capturing CDPHE's investigation prioritization of outbreaks in more populous counties, but in a more targeted manner.

Most Populous Counties	CDPHE		TLGRF	
	PPV	F1	PPV	F1
Top 10%	0.3333	0.3636	1.0000	1.0000
Top 20%	0.3571	0.2020	0.6974	0.7211
Top 50%	0.2185	0.2023	0.6268	0.6357
All	0.1813	0.1813	0.5879	0.5879

Table 18 Positive Predictive Value (PPV) and F1 Score of CDPHE and TLGRF on the more populous counties of Colorado

Finally, Tables 19 and 20 present the summary statistics of counties most frequently misclassified by CDPHE and TLGRF, respectively. Notably, our investigation reveals significant overlap in the commonly misclassified counties by CDPHE and TLGRF. Specifically, the most frequently misclassified counties, on average, exhibit a lower total population size and other notable census statistics (e.g., individuals facing poverty, unemployment, or disabilities) in comparison to the state average. These findings suggest that CDPHE and TLGRF share similar empirical patterns in terms of their investigation priorities.

Counties of:	Statistics	Total Population	Poverty	Unemployed	Age > 65	Age < 17	Disabled	Uninsured
CDPHE Incorrect	Mean	35495.4	3572.0	839.3	5491.2	7386.2	3635.9	3265.0
	Median	18325.0	2084.0	531.0	3459.0	3381.0	2332.0	1864.0
CDPHE Correct	Mean	69929.6	8138.9	1602.4	9320.1	14571.1	7039.1	7057.1
	Median	27754.0	3296.0	736.0	5076.0	5845.0	2990.0	2414.5
All Colorado	Mean	43319.7	4568.9	1037.7	6468.0	9004.7	4379.4	4226.2
	Median	25162.0	3075.0	589.0	3689.0	5514.0	2939.0	2395.0

Table 19 Comparison of Mean and Median statistics of the Top 10 most frequently misclassified and correctly classified Colorado counties by CDPHE

G.3.3. An Alternative Use Case of TLGRF

This section delves into an alternative use case of TLGRF, building on the use case discussed in §8. Specifically, TLGRF can be utilized to configure an absolute threshold policy. That is, instead of choosing a relative threshold as in §8, we can select a fixed threshold. This absolute threshold policy would then recommend investigating all counties that have caseload increases beyond this threshold projected by TLGRF. In other words, the less stringent or lower this predetermined threshold is, the more counties would be investigated under this policy. To quantify the number of investigations recommended by absolute threshold policies, we have experimented with different thresholds and plotted two of them in Figure 21.

Counties of:	Statistics	Total Population	Poverty	Unemployed	Age > 65	Age < 17	Disabled	Uninsured
TLGRF Incorrect	Mean	25699.0	2447.4	601.3	4073.5	5181.0	2570.6	2606.6
	Median	17909.0	1890.0	500.0	3253.0	2954.0	2332.0	1762.0
TLGRF Correct	Mean	58924.5	6003.8	1338.8	8490.7	11784.9	5618.5	5637.7
	Median	55101.0	4609.0	1250.0	8634.0	10565.0	4854.0	4993.0
All Colorado	Mean	43319.7	4568.9	1037.7	6468.0	9004.7	4379.4	4226.2
	Median	25162.0	3075.0	589.0	3689.0	5514.0	2939.0	2395.0

Table 20 Comparison of Mean and Median statistics of the Top 10 most frequently misclassified and correctly classified Colorado counties by TLGRF

We now discuss the practical implications of implementing policies based on absolute thresholds. As shown in Figure 21, it is difficult to integrate CDPHE's investigation resource constraint into absolute threshold-based policies. On one hand, when a lower threshold is chosen (e.g., Threshold=10), this policy would recommend a large daily investigation number that exceeds the capacity constraint of CDPHE. On the other hand, when a higher threshold is chosen (e.g., Threshold=30), this policy would recommend too few investigations on some days when investigation resources are available. In general, it can be challenging for an absolute threshold policy to match the investigation frequency of CDPHE. Therefore, recommendations made by an absolute threshold policy may not always be feasible for CDPHE.

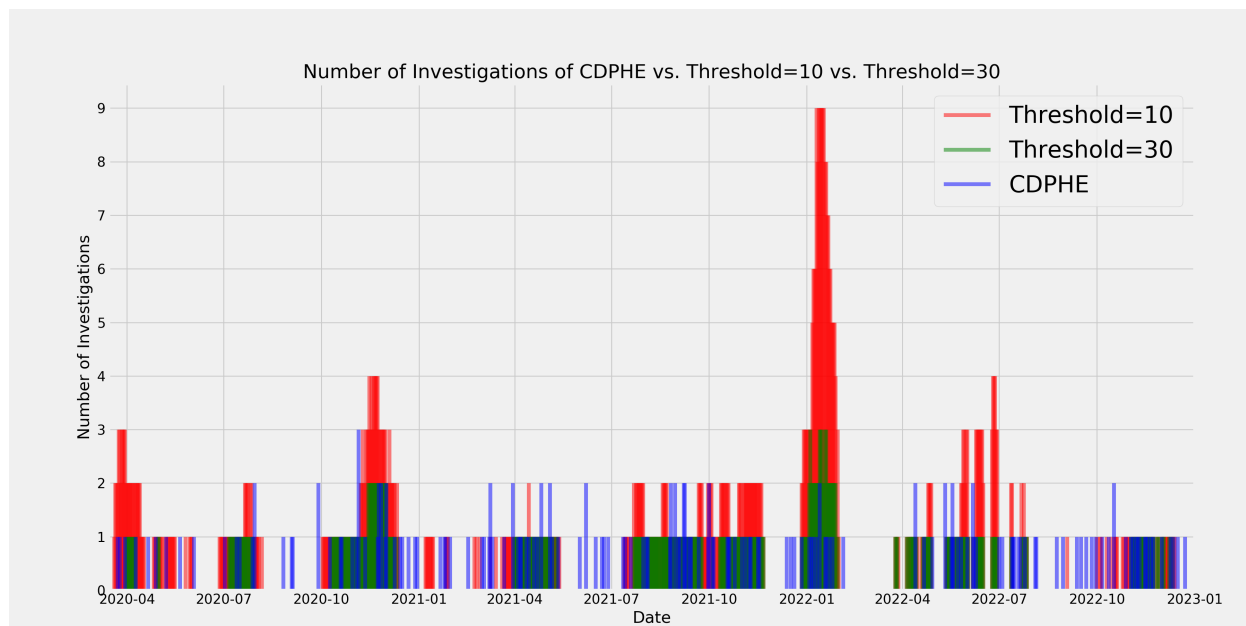


Figure 21 Daily Number of New Investigations Initiated by CDPHE
vs.
Daily Number of New Investigations Recommended by the Absolute Threshold Policy with Threshold=10 and Threshold=30

Appendix H: COVID-19 Outbreak Detection Tool: Additional Details

The outbreak detection tool reports county-level doubling times on a weekly basis throughout the course of the pandemic. Doubling time, defined as $\frac{\ln(2)}{r_{t,c}}$, converts the instantaneous county-level growth rate $r_{t,c}$ estimated from TLGRF to an intuitive metric that is easier to explain to the general public. Specifically, doubling time captures the rate of spread of COVID-19 in each county: a longer doubling time means that COVID-19 is spreading slower, and vice versa. For example, Figure 22 shows the COVID-19 doubling times of each county in the U.S. during the Omicron wave in December 2021 to January 2022. Just before the spread of Omicron variant in early-December 2021, COVID-19 cases were declining, which is evident from the increase in the doubling time from December 05, 2021, to December 26, 2021. However, the Omicron variant started emerging in December end. By early January, the doubling time in most counties was less than 2 weeks. The latest COVID-19 doubling time in each county can be seen at www.covid19sim.org.

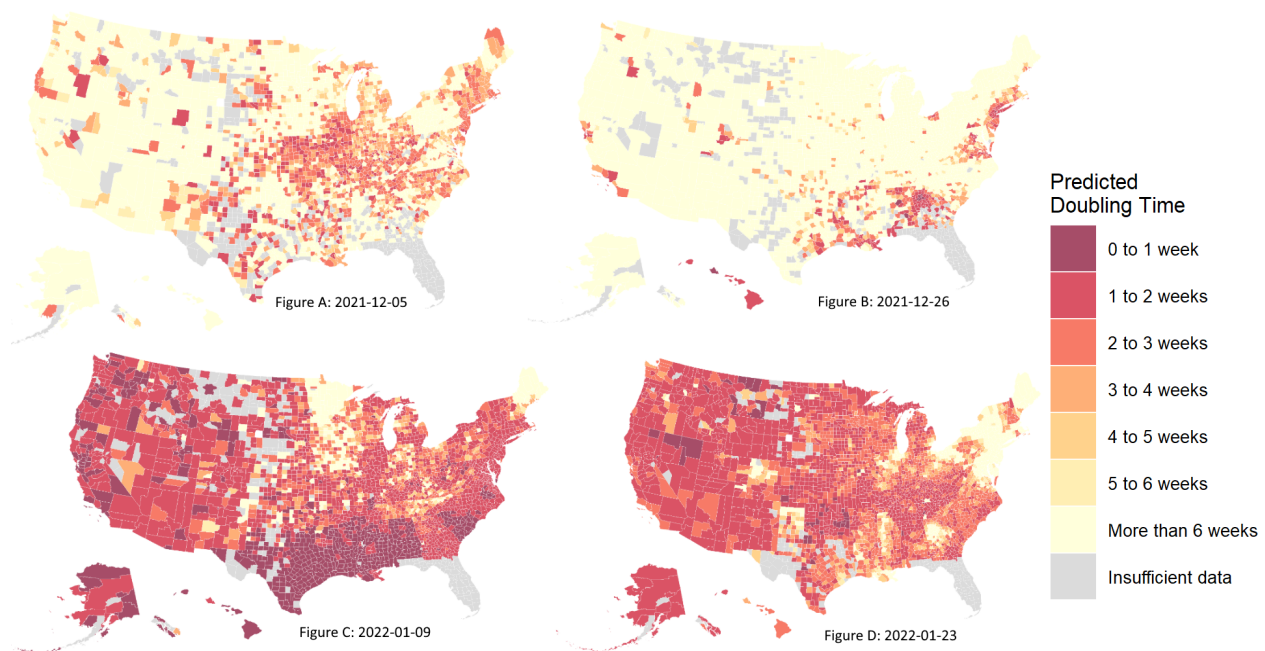


Figure 22 Snapshots of the chloroplast of county-level doubling days on our website at various points in time from 2021-12-05 to 2022-01-23. The doubling day of incident COVID-19 case number at county c on day t is derived from the instantaneous county-level growth rate $r_{t,c}$ as $\frac{\ln(2)}{r_{t,c}}$.

Furthermore, we feature a data explorer (see Figure 23): an interactive spreadsheet of doubling days, recorded cases and deaths, vaccination adoption etc. for the more inquisitive members of the public, where they can filter, sort, and search through the data as desired and download it as a csv file. Detailed documentation is publicly accessible on www.covid19sim.org and all code and data are open source.

The web platform of this decision support tool, “COVID-19 Outbreak Detection Tool”, was released on the 15th of September 2020.

Our outbreak detection tool has been well received since its launch. The website had around 105 daily visitors during the 2020 winter COVID-19 wave, where web traffic peaked at around 2000 visitors a day, and has an accumulated total of 20,000 authentic users from all 50 states. We have also been consulted by public health officials from the states of Maryland, Michigan, and Massachusetts, and helped them use this outbreak detection tool to guide their decision-making during the pandemic. Finally, our outbreak detection tool has also attracted significant public attention and was featured in leading media outlets, including The Voice of America and National Public Radio.

Data Explorer

Show entries Search:

County	State	Population	Fully vaccinated population	Average daily cases in the past week	Average daily cases in the past week (per 100K)	14-day incident case trend	COVID-19 Doubling Weeks
Ziebach	South Dakota	2756	32%	20	741		1 to 2 weeks
Dewey	South Dakota	5892	72%	99	1673		1 to 2 weeks
Prince George's	Maryland	909327	72%	695	76		2 to 3 weeks
Baltimore	Maryland	593490	63%	522	88		2 to 3 weeks
Rio Blanco	Colorado	6324	38%	16	248		3 to 4 weeks
Lee	Kentucky	7403	49%	40	536		3 to 4 weeks
Baltimore	Maryland	827370	70%	516	62		3 to 4 weeks
Elliott	Kentucky	7517	35%	34	449		4 to 5 weeks
Gooding	Idaho	15179	43%	18	118		4 to 5 weeks
Marengo	Alabama	18863	54%	63	332		4 to 5 weeks

Showing 1 to 10 of 3139 entries Previous 2 3 4 5 - 314 Next

Figure 23 Snapshot of the data explorer on our website, where the user can interactively filter, sort, and search through the relevant county level data and download it as a csv file if desired